

AIX-MARSEILLE UNIVERSITÉ

ÉCOLE DOCTORALE SCIENCES POUR L'INGÉNIEUR:
MÉCANIQUE, PHYSIQUE, MICRO ET NANOÉLECTRONIQUE

INSTITUT DE RECHERCHE SUR LES PHÉNOMÈNES HORS
ÉQUILIBRE

THÈSE

présentée pour obtenir le grade de
DOCTEUR D'AIX-MARSEILLE UNIVERSITÉ
SPÉCIALITÉ: MÉCANIQUE ET PHYSIQUE DES FLUIDES

par

Eduardo DURÁN VENEGAS

Modélisation et optimisation d'un rotor à pales flexibles

Soutenue le 05/06/2019 devant le jury composé de

| | | |
|---------------------|--|-----------------------|
| Stéphane Le Dizès | Directeur de recherche, CNRS, IRPHE | Directeur de thèse |
| Christophe Eloy | Professeur, ECM, IRPHE | Co-Directeur de thèse |
| François Gallaire | Professeur associé, EPFL, Suisse | Rapporteur |
| Philippe Chatelain | Professeur, UCL, Belgique | Rapporteur |
| Sabine Ortiz-Clerc | Professeure, ENSTA ParisTech | Examinatrice |
| Ivan Delbende | Maître de Conférences, Sorbonne Université, LIMSI | Examineur |
| Luis Parras Anguita | Professeur assistant, Universidad de Málaga, Espagne | Examineur |

Contents

| | | |
|----------|---|-----------|
| 1 | Introduction | 5 |
| 1.1 | Context | 6 |
| 1.2 | Description of the wake of a rotor | 8 |
| 1.2.1 | Rotor regimes | 8 |
| 1.2.2 | Momentum theory | 11 |
| 1.2.3 | Vortex methods | 13 |
| 1.3 | Aerodynamic loads | 16 |
| 1.3.1 | An introduction to airfoil aerodynamics | 16 |
| 1.3.2 | Blade element theory | 18 |
| 1.4 | Blade deformation | 20 |
| 1.4.1 | Mechanical properties of deformable materials | 20 |
| 1.4.2 | Beam model | 21 |
| 1.5 | A note on fluid-structure interactions | 23 |
| 1.6 | Helical vortices in a rotor wake | 23 |
| 1.7 | Stability of wake solutions | 24 |
| 1.8 | General overview | 27 |
| 2 | Wake model | 29 |
| 2.1 | Chapter overview | 30 |
| 2.2 | Generalized Joukowski model | 30 |
| 2.3 | Far-wake solutions | 31 |
| 2.3.1 | Vortex filament framework | 31 |
| 2.3.2 | Deformed helical vortex pairs | 39 |
| 2.3.3 | Analysis of the effect of a varying core size | 50 |
| 2.3.4 | Discussion in the context of rotors | 50 |
| 2.4 | Near-wake solutions | 53 |
| 2.4.1 | Framework | 53 |
| 2.5 | $R_b^* = 0$ case (Standard Joukowski model) | 55 |
| 2.5.1 | Framework | 55 |
| 2.5.2 | Wake solutions | 56 |
| 2.5.3 | Induced velocities | 60 |
| 2.5.4 | Energy extracted by a wind turbine | 65 |
| 2.6 | $R_b^* \neq 0$ case (Generalized Joukowski model) | 67 |
| 2.6.1 | Topology of the solutions | 67 |
| 2.6.2 | Parametrical analysis | 68 |
| 2.6.3 | Comparison with the standard model | 74 |

| | | |
|----------|--|------------|
| 2.7 | Chapter conclusion | 76 |
| 3 | Stability of the wake | 77 |
| 3.1 | Chapter overview | 78 |
| 3.2 | Perturbation model | 79 |
| 3.3 | Modal decomposition | 81 |
| 3.4 | Spatio-temporal evolution | 84 |
| 3.5 | Chapter conclusion | 86 |
| 4 | Rigid blade | 87 |
| 4.1 | Chapter overview | 88 |
| 4.2 | Rigid blade framework | 88 |
| 4.2.1 | Induced velocity on the rotor | 88 |
| 4.2.2 | Circulation law and equivalent Joukowski profile | 89 |
| 4.2.3 | Aerodynamic loads | 91 |
| 4.2.4 | Tip effect correction | 91 |
| 4.2.5 | Model parameters | 92 |
| 4.3 | Comparison with numerical and experimental results | 92 |
| 4.3.1 | MEXICO rotor project | 92 |
| 4.3.2 | The Unsteady Aerodynamic Experiment (UAE) | 96 |
| 4.3.3 | A hovering case: NASA Technical report TM81232 | 98 |
| 4.4 | Chapter conclusion | 100 |
| 5 | Flexible blade | 101 |
| 5.1 | Chapter overview | 102 |
| 5.2 | Deformation model | 102 |
| 5.3 | Fluid-structure interaction | 105 |
| 5.4 | Applications | 105 |
| 5.4.1 | Description of the rotors | 105 |
| 5.4.2 | Results | 106 |
| 5.5 | Chapter conclusion | 109 |
| 6 | Conclusions | 113 |
| 6.1 | Achievements | 113 |
| 6.2 | Future work | 114 |
| | Appendices | 117 |
| A | Numerical methodology | 119 |

Chapter 1

Introduction

Contents

| | | |
|------------|---|-----------|
| 1.1 | Context | 6 |
| 1.2 | Description of the wake of a rotor | 8 |
| 1.2.1 | Rotor regimes | 8 |
| 1.2.2 | Momentum theory | 11 |
| 1.2.3 | Vortex methods | 13 |
| 1.3 | Aerodynamic loads | 16 |
| 1.3.1 | An introduction to airfoil aerodynamics | 16 |
| 1.3.2 | Blade element theory | 18 |
| 1.4 | Blade deformation | 20 |
| 1.4.1 | Mechanical properties of deformable materials | 20 |
| 1.4.2 | Beam model | 21 |
| 1.5 | A note on fluid-structure interactions | 23 |
| 1.6 | Helical vortices in a rotor wake | 23 |
| 1.7 | Stability of wake solutions | 24 |
| 1.8 | General overview | 27 |

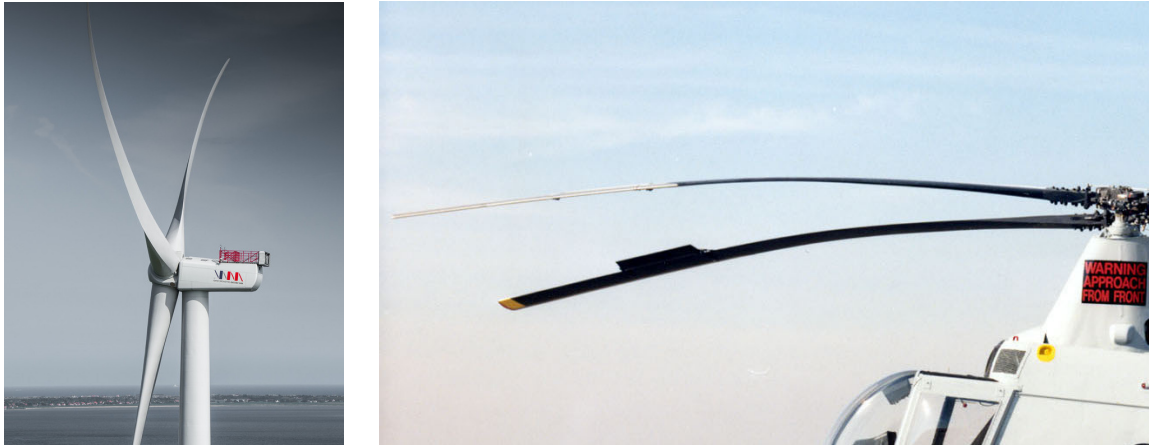


Figure 1.1: Left: *V164* offshore wind turbine model from MHI Vestas Offshore Wind, with a diameter of 164m and a total power of 9.5MW (source: www.mhivestasoffshore.com). Right: Detail of the blades of a Kaman HH-43B Huskie helicopter (source: www.nationalmuseum.af.mil)

1.1 Context

The term *rotor* is used in many technical domains, from mechanical to electrical engineering, to define rotating parts of a machine or a mechanical assembly. In this thesis, we are interested in rotors as defined in aeronautics: a system of rotating airfoils. This kind of rotor can transform the movement of a fluid into mechanical rotation or vice-versa. It has been used for centuries and they are very common in many daily applications. In particular, we are interested in two of its main uses: harvesting and propulsion.

Harvesting devices are probably the most ancient rotor applications. The principle is to transform the kinetic energy of a flow into a mechanical or electrical energy through the rotation of the system. The use of watermills and windmills to obtain useful mechanical energy has been documented for more than a thousand years. Nowadays, one of the main rotor applications in harvesting is wind turbine. The total installed power in wind farms grows every year, introducing more and bigger devices that generate new technical challenges. In the last years, the tendency has been to design more powerful devices by increasing the diameter of the rotor (Figure 1.1a shows a turbine *Vesta V164*, with 164m of diameter), however the great increase in the length of the blades introduces important effects on their deformation that can affect the performance of the rotor. Furthermore, the construction of populated wind farms presents some technical problems caused by the interaction between devices. The wake generated behind a rotor can interfere in the following row, altering the incoming flow and reducing the efficiency of the turbines. Having a good comprehension of the dynamic mechanisms of the wake or blade deformation is fundamental to give a solution to these problems.

Propulsion devices follow a principle inverse to that of wind turbines: a rotation is forced mechanically in order to generate a motion of the fluid and induce a thrust force perpendicular to the rotor disc. This kind of rotors can be found in boat propellers or helicopters. The main difficulty in the analysis and design of helicopter rotors lies in



Figure 1.2: Rotor with very flexible blades. Left: at rest; right: rotating. From Sicard (2014).

the many different flow configurations they can adopt, depending on the external wind conditions and if the vehicle is ascending, descending or in horizontal flight. In this sense, several sorts of transitions and instabilities can occur on the wake while helicopter is operating. These instabilities may lead to dangerous flight situations, as the so called Vortex Ring State, where a vortex ring system is generated around the rotor, producing a problematic loss of lift. Again, understanding the behaviour of the wake is fundamental to prevent this kind of issues. The effect of deformation of the blades is also very important in helicopters because of the slenderness of the blades and the great aerodynamic forces exerted on them. In figure 1.1b, a helicopter Kaman HH-43B is shown at rest where the deformation of the blades can be perfectly noticed.

Another particular case of propulsion rotors is found in drones, whose use in society has grown noticeably in the last decade. These devices are quite recent and have not involved as much research as helicopters. Frequently, their rotors are designed as copies of aircraft propellers at a smaller scale, however, drones have particular characteristics that should be taken into account:

- For different reasons, as reducing manufacturing cost, blades are often made of plastic. The use of polymeric materials for the design of the blades further increases the importance of the deformation in the study of their performance. In figure 1.2 is displayed a case of a very flexible drone rotor, where the blades are extremely deformed at rest and get straight under the effect of the centrifugal forces when rotating.
- Contrary to helicopter rotors, pitch cannot be controlled in drones. This implies a simpler construction, however, blades have to be designed to be capable to operate in different flight conditions even without pitch control.
- It is very common in drones to set up multiple rotors. In that case, displacement of the drone is controlled by varying the rotational speed, and so the thrust, of the different rotors. Typical configurations, where rotors are placed in vertical-axis position, permit a slow horizontal displacement of the device. For faster displacements, new innovative configurations are proposed, as convertible drones, where rotor axis



Figure 1.3: NASA GL-10 convertible drone. Source: *www.nasa.gov*

inclination can be modified from vertical to horizontal position (figure 1.3). For this kind of drone, rotors have to be specifically designed to operate in these two different configurations, consequently, a good comprehension of blades deformation or rotors wakes interaction is required.

In conclusion, in spite of their long history, rotors are a constantly developing technology. Understanding the dynamic of the wake, its interaction with the rotor and the mechanisms of deformation of the blades is important to address new challenges in rotors design. Understanding the coupling mechanisms between the flow and the flexibility of the rotor would be very useful from the point of view of optimization. Introducing the elasticity of the blades on rotor design could help, for example, to improve the performance of drones or enlarge the operational range of wind turbines. Having a precise description of the wake may also help to predict the transition to dangerous helicopter flight regimes or avoid interference between turbines in wind farms. However, these problems are very complex and heavy from the point of view of computation. The fluid-structure interaction problem resulting from the effect of the flow on the blade deformation and vice-versa becomes very heavy to compute using Direct Numerical Simulation methods. This complexity makes impossible any optimization procedure or any extensive parametric analysis with current computation means. In this work, different simplifications are proposed at every level to reduce the complexity and computational cost of the problem resolution, resulting in a light model with low computation times allowing to address optimization analysis. This model would provide a versatile tool to address new challenges in rotor design.

1.2 Description of the wake of a rotor

1.2.1 Rotor regimes

Rotor operating conditions are quite different in wind turbines, helicopters or drones. Each kind of device have its particularities and mechanical restrictions that affect the orientation and interaction with the external flow. In wind turbines, the external flow passes through the rotor disc and aerodynamic forces generate the rotation. To control the operating regime, they can change the pitch of the blades or the rotor orientation with external wind. Having the rotor in good configuration with respect to the external flow is crucial for the efficiency of the turbine. In helicopters, we do not have that strong

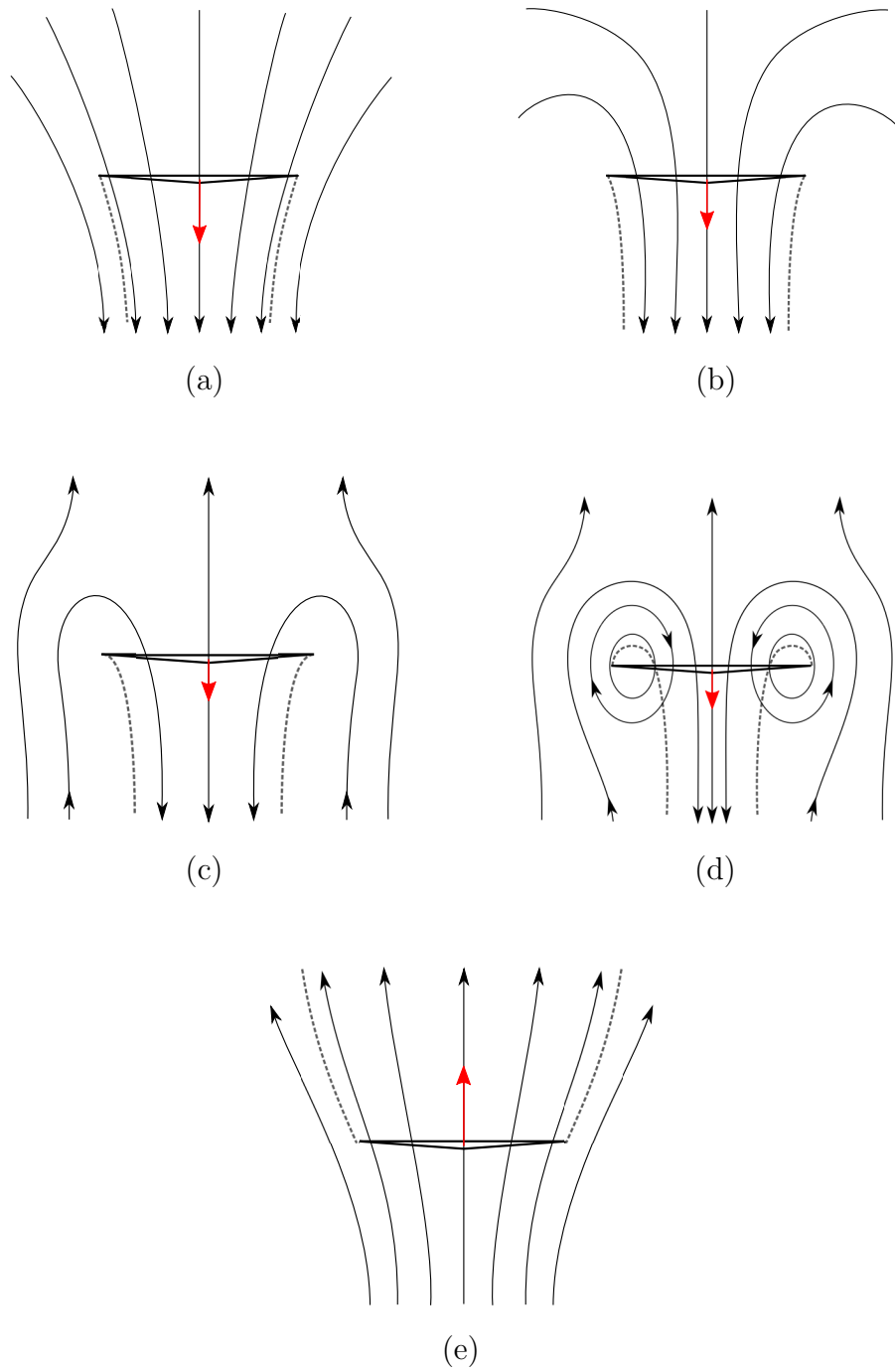


Figure 1.4: Scheme of the flow crossing the rotor plane for different regimes under an external axial flow. The black arrows represent the streamlines of the flow, while the dashed line represent the projection of the curve enveloping the wake. The red arrow shows the direction and the relative magnitude of the total velocity crossing the rotor plane. (a) Climbing flight. (b) Hover. (c) Slow descent. (d) Vortex-Ring State. (e) Windmill-brake / Wind turbine.

dependency with the external wind. In this case, rotation of the blades is imposed, generating a lift force that balance the weight of the aircraft. There are three main ways to control the flight: collective pitch, cyclic pitch and anti-torque. The collective pitch changes the angle of attack of all the blades at the same time, modifying the lift and allowing a vertical climbing or descending. The cyclic pitch implies a local variation of the angle of attack, causing an horizontal displacement of the helicopter. The anti-torque is a system to avoid uncontrolled rotation of the cabin produced by the torque of the rotor. Several solutions exist to compensate the torque, the most common is with a small tail rotor. The regulation of this system, over- or under-compensating the torque, introduces a controlled rotation on the cabin. In drones, as it was explained in the previous section, size restriction makes it impossible to include complex pitch control systems. Flight control is made by modifying the speed of the different rotors. In conclusion, many different flow regimes can be reached depending on the operational conditions of the device.

In this work, we will focus on uniform axial flow regimes, that is, when the external flow is homogeneous and aligned with the rotor axis. This corresponds to the normal operational conditions of wind turbines and vertical flight regimes of helicopters and drones. In particular, the non-homogeneous character of the wind owing to the presence of the ground is not taken into account for the wind turbines. For helicopters, the forward flight regimes are not considered in the present work. The external flow is always assumed to be perpendicular to the rotor plane. Under this hypothesis, the analysis of different operating states can be reduced to a few rotor regimes (figure 1.4). The rotation of the blades induces a flow perpendicular to the rotor plane. This induced flow can have the same direction as the external flow or be opposed to it. Depending on the regime, a rotor can accelerate or decelerate the external flow. Figure 1.4 shows a sketch of the mean flow (azimuthally averaged) streamlines crossing the rotor plane for the different rotor regimes. The streamlines are the family of curves that are parallel to the flow direction, so they never cross each others. In a three-dimensional flow, an ensemble of streamlines that form a closed surface is called streamtube. In figure 1.4, as axisymmetric flow is assumed, streamlines also correspond to streamtubes of circular cross section.

In the case of helicopters or drones in ascending flight (figure 1.4a) the external flow and the induced flow have the same direction, so the flow is accelerated. In the case of hovering flight (figure 1.4b), there is no external flow, so all the displacement of the fluid is generated by the rotor. The most interesting cases is probably when the external and the induced flows are in opposite directions; in that situation, different regimes can appear.

The simplest regime to analyze is probably associated with wind turbines or windmill brake descending helicopter (figure 1.4e), where the external flow is strong and the total flow has always the same direction across the whole rotor plane. However, there are regimes associated with helicopters in descending flight where the induced flow is strong compared to the external flow and the total flow changes its direction across the rotor plane. In soft descending flight regime (figure 1.4c), the flow crossing the rotor plane goes upwards out of the rotor disc and downwards inside of it. If the descending speed is increased, the Vortex Ring State regime (figure 1.4d) can be reached, where the flow direction changes inside the rotor disc, generating lift problems with serious consequences to the security of the helicopter.

To study the flow generated by the rotor in these different axial regimes, various

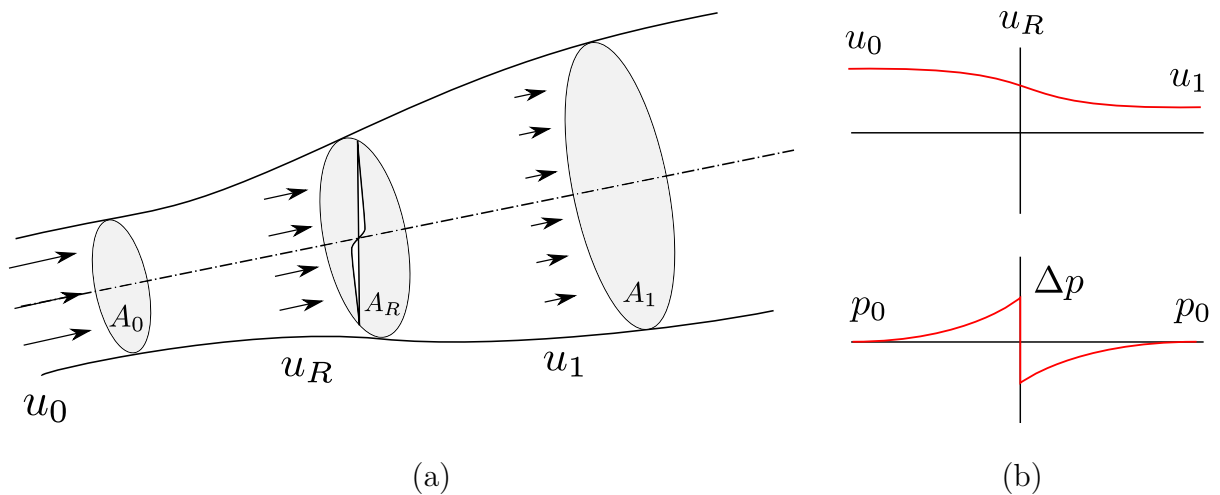


Figure 1.5: (a) Scheme of the streamtube around a rotor disc in a wind turbine configuration. The arrows represent the 1D momentum theory velocities. In solid grey, the circular areas of the stream tube upstream, downstream and on the rotor position. (b) Velocity and pressure distributions along the axial direction.

models are commonly used. In this chapter, the momentum theory and the vortex theory will be introduced. Concerning the wake description, in addition to uniform axial flow hypothesis, no time dependence will be considered in this work. Viscous effects, as shear of dissipation phenomena, will be also neglected.

1.2.2 Momentum theory

The axial momentum theory was originally developed by Rankine (1865), W. Froude (1878) and R.E. Froude (1889). It is simple and gives accurate predictions for propellers or wind turbines. For this reason, it is one of the most commonly used theories for wind turbines development. It is based on several strong assumptions. The analysis is one-dimensional. It considers the flow as uniform at each axial position in the streamtube, so the velocity and the thrust force are homogeneous over the rotor. The rotor disk is considered infinitely thin and it does not offer any resistance to the fluid passing through. That way, it can be analyzed just as an actuator that accelerates or decelerates the flow inside the streamtube. The flow is considered inviscid, steady and incompressible. A brief analysis of the theory will now be presented, showing the main expressions and variables. A deeper analysis of this theory can be found in Sørensen (2016).

Applying mass conservation, the mass flow rate has to be constant at each cross section of a stream tube surrounding the rotor disk (figure 1.5a). Assuming incompressibility, this implies the flow rate is conserved:

$$uA = \text{Cst}, \quad (1.1)$$

where A is the area of an arbitrary cross-section and u is its relative axial velocity. So, for wind turbines, while the flow is slowed down, the streamtube is expanded. On the other hand, for propellers, the flow is accelerated while the streamtube enveloping the rotor is contracted.

Particular assumptions are made for pressure distribution. Far upstream and downstream, it is supposed to be equal to the undisturbed ambient pressure (figure 1.5b). The net action of the lateral pressure acting on the stream tube is zero. Then, applying Bernoulli's equation at both sides of the rotor, the total pressure drop is given by

$$\Delta p = \frac{1}{2}\rho(u_0^2 - u_1^2). \quad (1.2)$$

This pressure drop is supposed to be uniform all over the rotor area, so the thrust and power extraction are simply obtained as:

$$T = \Delta p A_R = \frac{1}{2}\rho A_R (u_0^2 - u_1^2), \quad (1.3)$$

$$P = u_R T = \frac{1}{2}\rho A_R u_R (u_0^2 - u_1^2). \quad (1.4)$$

According to assumptions imposed for the pressure and assuming an inviscid, incompressible and steady flow, one can deduce the velocity across the rotor as the mean value between upstream and downstream velocities:

$$u_R = \frac{1}{2}(u_0 + u_1). \quad (1.5)$$

An important characteristic of a rotor that can be deduced from momentum theory is the axial interference factor, which can be defined as the ratio of the undisturbed external flow velocity to the total flow velocity behind the rotor:

$$a = \frac{u_0 + u_R}{u_0}, \quad (1.6)$$

so velocities in the far wake and in the rotor plane can be reformulated as $u_1 = (1 - 2a)u_0$ and $u_R = (1 - a)u_0$. This permits to give an expression of power extraction in terms of the axial interference factor:

$$P = 2\rho A_R u_0^3 a(1 - a)^2. \quad (1.7)$$

It is also very common to use of the so-called power coefficient, which gives a non-dimensional value for the power extracted by the rotor:

$$C_P = \frac{P}{\frac{1}{2}\rho A_R u_0^3} = 4a(1 - a)^2. \quad (1.8)$$

Then, differentiating with respect to a , a maximum theoretical obtainable power $C_P^{\max} = 16/27 = 0.593$ for a value of $a = 1/3$ is deduced. This is known as the Betz limit, it implies that only the 59.3% of the kinetic energy of the flow inside a stream tube of the same diameter of the disk can be transformed to useful work by the rotor. In addition, this is just a conservative limit that does not take into account the losses related to dissipation processes. Moreover, rotation has not been considered here. This can be included in Momentum theory as explained for instance in Sørensen (2016).

Momentum theory gives very useful results to predict the behaviour of the flow in wind turbines or climbing flight regimes, however, it cannot predict many practical effects. Although it has progressively been modified to consider the presence of multiple blades, the influence of the vortical wake or three-dimensional effects (see Sørensen, 2016), it assumes a particular topology of the flow streamlines that is not always satisfied. The observed regimes where the flow is not uniform at each cross section or when it changes direction, as it occurs in descending flight and Vortex Ring State, cannot be described by the Momentum theory. For these situations, different methods have to be used to describe the flow — one of them is presented in the next section.

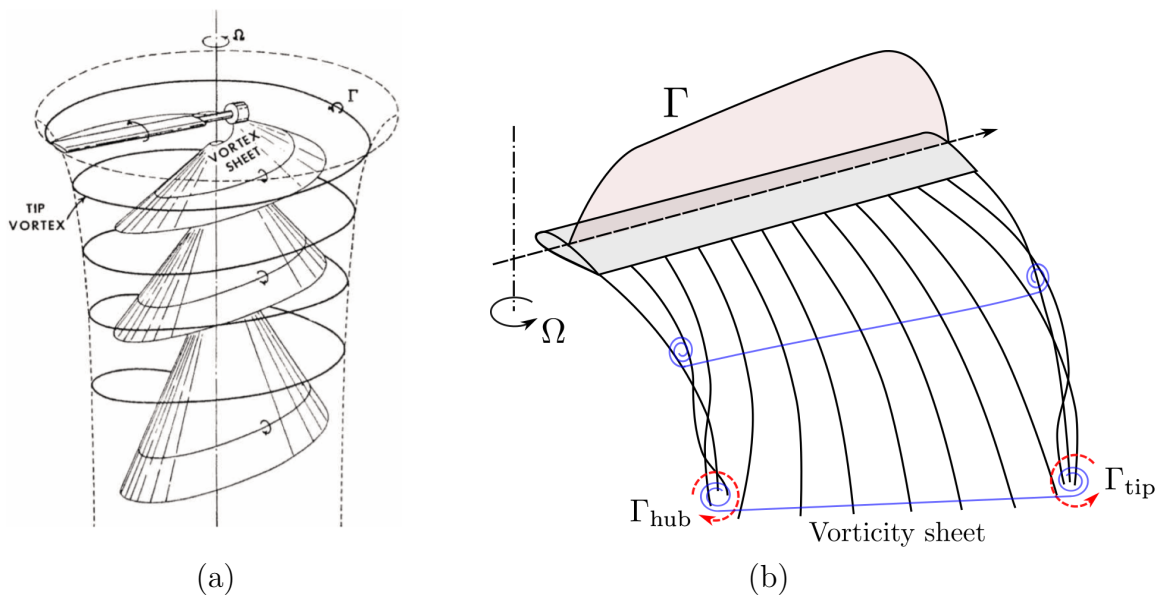


Figure 1.6: (a) Wake generated by a rotating blade during hovering regime with a developing vorticity sheet and an helical tip vortex (Gray, 1956). (b) Circulation profile along a blade. Tip and hub vortices are rolled-up behind the ends of the blade. In the middle, a vorticity sheet is shed.

1.2.3 Vortex methods

The pressure difference between both sides of the blades –the pressure- and the suction-side– generates vorticity at the trailing edge and the tip of the blade. The actual distribution of vorticity on the blade and the wake is quite complex and difficult to compute. It is normally composed of a vorticity layer emitted from the edge of the blade and two vortices shed from the tip and the hub (figure 1.6). Vortex methods assume a description of the wake in terms of vortex elements such as blobs, filaments or sheets. The vorticity of these elements is calculated from the circulation distribution along the blade.

Two main strategies can be followed to calculate the structure of the wake: either use a free-vortex method, where the wake is free to evolve according to the Biot-Savart law, or prescribe a vorticity shape.

In the Betz (1926) model, the wake is prescribed to be a single uniform helical vorticity sheet detached from each blade (figure 1.7a). These vorticity interdigitated sheets are simply advected downstream and are assumed to have a constant pitch. Another well known model was presented by Joukowski (1929), which was first used for the design of propellers. In this case, all the vorticity created along the blade is instantaneously concentrated into two vortices per blade, one at the tip and one on the axis (figure 1.7b). The strength of the vortices is given by the circulation Γ of the flow around the blade. In the Joukowski model, the circulation Γ is assumed to be constant all along the wake.

Numerous examples can be found in the literature where the relevance of this model is demonstrated. In figure 1.8 three examples are shown, from a wind turbine, a helicopter and a boat propeller, where the tip vortices are perfectly visible.

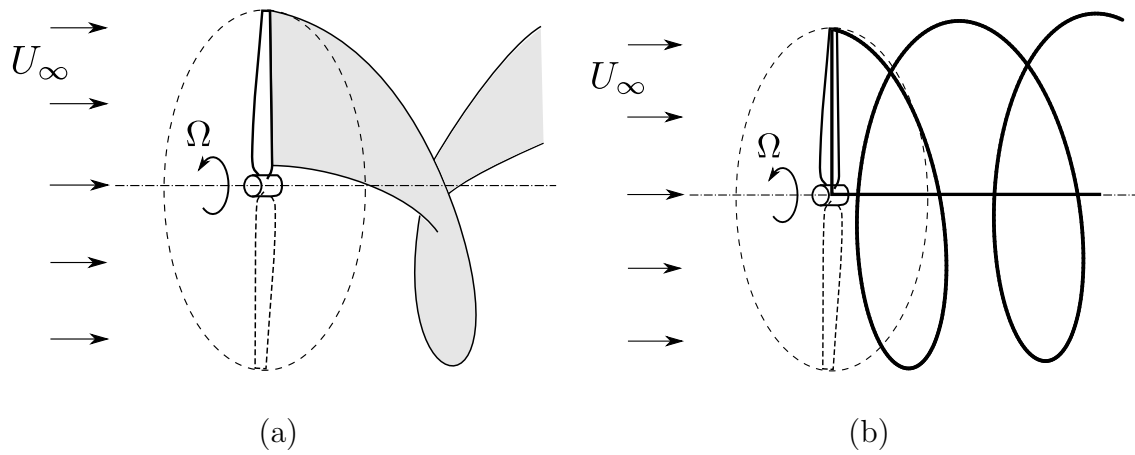
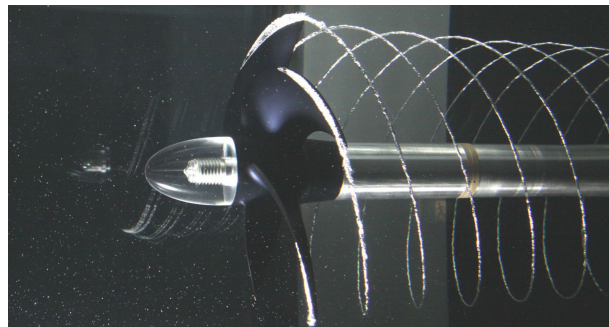


Figure 1.7: Rotor wake models proposed by (a) Betz (1926) and (b) Joukowski (1929).



(a)



(b)



(c)

Figure 1.8: Examples of visualization of the tip vortex in (a) a wind turbine (from Vermeer *et al.*, 2003) (b) a boat propeller (Cavitation Research Laboratory/AMC) and (c) a Bell AH-1 Cobra helicopter

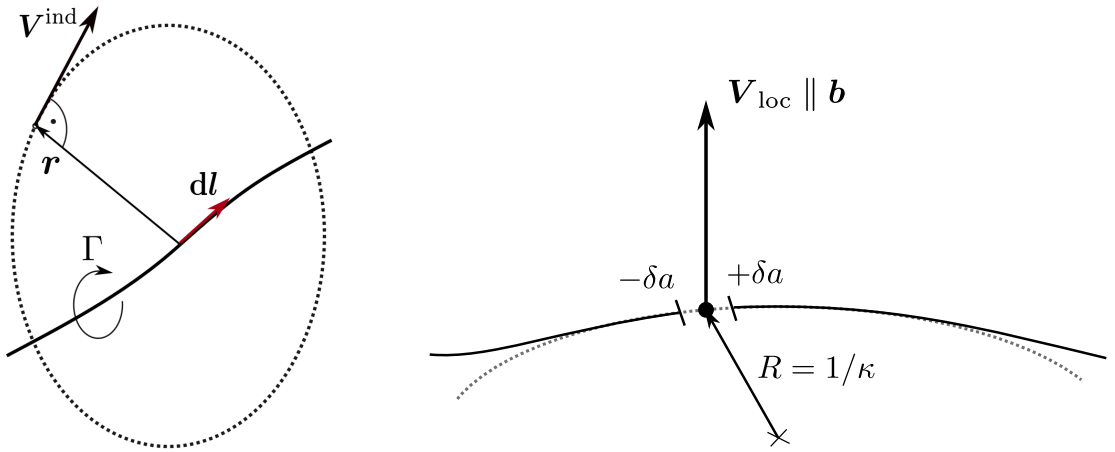


Figure 1.9: (a) Schematic of the velocity induced by a vortex filament of circulation Γ at a distance r . (b) Schematic of the local self-induced velocity of a vortex filament and the cut-off length δa . In dotted line, the circle osculating the filament at the point where self-induction is being calculated.

In the free-vortex methods, the geometry of the vortex elements forming the wake is calculated in the time domain, providing a much more precise structure than that of the prescribed shape models. In many practical problems, viscous effects can be neglected and an inviscid approach can be used. In this framework, vortex elements move cohesively as material elements with the local fluid velocity, giving the fundamental equation for the free-vortex method:

$$\frac{d\mathbf{r}}{dt} = \mathbf{V}(t, r), \quad (1.9)$$

where $\mathbf{r}(t)$ is the position of a point of the vortex element in a time.

The local velocity \mathbf{V} is the sum of the external velocity field and the velocity induced by the vortical elements. This contribution is given for a vortex filament of circulation Γ_j by the Biot-Savart law (figure 1.9):

$$\mathbf{V}_j^{\text{Ind}} = \frac{\Gamma_j}{4\pi} \int \frac{\mathbf{r} \times d\mathbf{l}}{|\mathbf{r}|^3}, \quad (1.10)$$

where $d\mathbf{l}$ is the differential element of the vorticity filament. The total induced velocity is obtained as the sum of the induction of all the vortical elements. The main difficulty of the Biot-Savart formula is the presence of a singularity at the position of the vortex element. To resolve this issue, different techniques have been developed in the literature (this will be treated in detail in section 2.1). One of the most commonly used is the cut-off method (Thomson, 1883; Crow, 1970). The idea of this method is to exclude a portion of the filament on both sides of the singularity in the Biot-Savart integral. The length of each portion is proportional to the vortex core size a and it is called cut-off length δa . The proportional factor δ depends on the characteristics of internal structure of the vortex (for details about the calculation of δ , see Saffman, 1992).

By applying the cut-off method, a simple asymptotic expression can be derived for the

self-induction of a curved filament of vorticity due to the effect of its local curvature:

$$\mathbf{V}_{\text{loc}} = \frac{\Gamma}{4\pi} \kappa \mathbf{b} \log \frac{L}{\delta a}, \quad (1.11)$$

where κ is the local curvature of the filament and L is the length of integration from both sides of the considered point. This expression is the so-called Local Induction Approach (LIA). It is the leading order approximation in the limit $a/L \rightarrow 0$. It clearly demonstrates that the self-induced velocity of a curved filament diverges as its core size goes to zero. It is also mainly directed along the binormal direction \mathbf{b} of the filament (figure 1.9).

The velocity surrounding a vortex element, coming from an external flow or self-induction, in general, displaces and deforms vortical structures. Only a few vortex structures, like vortex rings or helices, have the particularity to move without changing shape (this property will be discussed in section 2.3). In this work, we will be interested in this kind of structures, looking for structures that are stationary in an adequate frame. In the context of rotors, the frame will be moving with the blades.

Free and constrained wake approaches (Leishman, 2006; Bhagwat & Leishman, 2000; Bliss, 1993) are examples of numerical studies using the Biot-Savart law. The main advantages of vortex methods are that they give accurate approximations for the wake while they are easy to compute and in general much less computationally costly than direct numerical simulations. However, they suffer from stability problems and they can also become very expensive if a high number of elements is used. A good way to have a simple and relatively efficient description of the wake is to use the free-vortex method procedure with a reduced vortex model involving only a few vortices as the Joukowski model (Gupta & Leishman, 2005b).

1.3 Aerodynamic loads

1.3.1 An introduction to airfoil aerodynamics

Since the first successful airplanes flights in the early 1900's, aerodynamics have always been the object of active research. One of the most important contributions to airfoil aerodynamics was devised by Prandtl through the Lifting line theory in the end of the 1910's — this theory will be discussed later in detail. Shortly after, the thin airfoil theory was one of the first theories that described the lift force on an airfoil. It was formulated in the 1920's by Max Munk (Munk, 1924) and later improved by Glauert (1926), and gave a first relation between lift and the angle of attack for incompressible inviscid flows. The theory is two-dimensional and assumes an airfoil of zero thickness. It gives a purely linear relation between lift and the angle of attack, so it does not account effects such as the stall of the airfoil, that typically occurs for an angle of attack between 10° and 20° (see figure 1.11b). In spite of its simplicity, the thin airfoil theory permitted important research developments and was the basis of future achievements in airfoil aerodynamics. Review of these progresses can be found in Abbott & Von Doenhoff (1960), Kuethe & Chow (1976) or Katz & Plotkin (1991).

The difference of pressure of a flow between both sides of a 2D airfoil generates a force that depends on the geometry of the airfoil and on the properties (density and velocity)

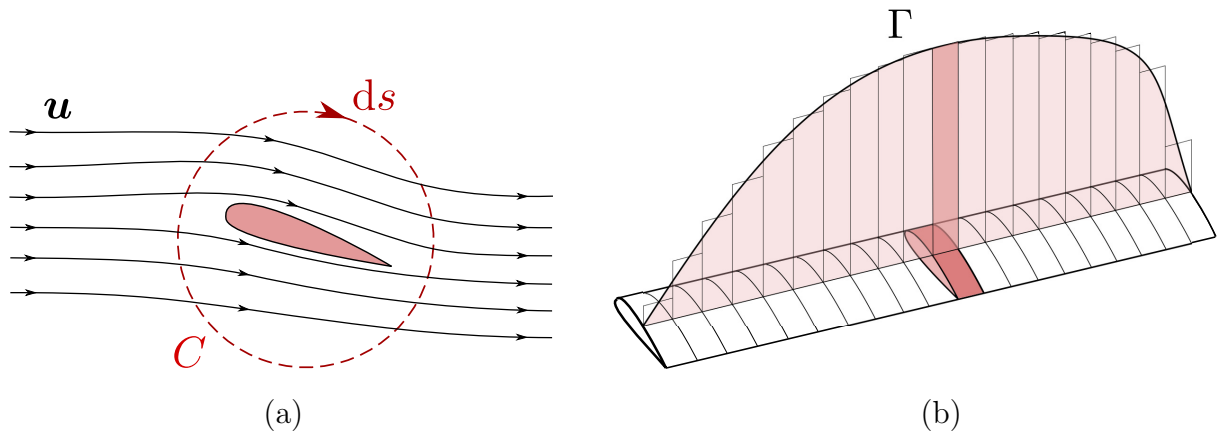


Figure 1.10: (a) 2D airfoil under an external flow \mathbf{u} . The dashed line circle C represents a closed line surrounding the airfoil with a differential of length ds . The integration of the velocity field \mathbf{u} along the closed line C gives the circulation Γ around the profile. (b) Scheme of the lifting line theory. The circulation $\Gamma(r)$ along the wing is computed applying Kutta-Joukowski law at every 2D element.

of the flow. This force can be decomposed into lift F_L , acting perpendicularly to the flow direction, and drag F_D , in the same direction as the flow. For a 2D airfoil, Kutta-Joukowski law links the lift force with the circulation Γ around the airfoil, the density of the fluid ρ and the speed of the airfoil U through:

$$F_L = \Gamma \rho U. \quad (1.12)$$

This law is conceived for two-dimensional potential flows, that is, inviscid, incompressible and irrotational, however, it is still a good approximation for real viscous flows in typical aerodynamic applications. To apply it in real flows, it is specially important to have a smooth merging between the fluid coming from upper and lower surfaces, without fluid circulation near the trailing edge of the airfoil. This is known as the Kutta condition and it is normally guaranteed with a sharp trailing edge and moderated angles of attack (Kuethe & Chow, 1976).

Using Kelvin's circulation theorem, the circulation can be mathematically defined as the integral of the velocity field \mathbf{u} around a closed contour C surrounding the airfoil (figure 1.10a):

$$\Gamma = \oint_C \mathbf{u} \cdot d\mathbf{s}. \quad (1.13)$$

In real flows, even when viscous effects are very weak, there always exist a narrow viscous boundary layer around the airfoil. To apply Kutta-Joukowski theorem, the closed line surrounding the airfoil must be located outside the boundary layer.

For a straight airfoil of length l and chord c , lift and drag forces are related to the properties of the flow felt by the blade through the so-called lift and drag coefficients, which depend exclusively on the geometry of the airfoil:

$$C_L = \frac{2F_L}{\rho U^2 c l}; \quad C_D = \frac{2F_D}{\rho U^2 c l}. \quad (1.14)$$

These two coefficients are crucial in applied aerodynamics. They are used to predict the aerodynamic forces on a specific airfoil under particular flow conditions. In figure 1.11b, it is illustrated a typical distribution of C_L and C_D as a function of the angle of attack α for a NACA0009 profile (from Abbott & Von Doenhoff, 1960). This distribution changes with Reynolds numbers, so several tables are normally given for an specific airfoil geometry. Historically, the coefficients have been determined experimentally in wind tunnel tests for different airfoil geometries (Jacobs *et al.*, 1935). Numerous compilations can be found in the literature with lift and drag coefficients data of the most commonly used airfoils (Abbott & Von Doenhoff, 1960).

The relation between circulation and lift extracted from Kutta-Joukowski formula can be finally reformulated to obtain a simple expression for the circulation that includes the lift coefficient:

$$\Gamma = \frac{1}{2}cUC_L. \quad (1.15)$$

This formula is *a priori* valid just for 2D airfoils. A very useful and simple model to compute the circulation of a 3D airfoil is based on treating it as a series of 2D elements (see figure 1.10). This is the case of the lifting-line theory (Prandtl, 1921), which assumes that any section of a finite wing experiences the same lift as an equivalent section of a infinite wing with the same uniform circulation. The circulation profile is then calculated by applying Kutta-Joukowski formula (1.15) to each section of the wing (figure 1.10b). This model takes into account the variation of the blade geometry and the flow properties along the wing so some 3D effects are taken into account in the circulation and aerodynamic loads distribution. However, the method is not powerful enough to capture more complex phenomena as tip and root losses (Leishman, 2006). Nevertheless, the lifting-line theory approach has been widely used and improved, for example, to adapt it to wings with arbitrary camber or sweep angle (Phillips & Snyder, 2000).

The same principle of the lifting-line theory to obtain load distributions on finite wings is specifically applied to rotors in the Blade Element Theory.

1.3.2 Blade element theory

Due to its simplicity and efficiency, the Blade Element Theory (BET) is one of the most commonly used theories to estimate the aerodynamic loads on the blades of a rotor. This theory was apparently proposed for the first time by Drzewiecki (1920) (see Leishman, 2006) for the analysis of airplane propellers. Later, Glauert (1935) further developed the theory by calculating the induced velocity on the rotor blades and applying it to the analysis of wind turbines. Applications to the helicopter rotor were also extensively made during the twentieth century (Payne, 1959; Bramwell, 1976; Johnson, 1980; Prouty, 1986). Nowadays BET is still used for the design of helicopter (Leishman, 2006) and wind turbine rotors (Hansen, 2015).

BET assumes that each blade section behaves as a quasi-2D airfoil: it locally produces aerodynamic forces and moments. The analysis of a blade then provides a radial distribution of the aerodynamic loads along the blade. As for the 2D lifting-line theory, three dimensional effects like tip loss are not included in BET. Specific corrections have been computed to account for these effects in rotors (Prandtl & Betz, 1927; Shen *et al.*, 2005; Sørensen, 2016).

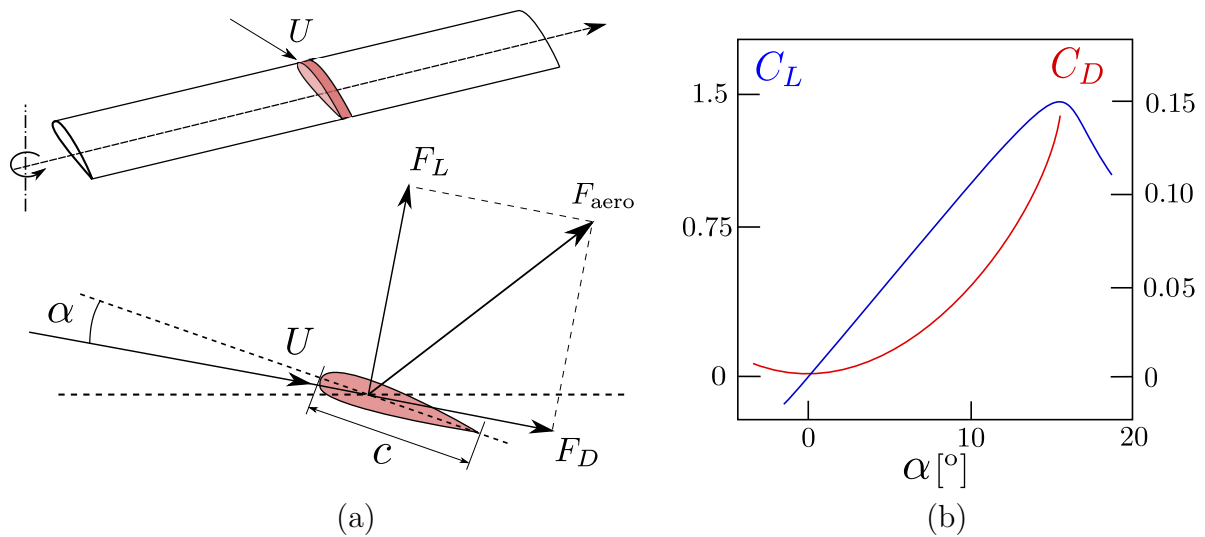


Figure 1.11: (a) Scheme of the Blade Element Theory. The aerodynamic loads are calculated at each element of the blade from the effective velocity U received. (b) Example of a typical distribution of lift and drag coefficients (Here for NACA0009 airfoil, from Abbott & Von Doenhoff (1960)).

Each blade element is studied independently, calculating the amplitude U and orientation (angle of attack α) of the local velocity (figure 1.11). This local velocity is composed of two main contributions: the external flow and the flow induced by the wake. In free vortex methods, the induced flow is computed through Biot-Savart law.

Now, the contributions to lift and drag per unit of span associated with each element can simply be derived from Kutta-Joukowski as:

$$F_L(r) = \frac{1}{2}\rho U^2 c C_L, \quad F_D(r) = \frac{1}{2}\rho U^2 c C_D. \quad (1.16)$$

These formulas give a very simple way to calculate aerodynamic forces. In practice, it is just necessary to compute the local velocity and the angle of attack, then C_L and C_D are directly obtained from tabulated data. In rotor blades, local velocity is mainly governed by the rotation of the blades, so contrary to airplane wings, Reynolds numbers may change from tip to hub. In this work, this effect will not be considered, and we shall use the Reynolds number at the tip to choose lift and drag coefficients distributions.

Once lift and drag forces distributions are computed, they can be integrated along the blades to obtain the total thrust, torque and power delivered by the rotor.

The main difficulty in BET is to estimate the local velocity U along the blades. While the external flow and the rotor angular speed are known, the induced velocity has to be calculated, so a model for the wake has to be used together with BET. Glauert (1935), de Bothezat (1919) and Reissner (1937, 1940) linked BET with the momentum theory to obtain the induced velocity distribution for the airplane propeller problem. Later, Gustafson & Gessow (1946) and Gessow & Gustafson (1948) developed a similar approach for hovering helicopter rotors. This combined theory is known as the Blade Element Momentum theory and is widely used for the design of wind turbines (Hansen *et al.*, 2006). BET has also been linked with vortical descriptions of the blades. These theories

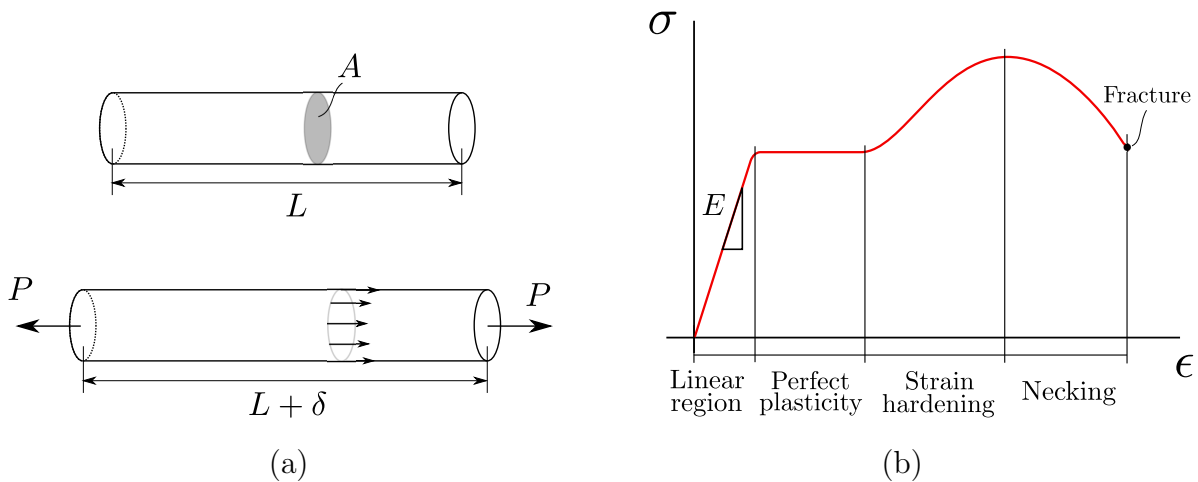


Figure 1.12: (a) Prismatic bar under an axial tension. (b) Typical stress-strain diagram for steel where most common transitions can be seen from linear elastic deformation to fracture.

have been developed from the beginning of the twentieth century by Joukowski (1929), Glauert (1922) or Lock *et al.* (1925). Betz (1920) and Goldstein (1929) developed a prescribed vortex wake theory for propellers which was later extended by Theodorsen (1948). The combination of BET with prescribed vortex wake models was also early applied to the helicopter rotor problem (Knight & Hefner, 1937).

1.4 Blade deformation

1.4.1 Mechanical properties of deformable materials

Mechanics of deformable materials is the branch of applied mechanics that studies the behaviour of solid bodies when they are subjected to different types of loading. Its principal objective is to obtain a complete mechanical description of a given structure by determining its stresses, strains and deformation when any kind of load is applied. Having a good understanding of this mechanical behavior is essential for the safe design of all types of structures, from airplanes to buildings or bridges (for reference books, see Benham & Crawford, 1976; Gere & Timoshenko, 1998).

Stress and strain are probably the most fundamental concepts in continuum mechanics, as their intrinsic relationship describes the mechanical behaviour of a material. A basic approach to these concepts can be made by analyzing the properties of a prismatic bar under an axial force.

The stress, σ , is a measure of the internal forces between particles inside a continuous material, it has units of force per unit area. Logically, the more loaded the material is, the greater these internal forces are. If we consider a prismatic bar of cross section A under a pure axial force P (figure 1.12a), stress is defined as

$$\sigma = \frac{P}{A}, \quad (1.17)$$

that we suppose uniformly distributed over the cross section area.

On the other hand, the strain, ϵ , is a non-dimensional measure of the deformation of the material. Under an axial load, a straight bar of length L will be shortened or lengthen a distance δ , depending on whether the load is compression or traction. Then, strain is defined as

$$\epsilon = \frac{\delta}{L}. \quad (1.18)$$

Strain can also be described laterally, as a lateral contraction occurs when the bar is elongated or an expansion when compressed.

To understand the behavior of a particular material and employ it in a design problem, it is important to know the intrinsic relation between stress and strain. This relation is illustrated in stress-strain diagrams. A typical strain-stress diagram of steel is shown in figure 1.12b. Initially, when the applied load is further increased, there is a linear relation between strain and stress and the material has an elastic behaviour, where deformation is completely reverted if load is removed. However, if load is still increased, the material becomes plastic, the deformation continues at constant stress and it remains even if load is removed. After that, if loading is increased, plastic deformation continues with a non-linear variation of σ before a great slimming of the material (necking) and, finally, its fracture. Depending on the material, the regions of the diagram can completely change, being enlarged or reduced. In this work, we are interested in the linear region and an elastic behaviour will always be supposed for rotor blades.

Staying in the elastic region, the description of the mechanic behaviour of the material is greatly simplified and it can be described by just two parameters: Young's modulus E and Poisson ratio ν .

Young's modulus describes the linear relationship between stress and strain in the elastic region (figure 1.12b). It is defined by the well known Hooke's law:

$$E = \frac{\sigma}{\epsilon}, \quad (1.19)$$

Poisson ratio describes how much a material is laterally contracted when axially elongated:

$$\nu = -\frac{\text{lateral strain}}{\text{axial strain}} \quad (1.20)$$

These two properties are easy to measure by applying a pure axial traction on a prismatic bar. Once the elastic properties of the material are determined from a experimental test, they can be used to calculate the deformation of more complex geometries. For that, stress and strain distributions have to be computed for the whole structure.

1.4.2 Beam model

The computation of the deformation of a blade can be very complex if the whole elastic problem is addressed, calculating numerically the strain-stress coupled problem. In addition, if a fluid-structure coupling is considered, the numerical resolution of the problem is even more costly (Bazilevs *et al.*, 2011).

For this reason, most models for wings and rotor blades take advantage of their slenderness to apply the so-called beam theory (Bauchau & Craig, 2009), which implies an

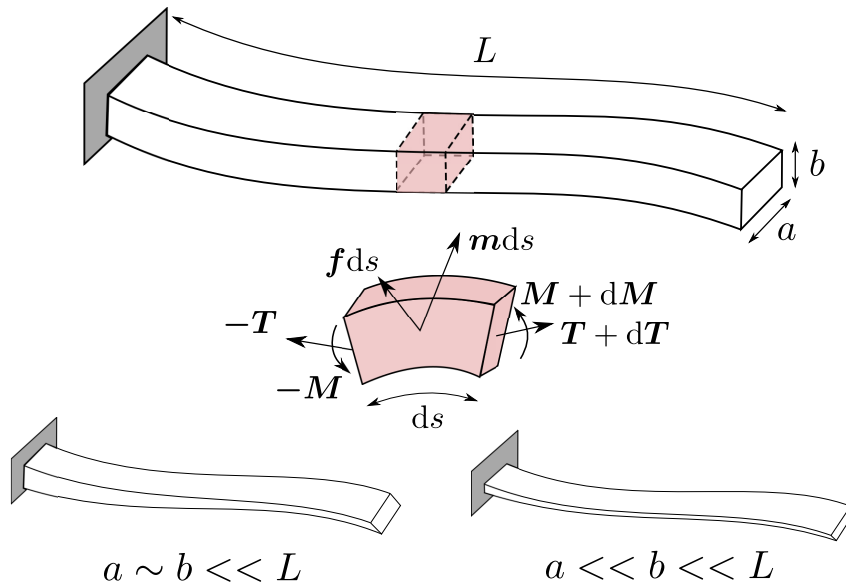


Figure 1.13: Upper: Internal and external forces and moments exerting on a chunk of beam. In the classical Euler-Bernoulli beam theory the length of the beam has to be much bigger than the rest of dimensions. Lower: asymptotic limits of rod ($a \sim b \ll L$) and ribbon ($a \ll b \ll L$) models.

important simplification in the resolution. This theory describes the deformations of the blade through 1D equations along the centerline, bringing a great reduction of the computation cost. In the seventieth century, Jacob Bernoulli (1654-1705) first postulated the principles of the theory, later, Daniel Bernoulli (1700-1782) and Leonhard Euler (1707-1783) extended the theory by formulating the differential equation for the motion of a vibrating beam and analyzing the deformation of the beam under different loading conditions (see Han *et al.*, 1999). Later, Timoshenko (1922) improved the theory including shear deformation and rotational bending effects.

The theory is applicable to linear elastic problems and is based on several assumptions concerning the cross section of the beam: it is infinitely rigid in its own plane, it remains plane after deformation and it is always normal to the deformed axis of the beam (Bauchau & Craig, 2009). Under these hypotheses, a force and momentum balance is made at every section of the beam. In figure 1.13, the forces and moments involved in the balance of a small section of beam are represented. \mathbf{T} and \mathbf{M} are the internal forces and moments and \mathbf{f} and \mathbf{m} are the external forces and moments per unit length. Applied to a flexible rotor, the blades can be modeled as cantilevered beams where the external forces are the aerodynamic loads, the weight of the blades and centrifugal force. One of the advantages of beam theory is that it allows the computation of both static and dynamic problems. In our case, we will use it to obtain static blade deformation equilibrium.

The link between forces and moments on the structure with the elastic properties of the material is given by a constitutive relation, relating E and ν with the internal moments of the beam. For that, in addition to the hypothesis of slenderness (the span is bigger than the other lengths of the beam) some other geometrical assumption has to

be made. Different asymptotic limits can be considered (see Carrera *et al.*, 1926), each one with its own constitutive relation. Two of the most common models are rod and ribbon (figure 1.13). The combination of force and moment balance with the constitutive equation permits to calculate beam bending and torsion.

The rod model (Dias & Audoly, 2014) is the simplest one, it assumes that the length of the blade is very large compared to the other dimensions involved in the problem. The constitutive law gives a linear expression for the internal moment in terms of the local torsion and bending. In this case, torsion and bending are not intrinsically coupled, which gives an important simplification to the problem.

For the ribbon model (Volovoi *et al.*, 2001; Dias & Audoly, 2015), the height of the cross section of the beam is supposed to be small compared to its width. In this case, the constitutive law becomes more complicated, yielding an intrinsic non-linear coupling between bending and torsion.

Independently of the intrinsic characteristics of the model, in flexible rotors there is always a coupling between bending and torsion because of the effect of aerodynamic loads: when a blade twists or bends, it changes its position with respect to the flow, this produces a variation of the aerodynamic loads and, in turn, of twisting and bending. A number of authors have shown that it is possible to take advantage of this coupling and improve rotors adaptability to non-optimal operational conditions. Two possible strategies can be used to exploit the coupling: active (i.e. forcing blade twist to obtain a bending response) or passive (using just the natural coupling given by the blade geometry), which is the most common due to its simplicity and economy. The effect of coupling has been analyzed to improve the performance of different kinds of rotor devices, from wind turbines (Maheri & Isikveren, 2010) to drones (Lv *et al.*, 2013). As an example, load mitigation in wind turbines is one of the possible applications of the bending-twisting coupling, which can be useful to reduce fatigue damage on the blades (Lobitz & Veers, 2003; Bottasso *et al.*, 2013).

1.5 A note on fluid-structure interactions

As it was exposed in the previous sections, for a given rotor, the circulation along the blades can be obtained only if the flow in the rotor plane is known. However, as this flow also depends on the circulation distribution, the wake-rotor problem is always coupled, even for a rigid rotor. Additionally, for the flexible problem, the aerodynamic forces and the deformation of the blades also depend on the flow in the rotor plane; any change of position of the blades modifies the geometry of the wake and consequently the induced flow, so blade deformation increases the coupling. In conclusion, a strong fluid-structure coupling is in the core of the flexible rotor problem.

1.6 Helical vortices in a rotor wake

For a N blade rotor, the Joukowski (1929) model exhibits in the far-wake a uniform helical braid composed of N vortices of circulation Γ (plus a central vortex of circulation $-N\Gamma$). These perfect helical vortex solutions have been the subject of numerous works since the

early works by Kelvin (1880), Da Rios (1916), Levy & Forsdyke (1928) and Joukowski (1929).

For instance, Betchov (1965) and Kida (1981) showed using the local induction approximation that these structures rotate and translate without changing form. When the vortex is (infinitely) thin, Hardin (1982) and Kawada (1936) (see Fukumoto *et al.*, 2015) provided an exact expression for the induced velocity field inside and outside the cylinder containing the helix. Ricca (1994), Kuibin & Okulov (1998) and Boersma & Wood (1999) showed how the singularity of Hardin expression can be extracted to compute the self-induced motion of the helix. Velasco Fuentes (2018) recently applied these results to compute the motion of vortex elements on a helical vortex, emphasizing the role of tangential velocities. In these works, the vortex core size is implicitly assumed to be a small parameter. Lucas & Dritschel (2009) and Selçuk *et al.* (2017) have shown how helical vortices with a thick core can be obtained numerically by enforcing the helical symmetry in the governing equations.

Solutions with more complex geometries are scarce in the literature. Walther *et al.* (2007) looked at equilibrium solutions composed of undeformed helical vortex pairs of same pitch but different radius. They demonstrated that undeformed helical vortex pairs of identical pitch and opposite circulation were possible for a particular radius ratio. This analysis was further pursued by Okulov (2016) for helical vortices with same sign circulation. Reducing the framework to nearly parallel filaments (Klein *et al.*, 1995), Kwiecinski & Van Gorder (2018) were recently able to provide more exotic solutions.

1.7 Stability of wake solutions

The stability of a dynamical system makes reference to its response to small perturbations. A particular system, in our case, the wake generated by a rotor in a certain regime or a blade deformed under aerodynamic loads, is stable if it comes back to its original equilibrium state after being excited with a small perturbation. On the other hand, if the perturbation is amplified in time, the system is unstable. In this section, several instabilities concerning vortical wakes will be discussed.

Pairing instabilities

Among the various instabilities occurring in the context of vortex dynamics, the pairing instability, that is the spontaneous grouping by pair of vortices, is probably the most important one. This instability was first described in the context of 2D point vortices.

Crow instability (Crow, 1970) is a 3D version of the pairing instability that appears in the wake of airplanes. It results from the 3D interactions of the counter-rotating vortex pair that is generated by the airplane. It leads to the deformation of the vortices that ultimately touch, reconnect and form an array of vortex rings (figure 1.14).

Short and long-wave instabilities in helical vortices

Two kind of instabilities can be found in infinite helical vortices: long-wave and short-wave instabilities (Leweke *et al.*, 2014).

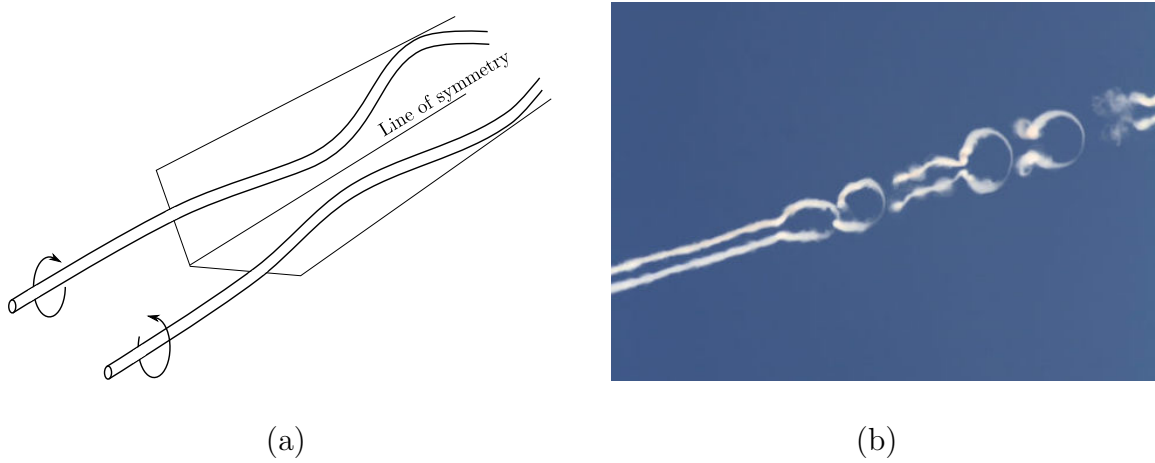


Figure 1.14: (a) Scheme of two parallel counter-rotative vortices developing a symmetric Crow instability mode. (b) Chain of vortex rings of a Crow instability

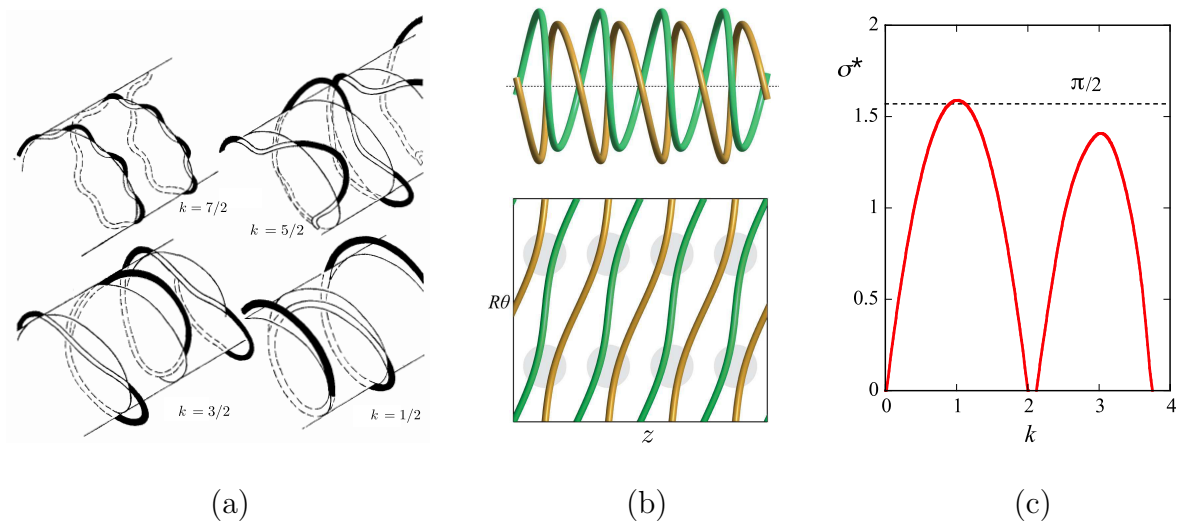


Figure 1.15: (a) Long wave instability results for a single helical vortex obtained by Widnall (1972). Displacement prediction for several wavelength perturbations. (b) Three dimensional view on the left and developed plan view on the right of the unstable mode associated with $k = 1$ for a pair of helical vortices (from Quaranta, 2017). (c) Growth rate of symmetric modes as a function of the wavenumber k for a pair of helical vortices. Theoretical distribution from Gupta & Loewy (1974) expressions.

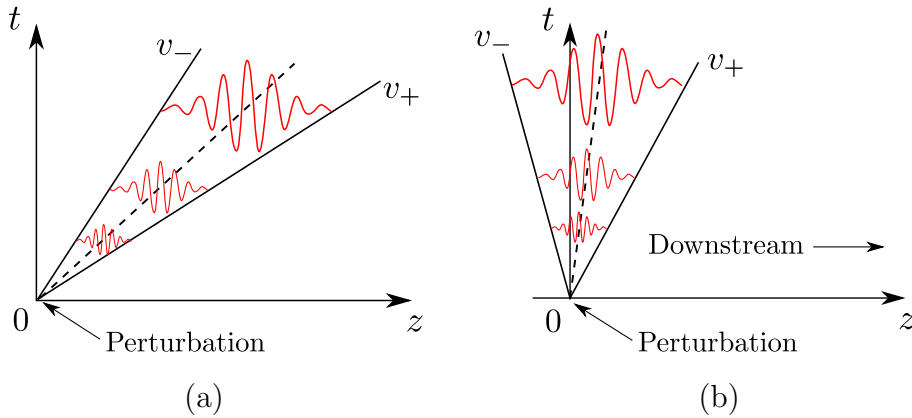


Figure 1.16: Spatio-temporal evolution of a perturbation (a) convectively and (b) absolutely unstable.

For long-wave instabilities, the wavelength of the perturbations is large compared to the vortex core. The vortices are locally displaced as a whole, without changing the internal core structure. This will be the kind of instability analyzed in this work, as the vortices are considered as filaments without taking into account possible variations on the core structure. Widnall (1972) analyzed this problem for filaments of vorticity with finite core size, finding an equivalent of Crow instability for helical vortices. She proved how long-wave instabilities become more important as the pitch of the helix decreases and the neighboring turns of the filaments begin to strongly interact generating pairing unstable modes. Some of these modes are showed in figure 1.15a. Later, Gupta & Loewy (1974), did a similar analysis for multiple interdigitated helical vortices, obtaining similar instability results. The link between the long-wave instabilities of helical vortices and the pairing instability was made by Quaranta *et al.* (2015). In figure 1.15b, a typical symmetric instability mode for a pair of helical vortices is shown. For this particular case, both symmetric and antisymmetric pairing phenomena are a priori possible. In figure 1.15c, a typical distribution of the growth rate as a function of the wavenumber of the perturbation is shown for symmetric modes.

The short-wave instabilities appear as an amplification of the perturbations inside the vortex cores. The effect of nearby vortices, or the curvature or torsion of the vortex itself, produce a deformation of the vortex core that is the source of the instability (Lewke *et al.*, 2016). Different kinds of short-wave instabilities can be found, as the elliptic instability, associated with elliptic deformation of the vortex core (Kerswell, 2002; Blanco-Rodríguez & Le Dizès, 2016), or the curvature instability, associated with the curvature induced deformation (Fukumoto & Hattori, 2005; Hattori & Fukumoto, 2009; Blanco-Rodríguez & Le Dizès, 2017).

Spatio-temporal development of a perturbation

Independently of the analysis of the geometry and growth rate of the different unstable modes, a spatio-temporal stability analysis can be performed to study its propagation along the wake (see Huerre & Monkewitz, 1985, 1990). In our case, the objective of this

kind of analysis is to determine if, for a given wake solution, the instability propagates downstream or spreads upstream and affect the flow in the rotor plane.

To study the nature of the instability, the impulse response is analyzed in the (z, t) plane (figure 1.16), where z is the direction of the flow. A particular velocity of propagation $v = z/t$ is represented in the plane as a straight line radiated from the initial location of the perturbation. In a unstable system, the perturbation is amplified but spread while it is advected downstream. Of particular interest are the rear and front velocities v_- and v_+ of propagation of the wavepacket. If there is a single wavepacket, in any frame moving at a velocity, v , such that $v_- < v < v_+$, the perturbation grows at any fixed position. Then, two different situations can occur depending on whether v_+ and v_- have the same sign or not. If they have the same sign (figure 1.16a), the instability is advected away from its source. In this case, the flow is said convectively unstable. In the other case, if v_+ and v_- have different signs (figure 1.16b), the perturbation propagates both upstream and downstream as it grows. In this case, the flow is absolutely unstable.

In the context of helicopter, it has been suggested that the transition to the VRS could be associated with a change of the local pairing instability from convective to absolute (Leishman *et al.*, 2004; Bolnot *et al.*, 2014). For this reason, we shall also consider the spatial-temporal development of the perturbations in this work.

1.8 General overview

Motivated by their industrial applications, the performance of helicopter rotors and wind turbines has been widely studied in the last century. However, the effect of the deformation has not been so analyzed or implemented for the optimization of rotor design, even though it is non negligible in many industrial applications. One of the main problems of including blade deformation in the optimization of the rotor design is the computational cost of solving the coupled fluid-structure problem, calculating the fluid dynamic problem of the wake and the elastic problem for the blade. To avoid that problem, this work presents a simplified method based on reduced models for the wake and the blades, where different hypotheses are made:

Wake

- Model: The wake geometry is calculated through a Lagrangian free-vortex method with a prescribed Joukowski model geometry. Biot-Savart law is used to compute induced velocities.
- Hypothesis: The flow is assumed inviscid and incompressible. The external flow will be uniform and aligned with the rotor axis.

Aerodynamic loads

- Model: BEM theory is used with the Kutta-Joukowski law to compute the circulation and aerodynamic forces distribution along the blades.

- Hypothesis: As for the wake, inviscid and incompressible flow is assumed. For the computation of lift and drag coefficients, the dependence on Reynolds number along the blades is not taken into account, the value at the tip is used.

Blades deformation

- Model: Beam theory is applied combined with a rod model to compute the deformation of blades.
- Hypothesis: Linear elastic properties are assumed, as well as all beam theory conditions concerning cross section.

At all levels steadiness is imposed, looking for stationary solutions for the whole coupled problem.

In chapter 2, the model for the wake is analyzed. Two different models are presented and compared: a classical Joukowski model, where two vortices are detached per blade, one at the tip and one at the axis, and a generalized Joukowski model where the central axis is not located on the axis but displaced on the blade. Both models are compared with experimental and numerical results. Then, in chapter 3, a stability analysis is presented for Joukowski model solutions in several rotor regimes, comparing it with analytical results from the bibliography. An analysis of the convectively/absolutely unstable solutions is also presented, identifying the regimes where this transition occurs.

In chapter 4, Kutta-Joukowski law and blade element theory are applied to obtain the circulation profile and the aerodynamic forces exerted along the blade. A particular methodology is presented to calculate the circulation of the wake vortices from the circulation profile on the blade. The solutions obtained for the wake in chapter 2 are used to calculate the flow in the rotor plane. The numerical results obtained from the present model are compared to numerical and experimental results found in the literature

Finally, in chapter 5, the models for the blade deformation are developed and coupled with the induction effect from the wake. A strong fluid-structure coupling is implemented, looking for a convergence between the stationary solutions for the wake structure and the blade deformation.

Chapter 2

Wake model

Contents

| | | |
|------------|---|-----------|
| 2.1 | Chapter overview | 30 |
| 2.2 | Generalized Joukowski model | 30 |
| 2.3 | Far-wake solutions | 31 |
| 2.3.1 | Vortex filament framework | 31 |
| 2.3.2 | Deformed helical vortex pairs | 39 |
| 2.3.3 | Analysis of the effect of a varying core size | 50 |
| 2.3.4 | Discussion in the context of rotors | 50 |
| 2.4 | Near-wake solutions | 53 |
| 2.4.1 | Framework | 53 |
| 2.5 | $R_b^* = 0$ case (Standard Joukowski model) | 55 |
| 2.5.1 | Framework | 55 |
| 2.5.2 | Wake solutions | 56 |
| 2.5.3 | Induced velocities | 60 |
| 2.5.4 | Energy extracted by a wind turbine | 65 |
| 2.6 | $R_b^* \neq 0$ case (Generalized Joukowski model) | 67 |
| 2.6.1 | Topology of the solutions | 67 |
| 2.6.2 | Parametrical analysis | 68 |
| 2.6.3 | Comparison with the standard model | 74 |
| 2.7 | Chapter conclusion | 76 |

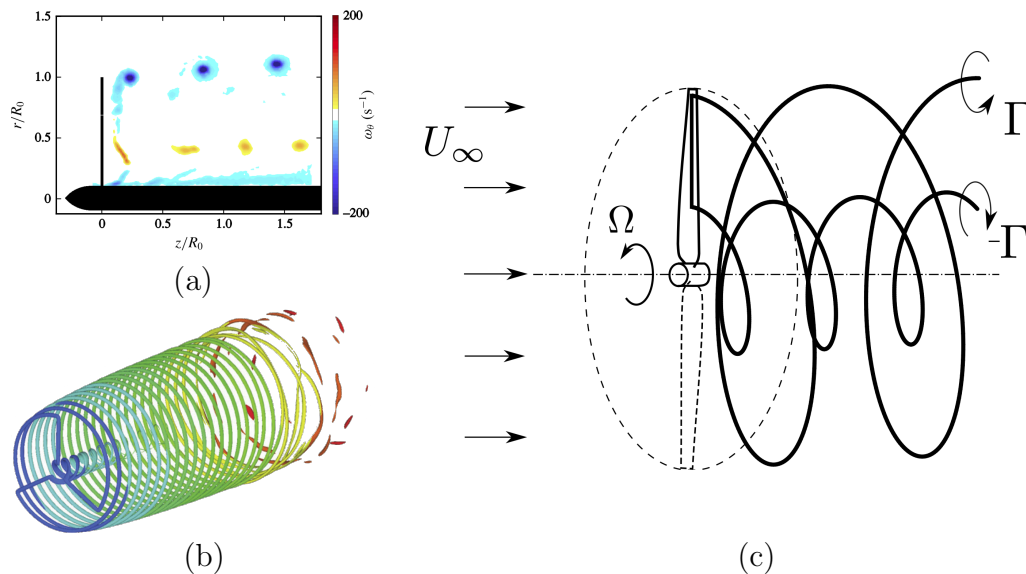


Figure 2.1: (a) PIV visualization of the wake generated by a rotor in wind turbine regime (Quaranta *et al.*, 2015). In yellow, it can be observed the hub helical vortex. (b) Numerical calculation of a three-bladed wind turbine wake from Ivanell *et al.* (2010) using the Actuator Line Method. (c) Scheme of the generalized Joukowski rotor model. To simplify the figure, only the vortices detached from a single blade are represented.

2.1 Chapter overview

In this chapter a free-vortex method is applied to a prescribed Joukowski rotor model to obtain the geometry of the wake. Stationary solutions are obtained in a frame that rotates with the blades for given values of tip-speed-ratio, vortex circulation and vortex core size. A generalized Joukowski model is presented where the hub vortex is not necessarily located on the axis. Contrary to the classical Joukowski model, where far-wake solutions are perfect helices, for the generalized model they are not homogeneous. To estimate the effect of the far wake, stationary far wake solutions are calculated separately in section 2.3 to use them later for the calculation of the near wake. In this section the mathematical methodology employed to obtain all wake solutions is presented in detail. Then, in section 2.4, the framework to obtain near-wake solutions is presented. In section 2.5, we consider the classical Joukowski model, that is, when the hub vortex is located on the axis, obtaining stationary solutions for various wind turbine and helicopter regimes. Then, in section 2.6, generalized solutions are obtained when the hub vortex is not located on the axis. Finally, a comparison of the solutions obtained from the standard model and the generalized one is made.

2.2 Generalized Joukowski model

As it was introduced in section 1.2.3, in the Joukowski rotor model, the wake is generated by each blade as an ensemble of filaments of vorticity: a bound vortex on the blade,

and two free vortices of opposite circulation detached from the axis and the tip of the blade. For a N blade rotor, these vortices form in the far-wake a uniform helical braid composed of N vortices of circulation Γ plus a central vortex of circulation $-N\Gamma$ (figure 1.7b). However, in many actual rotors, it can be observed that the internal vortex is not necessarily placed on the axis, but displaced on the radial direction, generating another helical vortex. In figure 2.1, experimental and numerical examples are shown where this configuration appears. In this section, a generalized Joukowski model taking into account this characteristic of the wake is presented. From each blade, the wake is composed of a bound vortex on the blade, and two free helical vortices, one detached from the tip with a circulation Γ and one detached near the axis with a circulation $-\Gamma$ (figure 2.1c). These two helices will not necessarily have the same pitch.

In the standard Joukowski model, the far-wake is spatially homogeneous. It is known that helical vortices with a uniform external axial flow keep undeformed under their own induction (Kida, 1981). With a straight hub vortex on the rotation axis, the angular rotation of the helix is modified but not its shape. However, if the hub vortex is not on the axis but has the form of a helix, the mutual induction between tip and hub vortices will not be homogeneous any more: a radial induced velocity will appear on the helices and they will be deformed. In addition, because of this mutual induction, the axial and azimuthal flow on each vortex will not be the same and the helices will normally have different pitches.

Finding the far-wake solution when the hub vortex is not on the axis is therefore already an issue –this problem is treated in the next section–. These far-wake solutions will be obtained calculating the structures resulting of the interaction of infinite helical vortex pairs. The details of the calculation of the near wake and its coupling with far-wake solution will be presented in section 2.4.

2.3 Far-wake solutions

The content of this section is extracted from the paper *Generalized helical vortex pairs* (Durán Venegas & Le Dizès, 2019), published in the *Journal of Fluid Mechanics*.

In section 2.3.1, we introduce the vortex method framework and review some preliminary results on helical vortices in order to introduce the geometric parameters characterizing our solutions. In section 2.3.2, we first derive an approximation for the solutions by neglecting helix deformations. Then, we characterize the deformation of the helices and the properties of the solutions in terms of structure velocities and induced velocities. The effect of varying the vortex core size is analyzed in section 2.3.3. A preliminary analysis of the solutions for the description of helicopter and wind turbine wakes is addressed in section 2.3.4.

2.3.1 Vortex filament framework

In this section, we describe the numerical method that we use. The method is based on a Lagrangian description of the vortices and a discretization of the vortices into segments. This discretization process allows us to use explicit expressions for the induced and self-induced velocities. After having explained these two aspects, we apply the method to

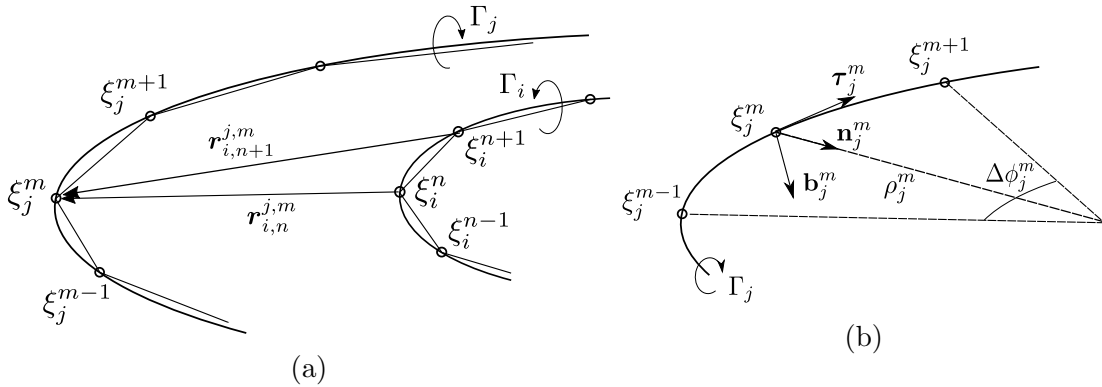


Figure 2.2: Discretization procedure of the vortex filaments. (a) Discretization in segments of two filaments of circulation Γ_i and Γ_j . (b) Arc of circle formed by three consecutive points of a discretized filament for the computation of the local contribution.

special cases: first to single helices to validate the method, then to non-interacting helical pairs to introduce the geometrical parameters that are used to define the solutions.

Lagrangian description

We consider small core size vortices which can be described as vortex filaments. In this framework, all the vorticity is concentrated along lines which move as material lines in the fluid according to

$$\frac{d\boldsymbol{\xi}}{dt} = \mathbf{U}(\boldsymbol{\xi}) = \mathbf{U}^\infty + \mathbf{U}^{ind}(\boldsymbol{\xi}), \quad (2.1)$$

where $\boldsymbol{\xi}$ is the position vector of the vortex filament, \mathbf{U} the velocity field, composed of an external field \mathbf{U}^∞ and a field $\mathbf{U}^{ind}(\boldsymbol{\xi})$ induced by the vortex filaments. When there are N vortices, this induced velocity is given by the Biot-Savart law

$$\mathbf{U}^{ind}(\boldsymbol{\xi}) = \sum_{j=1}^N \frac{\Gamma_j}{4\pi} \int \frac{(\boldsymbol{\xi}_j - \boldsymbol{\xi}) \times d\boldsymbol{\tau}_j}{|\boldsymbol{\xi}_j - \boldsymbol{\xi}|^2}, \quad (2.2)$$

where the integrals cover each vortex filament defined by its circulation Γ_j , its position vector $\boldsymbol{\xi}_j$ and its tangent vector $\boldsymbol{\tau}_j$.

On the vortex line, the Biot-Savart integral is singular, and the self-induced velocity diverges. To avoid this singularity, one has to assume a small but finite core size a . The self-induced motion is then obtained by an integral of the same form but without considering the interval $[-\delta a, \delta a]$ around the singular point. This so-called cut-off method is explained in length in textbooks (see Saffman, 1992). The value of δ depends on the vortex core model. Here, we shall assume a Gaussian vorticity profile for which $\delta \approx 0.8736$.

Vortex discretization

We follow the vortex method approach described for instance in Leishman (2006). Each vortex filament is discretized in small segments in order to compute the velocity field and follow its displacement (see figure 2.2a).

The velocity field induced by a given segment $[\boldsymbol{\xi}_i^n, \boldsymbol{\xi}_i^{n+1}]$ of the i th vortex at a point $\boldsymbol{\xi}_j^m$ can be calculated explicitly as

$$\mathbf{U}_{i,n}^{seg}(\boldsymbol{\xi}_j^m) = \frac{\Gamma_i}{4\pi} \frac{((1 - |\mathbf{r}_{i,n}^{j,m}|^2)|\mathbf{r}_{i,n}^{j,m}| + (1 - |\mathbf{r}_{i,n+1}^{j,m}|^2)|\mathbf{r}_{i,n+1}^{j,m}|)(\mathbf{r}_{i,n}^{j,m} \times \mathbf{r}_{i,n+1}^{j,m}) \cdot \mathbf{r}_{i,n}^{j,m} \cdot \mathbf{r}_{i,n+1}^{j,m}}{((\mathbf{r}_{i,n}^{j,m} \cdot \mathbf{r}_{i,n+1}^{j,m})^2 - |\mathbf{r}_{i,n}^{j,m}|^2 |\mathbf{r}_{i,n+1}^{j,m}|^2) |\mathbf{r}_{i,n}^{j,m}| |\mathbf{r}_{i,n+1}^{j,m}|}, \quad (2.3)$$

where $\mathbf{r}_{i,n}^{j,m} = \boldsymbol{\xi}_j^m - \boldsymbol{\xi}_i^n$. This expression is defined everywhere except at the points $\boldsymbol{\xi}_i^n$ and $\boldsymbol{\xi}_i^{n+1}$ defining the segment. To determine the contribution to the velocity field at $\boldsymbol{\xi}_j^m$ of the adjacent segments $[\boldsymbol{\xi}_j^m, \boldsymbol{\xi}_j^{m+1}]$ and $[\boldsymbol{\xi}_j^{m-1}, \boldsymbol{\xi}_j^m]$, we replace the two segments by the arc of circle passing through the three points $(\boldsymbol{\xi}_j^{m-1}, \boldsymbol{\xi}_j^m, \boldsymbol{\xi}_j^{m+1})$ and use the cut-off formula. We obtain

$$\mathbf{U}_{j,m}^{loc} = \frac{\Gamma_j}{4\pi\rho_j^m} \ln\left(\frac{\Delta\phi_j^m \rho_j^m}{\delta a}\right) \mathbf{b}_j^m, \quad (2.4)$$

where ρ_j^m and \mathbf{b}_j^m are the curvature radius and binormal vector at $\boldsymbol{\xi}_j^m$ respectively, and $\Delta\phi_j^m$ is the angle of the arc of circle $(\boldsymbol{\xi}_j^{m-1}, \boldsymbol{\xi}_j^{m+1})$ as illustrated in figure 2.2b. The total induced velocity at $\boldsymbol{\xi}_j^m$ is then given by an expression of the form

$$\mathbf{U}^{ind}(\boldsymbol{\xi}_j^m) = \mathbf{U}_{j,m}^{loc} + \sum_{n=1}^N \sum_{i=1}^{p_n} \mathbf{U}_{i,n}^{seg}(\boldsymbol{\xi}_j^m), \quad (2.5)$$

where p_n is the number of points discretizing the n th vortex, and assuming implicitly that $\mathbf{U}_{j,m}^{seg}(\boldsymbol{\xi}_j^m) = \mathbf{U}_{j,m-1}^{seg}(\boldsymbol{\xi}_j^m) = 0$.

This formula is tested against direct calculation of the cut-off integral in figure 2.3 for a single helix (see also Gupta & Leishman, 2005a). We observe that a good approximation is obtained as soon as the helix is divided in 25 or more segments by turn when the local contribution is included. When the local contribution is not taken into account, a much larger number of segments by turn of order $O(2\pi\rho/a)$ is needed to obtain a good approximation. In practice, we use $p_n = 30$ in most calculations.

Vortex ring and helical vortex

A vortex ring and a helical vortex are examples of vortex structures that move in space at a constant speed without deformation. For these particular vortices, there exist a unique moving frame where all the vortex elements are steady. For the ring, this frame is translating along the ring axis. For the helix, it is both translating and rotating along the helix axis.

The variation of the rotation rate and axial speed of a right-handed helix with respect to the pitch is given in figure 2.4 for a typical vortex core size. As already noticed by Velasco Fuentes (2018), it is interesting to see that the rotation changes sign as the pitch varies. For a left-handed helix, the rotation rate is the same but the axial speed is opposite. In figure 2.4, our numerical results are compared to theoretical approximations based on Hardin (1984) expressions. The dashed grey curves are obtained by taking the mean value of Hardin expression at $R - a$ and $R + a$ as it was done by Velasco Fuentes (2018). The solid grey line is the same expression corrected by a $1/4$ term associated with

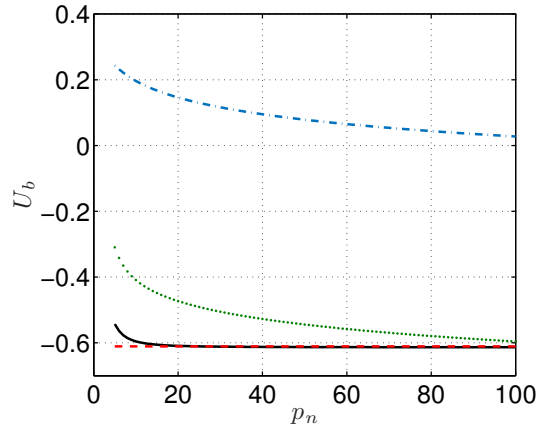


Figure 2.3: Comparison of the cut-off formula (dashed red line) with the approximate formula (2.5) (solid black line). Binormal component of the induced velocity versus the number p_n of segments by turn for an helix of circulation $\Gamma = 1$, pitch $h = 1$, radius $R = 1$, and core size $a = 0.05$. The two contributions \mathbf{U}^{loc} and \mathbf{U}^{seg} are also indicated in dash-dot and dotted lines, respectively.

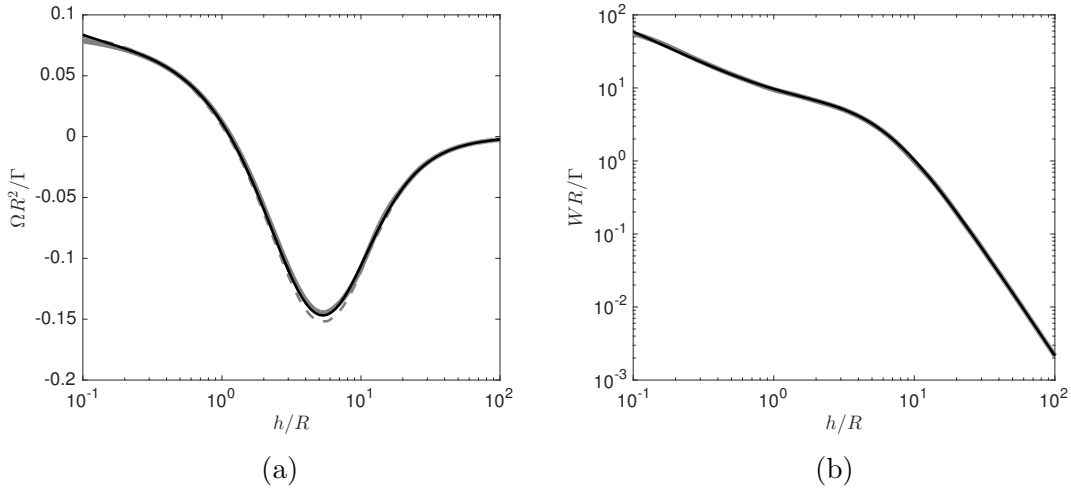


Figure 2.4: Non-dimensionalized rotation rate $\Omega R^2/\Gamma$ (a) and axial speed WR/Γ (b) of a right-handed helix of circulation Γ , radius R , pitch h and core size a as a function of h/R for $a/R = 0.03$. The solid black curves correspond to the numerical results obtained in this work. The solid grey curves correspond to the theoretical expressions (2.6-2.7), the dashed grey curves correspond to the results obtained by Velasco Fuentes (2018), that is the same expressions without the $1/4$ terms. Both theoretical results are for an equivalent Rankine vortex of core size $a/R = 0.0408$.

local curvature (Ricca, 1994; Kuibin & Okulov, 1998; Boersma & Wood, 1999):

$$\frac{\Omega R^2}{\Gamma} = \frac{\ln(2/\epsilon) + 2(1+p^2) - \ln(\sqrt{1+p^2}) - (1+p^2)^{3/2}[2/p - \mathcal{W}(p)] - 1/4}{4\pi(1+p^2)^{3/2}}, \quad (2.6)$$

$$\frac{WR}{\Gamma} = \frac{\ln(2/\epsilon) - \ln(\sqrt{1+p^2}) + (1+p^2)^{3/2}\mathcal{W}(p) - 1/4}{4\pi(1+p^2)^{3/2}}, \quad (2.7)$$

where $p = h/(2\pi R)$, $\epsilon = a/[R(1+p^2)]$ and $\mathcal{W}(p)$ is the function defined in Boersma & Wood (1999) by

$$\mathcal{W}(p) = \int_0^\infty \left\{ \frac{\sin^2 t}{(p^2 t^2 + \sin^2 t)^{3/2}} - \frac{1}{(p^2 + 1)^{3/2}} \frac{H(1/2 - t)}{t} \right\} dt. \quad (2.8)$$

This correction term permits to take into account the deformation of the vortex core induced by curvature. In these theoretical works, a Rankine vortex model (uniform vorticity in the core) is used, while we use a Gaussian vorticity profile. We have thus applied the correction factor $a_{\text{Rankine}} \approx 1.36 a_{\text{Gaussian}}$ to the core size to account for the different vortex models (Widnall, 1972; Saffman, 1992). As it can be seen on this figure, the agreement between the numerical results and Velasco Fuentes (2018) is good and almost perfect for both Ω and W when the correction term is included. This comparison is a strong validation of our numerical approach.

For both rings and helices, there exist infinitely many other moving frames where the vortex structure is steady. The displacement associated with this frame just has to remain tangent to the structure. The condition of steadiness for the frame velocity \mathbf{V}_F can then be written as

$$(\mathbf{V}_F(\boldsymbol{\xi}_j^m) + \mathbf{U}^{ind}(\boldsymbol{\xi}_j^m)) \times \boldsymbol{\tau}_j^m = \mathbf{0}. \quad (2.9)$$

In this frame, the vortex elements are moving along the vortex structure. For a ring, any rotation around the ring axis can for instance be added. For an helix of pitch h , any rotation and translation along the helix axis can also be added if the rotation rate Ω_a and axial speed W_a of this additional movement satisfy

$$W_a/\Omega_a = \pm h/2\pi, \quad (2.10)$$

where the sign is $+$ for right-handed helices, and $-$ for left-handed helices.

An helical braid composed of N identical vortices of same axis, separated with each other by an azimuthal angle $2\pi/N$ also forms a steady solution in an adequate frame. When $N \neq 1$, a straight hub vortex placed on the central axis can be added without introducing any deformation on the helices. This is not possible when $N = 1$. The external helix indeed generates an horizontal velocity on the axis that induces a radial displacement of any straight structure place at this position. In that case, we expect the hub vortex to deform and to move out from the rotation axis. Our objective is to describe such a structure, as well as the structures composed of N vortex pairs with root vortices not on the rotation axis. We shall see that there still exist steady solutions in those cases.

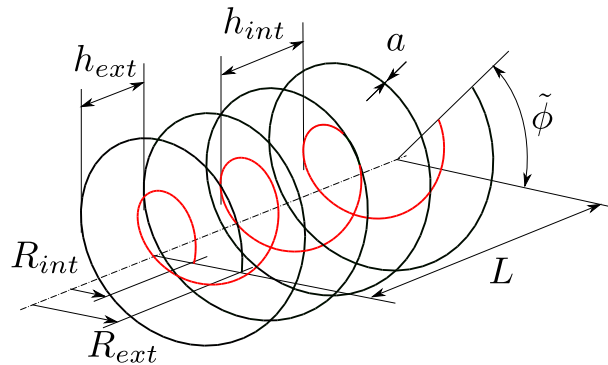


Figure 2.5: Configuration of two undeformed co-axial helical vortices. Here both helices have the same orientation: $\kappa = 1$.

Non-interacting helical pairs

In order to understand the parameters defining the solutions, it is useful to consider first a simple configuration composed of two co-axial helices of opposite circulation and same core size a . The internal and external helices are defined by their radii R_{int} and R_{ext} and pitches h_{int} and h_{ext} , as illustrated in figure 2.5. They also depend on their relative orientation characterized by a parameter κ , which is $+1$ if both helices have the same orientation, and -1 if they have opposite orientations.

If $\kappa = -1$ or if $h_{ext} \neq h_{int}$, this pair of vortices is no longer helically invariant. However, it exhibits a certain spatial periodicity. The periodicity is in the sense that there exists an axial distance $L > 0$ and an angle $0 \leq \tilde{\phi} < 2\pi$ such that the radial locations of each vortex are invariant by the double operation of translation by L and rotation by $\tilde{\phi}$ (see figure 2.5). The parameters L and $\tilde{\phi}$ are given by

$$\frac{1}{L} = \left| \frac{1}{h_{int}} - \frac{\kappa}{h_{ext}} \right|, \quad (2.11a)$$

$$\tilde{\phi} = 2\pi \left[\frac{L}{\min(h_{int}, h_{ext})} - E \left(\frac{L}{\min(h_{int}, h_{ext})} \right) \right], \quad (2.11b)$$

where $E(x)$ denotes the integer part of x . When $\kappa = -1$, L is smaller than h_{ext} and h_{int} : both helices have performed less than a complete rotation in one axial period L . When $\kappa = 1$, L is always larger than the smaller pitch; the helix with the smaller pitch has then performed more than a complete rotation in a period. The other helix has performed just one complete revolution less.

When $h_{ext} \neq h_{int}$, the undeformed helical pair corresponds to a steady solution only if the mutual induction of one helix on the other is negligible. This occurs when the core size becomes sufficiently small. In this limit, the locally induced velocity is the dominant contribution to the induced velocity which then becomes constant and oriented along the local binormal vector. Each helix then behaves as if the other helix was not present. *A priori*, they rotate and translate at different speeds. But, owing to the possibility to add any displacement along the helical line, it is possible to find a frame where both helical structures become steady. The frame selection is graphically explained in figure 2.6b. In that figure, we plot each helix in the (ϕ, z) plane at $t = 0$ (solid lines) and $t = 1$

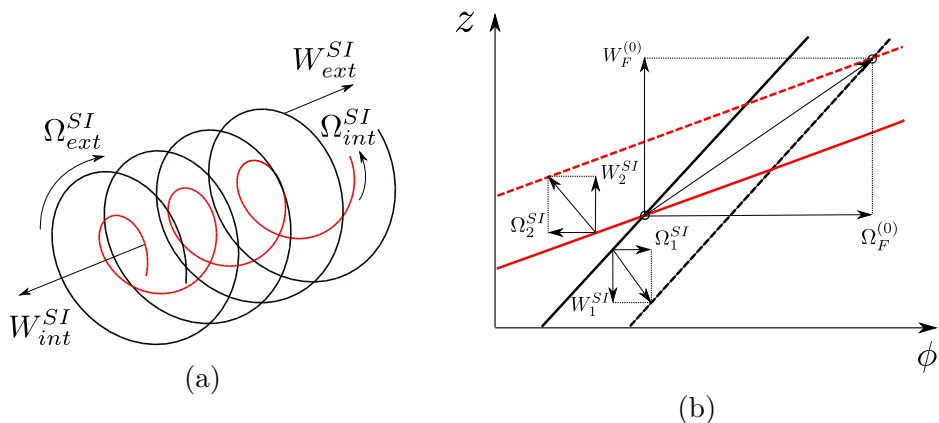


Figure 2.6: (a) Self-induced velocities of a pair of coaxial vortices when the mutual induction is negligible. (b) Schematic diagram showing how the moving frame velocities $\Omega_F^{(0)}$ and $W_F^{(0)}$ are obtained. Solid and dashed lines represent the two helices at $t = 0$ and $t = 1$ respectively. The frame velocity is given by the vector connecting the crossing points of solid lines with dashed lines. The axial and azimuthal components of this vector provides $W_F^{(0)}$ and $\Omega_F^{(0)}$ respectively.

(dashed lines) using two different colors. Each helix corresponds to a straight line with a slope equal to the helix pitch. The self-induced velocity of each helix, together with their decomposition on the axial and azimuthal direction is also indicated. Any vector that connects any two points from the lines at the two distinct times provides a possible frame velocity vector that keeps the considered helix steady. The vector that keeps both helices steady is the one that connects the crossing points associated with each instant. Such a vector exists as soon as the helix lines are not parallel in the (ϕ, z) plane, that is if $h_{ext} \neq h_{int}$ or $\kappa = -1$.

The angular velocity $\Omega_F^{(0)}$ and axial velocity $W_F^{(0)}$ of the frame are given from the self-induced velocity of each helix by

$$\Omega_F^{(0)} = \frac{2\pi(W_{int}^{SI} - W_{ext}^{SI}) + (\Omega_{ext}^{SI}h_{ext} - \Omega_{int}^{SI}\kappa h_{int})}{h_{ext} - \kappa h_{int}}, \quad (2.12a)$$

$$W_F^{(0)} = W_{ext}^{SI} + \frac{h_{ext}}{2\pi}(\Omega_F^{(0)} - \Omega_{ext}^{SI}). \quad (2.12b)$$

The second equation shows that condition (2.10) is satisfied by the external vortex. It is immediate to obtain

$$W_F^{(0)} = W_{int}^{SI} + \frac{\kappa h_{int}}{2\pi}(\Omega_F^{(0)} - \Omega_{int}^{SI}), \quad (2.13)$$

that guarantees that (2.10) is also satisfied by the internal vortex.

Without restriction, we can assume the external helix to be right-handed with a positive circulation Γ . The internal helix has then a negative circulation $-\Gamma$. It is right-handed if $\kappa = 1$, left-handed if $\kappa = -1$.

Parameters defining the deformed helical structures

The two-helix structure obtained above is no longer a solution if the two helices interact. Indeed, the velocity field of one helix on the other contains a radial component that moves the structure radially. Each helix is therefore expected to be deformed by the field induced by the other helices. Being inspired by the non-interacting solutions, we shall search for steady solutions that still exhibit a spatial periodicity. We consider solutions composed of N pairs of counter-rotating vortices (the external vortex having a positive circulation Γ , the internal a negative circulation $-\Gamma$), with a $2\pi/N$ azimuthal symmetry. By construction, we then assume that the solutions are invariant by the transform $\phi \rightarrow \phi + 2\pi/N$. We also assume that there exist an axial distance $L > 0$ and an angle $\tilde{\phi}$ satisfying $0 \leq \tilde{\phi} < 2\pi/N$, such that the solutions are invariant by the double operation $z \rightarrow z + L$ and $\phi \rightarrow \phi + \tilde{\phi}$. We do not want the solution to repeat several times in a spatial period, so we further assume that there is a single location in an axial period L where internal and external vortices are at the same azimuth. We shall choose this particular azimuth to define from their radial positions the radius R_{int} and R_{ext} of the internal and external vortex ($R_{int} < R_{ext}$). We also define the mean pitch h_{int} and h_{ext} for each vortex from the azimuthal angle covered in an axial period. For the external vortex, if this angle is ϕ_{ext} , we have $h_{ext} = \frac{2\pi L}{\phi_{ext}}$. If we add the vortex core size a that we assume identical and constant for all the vortices, we obtain 5 spatial length scales from which we can form 4 independent non-dimensional parameters:

$$R^* = \frac{R_{int}}{R_{ext}}, \quad h^* = \frac{h_{ext}}{R_{ext}}, \quad \alpha = \frac{h_{int}}{h_{ext}}, \quad \varepsilon = \frac{a}{R_{ext}}. \quad (2.14)$$

To these 4 real positive parameters, we should add the number N of vortex pairs and the index $\kappa = \pm 1$ that defines the relative orientation of internal and external vortices. In most cases, we shall keep $\kappa = 1$ and $N = 1$. The parameter R^* will be varied between 0 and 0.75, h^* between 0.1 and 2, α between 0.5 and 2. The parameter ε will always be considered small, and typically equal to 0.03. Even for this small value of ε , finite core size effects can become important if h and α are too small. This provides a limitation on the values of the parameters that we can consider. Here, only the extreme cases ($h \approx 0.1$ and $\alpha \approx 0.5$) are expected to give rise to consequent finite core size effects.

In the paper, the vortex core size is also assumed to be constant. This approximation is discussed in section 2.3.3.

Note that both the normalized period L/R_{ext} and the angle $\tilde{\phi}$ can be obtained from the above geometrical parameters:

$$\frac{L}{R_{ext}} = \frac{h^*}{N|1/\alpha - \kappa|}, \quad \tilde{\phi} = \frac{2\pi}{N} \left[\frac{1}{|1/\alpha - \kappa|} - E \left(\frac{1}{|1/\alpha - \kappa|} \right) \right]. \quad (2.15)$$

With each solution is associated a moving frame where the solution is steady. From the angular velocity Ω_F and the axial velocity W_F of the frame, we can construct two other dimensionless parameters using the external radius R_{ext} and the circulation Γ of the vortices:

$$\Omega = \frac{R_{ext}^2 \Omega_F}{N\Gamma}, \quad W = \frac{R_{ext} W_F}{N\Gamma}. \quad (2.16)$$

These two parameters characterizing the frame velocity are functions of the 6 geometrical parameters R^* , h^* , α , ε , N and κ .

2.3.2 Deformed helical vortex pairs

In this section, we describe the deformed helical structures as the geometrical parameters vary. After having introduced an approximated solution, we successively study the geometrical characteristics, the frame velocity and the induced velocity.

First order approximation

As already mentioned above, as soon as the mutual induction of one helix on the others is taken into account, the vortex structure does not remain helical. For a given vortex parametrized by its radial position $r(z)$ and angular position $\phi(z)$ as a function of the z coordinate, the condition of steadiness (2.9) reduces to

$$\frac{dr}{dz} = \frac{V_r^{ind}}{V_z^{ind} - W_F}, \quad \frac{d\phi}{dz} = \frac{\Omega_z^{ind} - \Omega_F}{V_z^{ind} - W_F}. \quad (2.17)$$

Each induced velocity component is composed of two contributions, a self-induced contribution V^{SI} and a contribution induced by the other vortices V^{MI} . The radial self-induced velocity of an helix being null, we clearly see from the first equation that the radial deformation will be associated with the mutual induction, and more precisely with the radial component V_r^{MI} of the mutually induced velocity.

A first order correction to the undeformed solution can be obtained by solving these two equations assuming that the velocity fields on the right-hand side are evaluated at the undeformed location:

$$\frac{dr^{(1)}}{dz} = \frac{V_r^{MI}(r_0, \phi_0(z), z)}{V_z^{MI}(r_0, \phi_0(z), z) + V_z^{SI} - W_F^{(1)}}, \quad (2.18a)$$

$$\frac{d\phi^{(1)}}{dz} = \frac{\Omega^{MI}(r_0, \phi_0(z), z) + \Omega^{SI} - \Omega_F^{(1)}}{V_z^{MI}(r_0, \phi_0(z), z) + V_z^{SI} - W_F^{(1)}}. \quad (2.18b)$$

For the mutual induction, we use the formula given by Hardin (1982) for a perfect helix. The corrected frame velocities $\Omega_F^{(1)}$ and $W_F^{(1)}$ are obtained by using the definition of L for the internal and external vortex:

$$\phi_{int}^{(1)}(L) - \phi_{int}^{(1)}(0) = \frac{2\pi L}{h_{int}} = \int_0^L \frac{\Omega_{int}^{MI}(r_{int}^{(0)}, \phi_{int}^{(0)}(z), z) + \Omega_{int}^{SI} - \Omega_F^{(1)}}{V_{z,int}^{MI}(r_{int}^{(0)}, \phi_{int}^{(0)}(z), z) + V_{z,int}^{SI} - W_F^{(1)}} dz, \quad (2.19a)$$

$$\phi_{ext}^{(1)}(L) - \phi_{ext}^{(1)}(0) = \frac{2\pi L}{h_{ext}} = \int_0^L \frac{\Omega_{ext}^{MI}(r_{ext}^{(0)}, \phi_{ext}^{(0)}(z), z) + \Omega_{ext}^{SI} - \Omega_F^{(1)}}{V_{z,ext}^{MI}(r_{ext}^{(0)}, \phi_{ext}^{(0)}(z), z) + V_{z,ext}^{SI} - W_F^{(1)}} dz. \quad (2.19b)$$

Note that equations (2.19a,b) give (2.12) if we neglect the mutual induction. The condition of periodicity of the radial deformation does not give an additional constraint because it is automatically satisfied for each vortex.

This simple first order approximation for the helix deformation is compared to numerical results for two typical examples in figure 2.7. We clearly see that the agreement strongly depends on the pitch ratio α . This approximation tends to underestimate the deformation of the external vortex but to overestimate that of the internal vortex. The

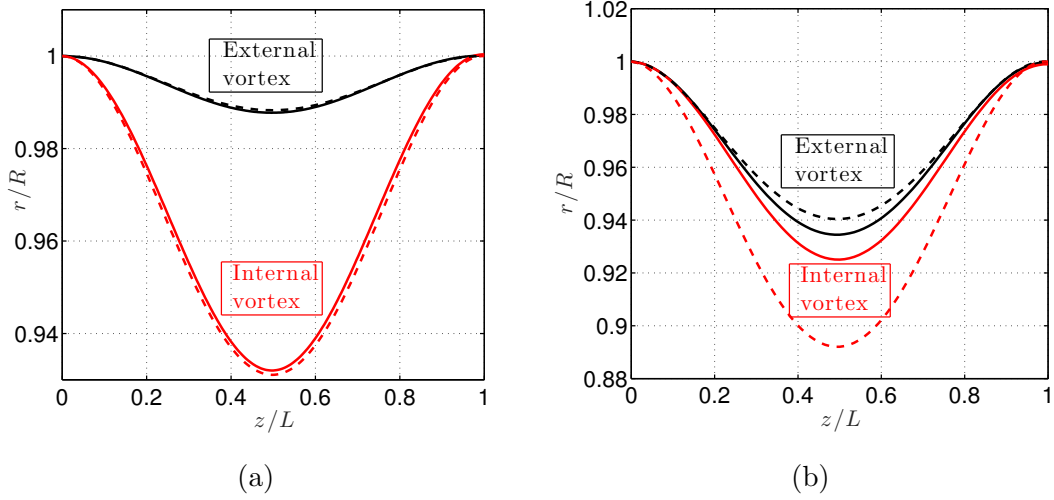


Figure 2.7: Radial position of the internal and external vortices for a single counter-rotating helical pair for (a) $R^* = 0.5$, $\kappa = 1$, $h^* = 1$, $\alpha = 0.9$ and $\varepsilon = 0.03$ (b) $R^* = 0.5$, $\kappa = 1$, $h^* = 1$, $\alpha = 1.4$ and $\varepsilon = 0.03$. Solid line: numerical solution. Dashed line: first order approximation.

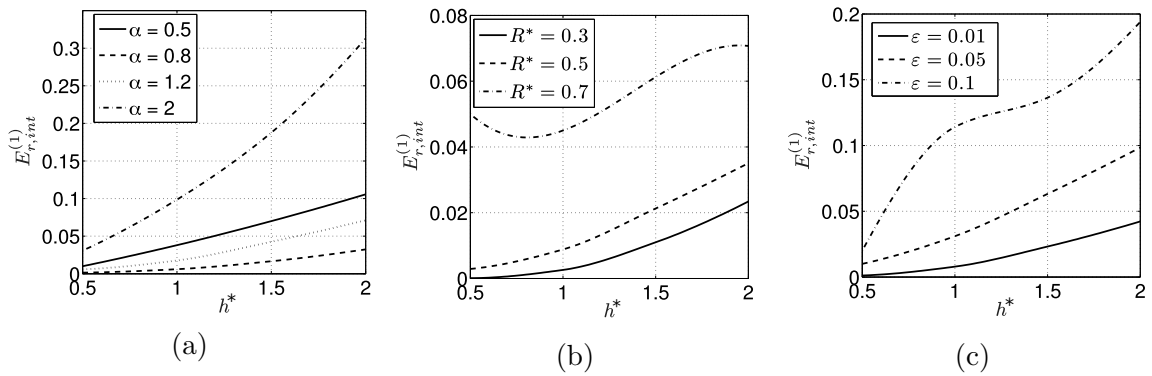


Figure 2.8: First order approximation error $E_{r,int}^{(1)}$ for a single vortex pair ($N = \kappa = 1$). (a): $R^* = 0.5$ and $\varepsilon = 0.03$; (b): $\alpha = 1.2$ and $\varepsilon = 0.03$; (c): $R^* = 0.5$ and $\alpha = 1.2$

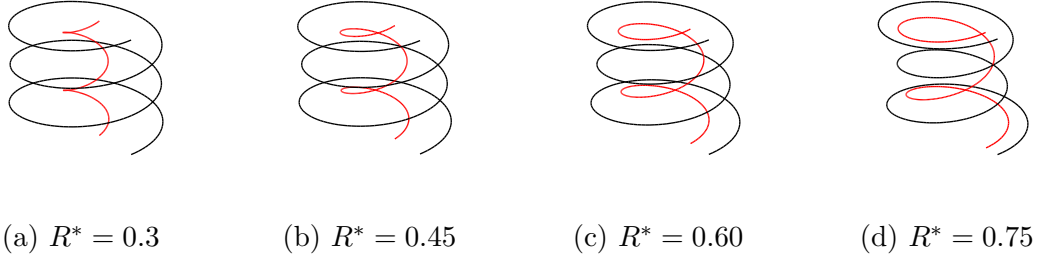


Figure 2.9: Representation of the deformed vortex structure for $N = 1$, $\kappa = 1$, $h^* = 2$, $\alpha = 1.5$, $\varepsilon = 0.06$ and different values of R^*

error is always larger for the internal vortex. The maximum error can then be quantified using

$$E_{r,int}^{(1)} = \frac{\max(|r_{int} - r_{int}^{(1)}|)}{R_{int}} \quad (2.20)$$

which measures the maximum deviation between numerical and first order solutions. This quantity is plotted in figure 2.8 as a function of h^* for $N = \kappa = 1$ and various α , R^* and ε . This figure shows that except for very large R^* ($R^* = 0.7$), the error increases with h^* . The error also increases with ε , R^* and with the distance of α to 1. It becomes particularly large (superior to 30%) for large α and large h^* . Note however that the error remains small for $\alpha \approx 1$, small R^* and small ε .

Characterization of the helix deformation

The first order approximation clearly demonstrates that the radial deformation increases when the radial velocity induced by the other vortices grows. This occurs when internal and external vortices get closer to each other, that is when R^* increases. This is illustrated on figure 2.9 where a perspective view of a single pair is shown for different values of R^* , the other parameters being fixed.

In order to quantify the level of deformation, we introduce two quantities

$$\Delta r_{max}^{int} = \frac{\max(|r_{int} - R_{int}|)}{R_{int}}, \quad \Delta r_{max}^{ext} = \frac{\max(|r_{ext} - R_{ext}|)}{R_{ext}} \quad (2.21)$$

that measure the maximum displacement of internal and external vortices. The growth of Δr_{max}^{int} and Δr_{max}^{ext} with respect to R^* is quantified in figure 2.10c. The effect of the number of vortices is clearly visible. The vortex deformation strongly decreases with N . For $R^* = 0.7$, the fluctuation of the internal vortex reaches 30% for a single vortex pair while it is less than 0.1% for three vortex pairs. Note that when R^* goes to zero, the deformation of the external vortex vanishes whatever N . When $N \neq 1$, this is the same for the internal vortex. In that case, we recover the Joukowski's model with a straight vortex hub on the helix axis. For $N = 1$, the limit $R^* \rightarrow 0$ is by contrast singular.

The variations of Δr_{max}^{int} and Δr_{max}^{ext} with respect to h^* and α are shown in figure 2.11. The increase of the vortex deformations with h^* is associated with the decrease of the axial component of the induced velocity. Indeed, for large h^* , the vortices get aligned

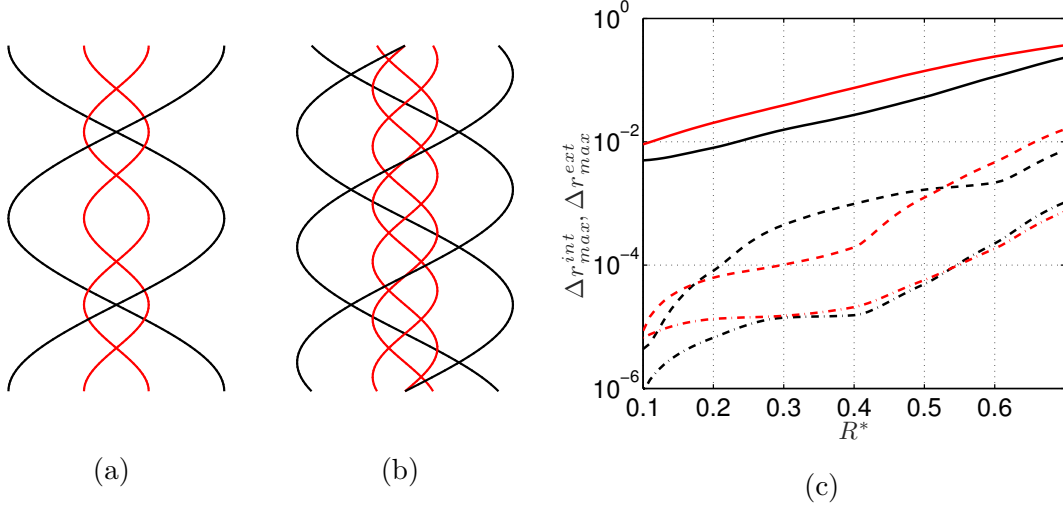


Figure 2.10: Representation of 2 vortex pairs (a) and 3 vortex pairs (b) for $h^* = 1$, $R^* = 0.4$, $\varepsilon = 0.05$, $\alpha = 2$, $\kappa = 1$. (c): Maximum deformation Δr_{max}^{int} (red) and Δr_{max}^{ext} (black) versus R^* for 1 vortex pair (solid lines), 2 vortex pairs (dashed lines), 3 vortex pairs (dash-dot lines). $h^* = 1$, $\alpha = 1.5$, $\kappa = 1$ and $\varepsilon = 0.05$.

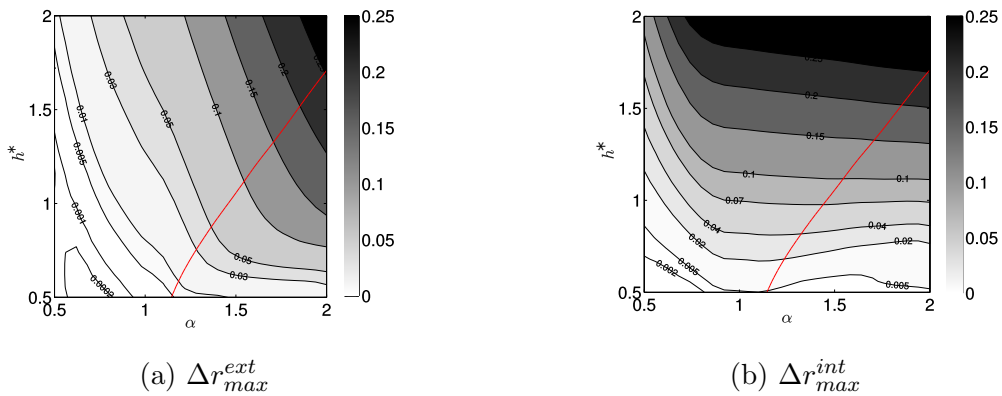


Figure 2.11: Maximum deformation contours in the (α, h^*) plane for $R^* = 0.5$, $\varepsilon = 0.03$, $\kappa = 1$, $N = 1$. The thick solid line corresponds to the line $\Delta r_{max}^{int} = \Delta r_{max}^{ext}$.

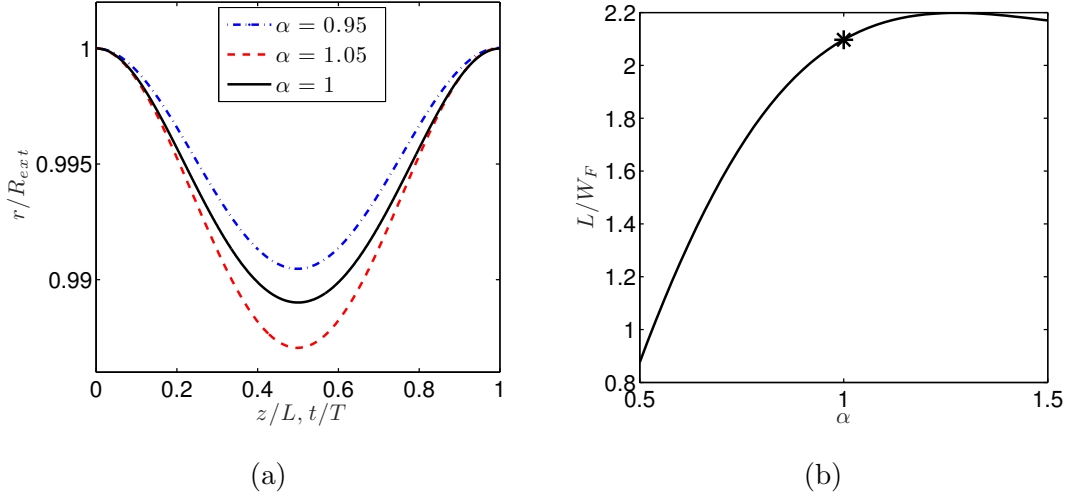


Figure 2.12: Characteristics close to $\alpha = 1$ for $h^* = 1$, $\varepsilon = 0.01$, $N = 1$, $\kappa = 1$. (a) Comparison of the radial positions of deformed helices versus z/L for $\alpha = 1.05$ and $\alpha = 0.95$ with the radial position of perfect helices versus t/T for $\alpha = 1$. (b) Variation of the characteristic time scale L/W_F versus α . The symbol represents the period T of the temporal evolution of perfect helices for $\alpha = 1$.

with the respect to z axis. They therefore mainly induce a velocity field in the radial and azimuthal directions. The ratio V_r/V_z that defines the slope of the deformation thus gets large, implying large Δr_{max}^{int} and Δr_{max}^{ext} . In the opposite, when h^* goes to zero, V_r/V_z goes to zero as well: the helical vortices are thus no longer deformed.

Concerning the effect of α , the increase of the deformation of the external helix with α can be understood by the same argument. It is associated with a decrease of h_{int} , and therefore an increase of the ratio V_r/V_z . The variation of Δr_{max}^{int} with respect to α is less simple. For $h^* < 1$, Δr_{max}^{int} is maximum for α close to 1. This value $\alpha = 1$ is special for $\kappa = 1$ because the axial period L and the frame axial velocity W_F get infinite [see equation (2.15)]. It therefore corresponds to a singular limit in our description. However, the radial positions r_{int} and r_{ext} of internal and external vortices can still be plotted as a function of z/L and we obtain a well-defined curve as $\alpha \rightarrow 1$. Similarly, W_F/L converges to a non-zero constant as $\alpha \rightarrow 1$, which means that a finite time $T = L/W_F$ is needed to advect a perturbation on the period L at the velocity W_F . The singular case $\alpha = 1$ could therefore be described by an alternative way by considering the solution in the frame moving at the velocity W_F . In this frame it should correspond to the temporal dynamics of perfect helices with the same R^* , h^* and ε . This is indeed what we have checked in figure 2.12. In figure 2.12(a), we show that the variation of r_{int} as a function of z/L for α close to one, is well described by the variation of r_{int} as a function of t/T in the temporal problem. We also check in figure 2.12(b) that L/W_F converges to the temporal period obtained in the temporal problem as $\alpha \rightarrow 1$.

Structure velocities

As explained above (§2.3.2), we can obtain different approximations of the frame velocity Ω_F and W_F by neglecting the helix deformations and/or the mutual induction. The

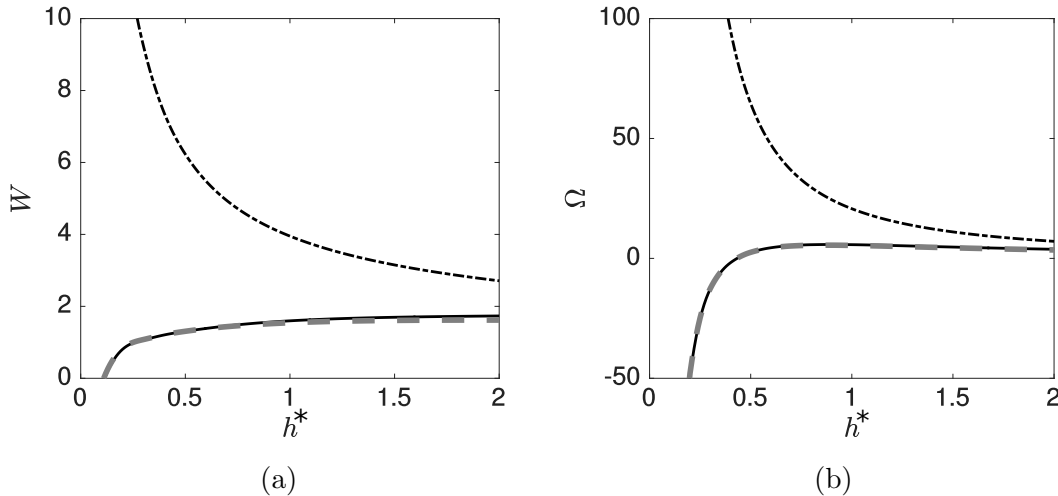


Figure 2.13: Frame velocity versus h^* for $R^* = 0.5$, $\varepsilon = 0.03$, $\alpha = 1.4$, $\kappa = 1$, $N = 1$. (a) Angular velocity $\Omega = R_{ext}^2 \Omega_F / \Gamma$, (b) axial velocity $W = R_{ext} W_F / \Gamma$. Solid line: numerical result. Dashed line: first order approximation $(\Omega_F^{(1)}, W_F^{(1)})$. Dash-dotted line: leading order approximation $(\Omega_F^{(0)}, W_F^{(0)})$.

leading order approximation $(\Omega_F^{(0)}, W_F^{(0)})$ neglects both the mutual induction and the deformation. The first order approximation $(\Omega_F^{(1)}, W_F^{(1)})$ neglects the vortex deformation but takes into account the mutual induction. This approximation is obtained by solving the equations (2.19a,b) for $\Omega_F^{(1)}$ and $W_F^{(1)}$. In figure 2.13, we have compared both approximations to numerical results for a typical case. We clearly see that the leading order approximation does not capture the variations of Ω_F and W_F with h^* , while the first order approximation follows both qualitatively and quantitatively these variations. By comparing other configurations, we have observed that the first order approximation provides a good approximation of Ω_F and W_F as soon as $R^* \leq 0.5$ and $\varepsilon \leq 0.1$. In practice, these approximations have been used as guess values for the numerical calculation.

The variations of the frame velocities Ω and W with respect to h^* and α are shown in figure 2.14. Both contour plots exhibit similar features: a same singularity line $\alpha = 1$ and a single contour where Ω and W vanish. These zero level contours are different for Ω and W but both cross the singular line $\alpha = 1$ at the same value (here $h^* \approx 0.175$). This special point on the singular line $\alpha = 1$ corresponds to the particular solution obtained by Walther *et al.* (2007). For these parameters, the vortices are undeformed helices of same pitch. There therefore exist infinitely many frames where the helices are stationary as any values of axial speed W_a and angular velocity Ω_a can be added provided (2.10) is satisfied. This explains the degeneracy observed at this point in figure 2.14. These qualitative features do not depend on ε and R^* . It is interesting to note that a contour of Ω may cross twice a contour of W (look at the saddle point region close to $(\alpha, h) \approx (1.7, 0.4)$). The coordinates of the two crossing points then correspond to couples of parameters (α, h) having the same frame velocities (Ω, W) .

By construction, the vortex elements are advected along the stationary vortex structure. This tangential velocity is different for the internal and the external vortex and varies

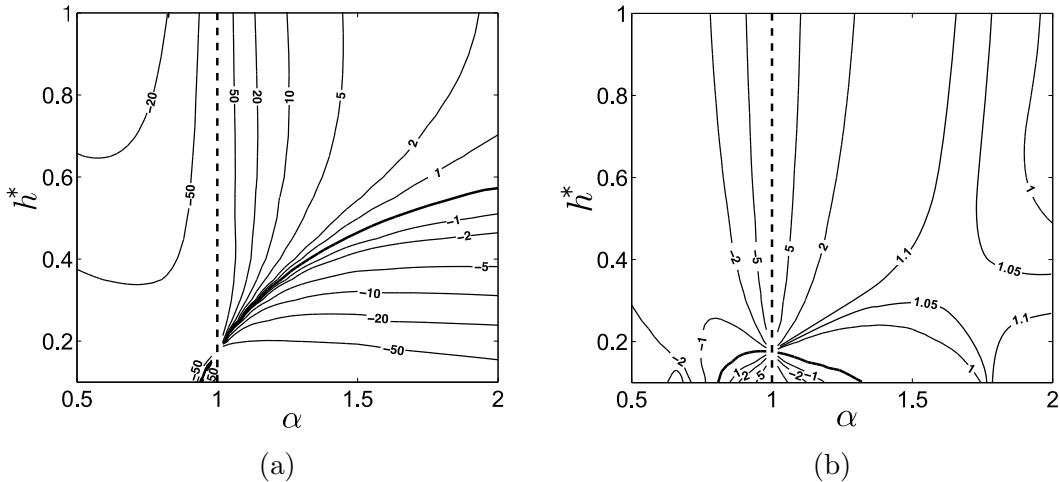


Figure 2.14: Contour values of the frame velocity in the (α, h) plane for $R^* = 0.5$, $\varepsilon = 0.03$, $N = 1$ and $\kappa = 1$. (a) Angular velocity $\Omega = \Omega_F R_{ext}^2 / \Gamma$, (b) Axial velocity $W = W_F R_{ext} / \Gamma$. The dashed line ($\alpha = 1$) indicates a line where Ω and W are not defined. The thick solid curve corresponds to the level zero.

along the vortex structure, as illustrated in figure 2.15a. This variation is associated with the deformation of the helices. It is then important when the level of deformation is high. For each vortex, we define a mean tangential velocity \bar{V}_{tan} and a measure ΔV_{tan} of the fluctuation around this mean using

$$\bar{V}_{tan} = \frac{1}{L} \int_{z_0}^{z_0+L} V_{tan}(z) dz, \quad \Delta V_{tan} = \frac{\max |V_{tan} - \bar{V}_{tan}|}{|\bar{V}_{tan}|}. \quad (2.22)$$

The measures ΔV_{tan}^{ext} and ΔV_{tan}^{int} for the external and internal vortex are plotted as a function of h^* in figure 2.15b for a few cases. We do observe an increase of the tangential velocity fluctuation with h^* and R^* , in agreement with the increase of the vortex deformation (see figure 2.11).

The mean tangential velocity of each vortex is shown in the (α, h) plane in figure 2.16. A positive value corresponds to an advection in the positive axial direction, a negative value to an advection in the opposite direction. Not surprisingly, the mean tangential velocity blows up as $\alpha \rightarrow 1$ like Ω_F and W_F . It is also interesting to note that the contour curves are similar (in shape) for both vortices and close to those obtained for $\Omega_F R_{ext}^2 / \Gamma$ in figure 2.14(a).

In figure 2.17a, we have displayed on the same plot the parameters for which mean tangential velocities and Ω_F vanish. We clearly see that mean tangential velocities and Ω_F vanish for almost the same parameters. This means that there is a very small region of parameters around the line $\Omega_F = 0$ where internal and external vortices propagate in different directions. This region is delimited by the solid lines shown in figure 2.17a. Everywhere else, both vortices propagate in the same direction. We shall see in section 2.3.4 that this condition on the direction of propagation of the vortices is necessary for the solution to describe the flow generated by a rotor.

It is interesting to compare more precisely the mean tangential velocity with the velocity associated with the moving frame. Assuming that each structure is approximatively

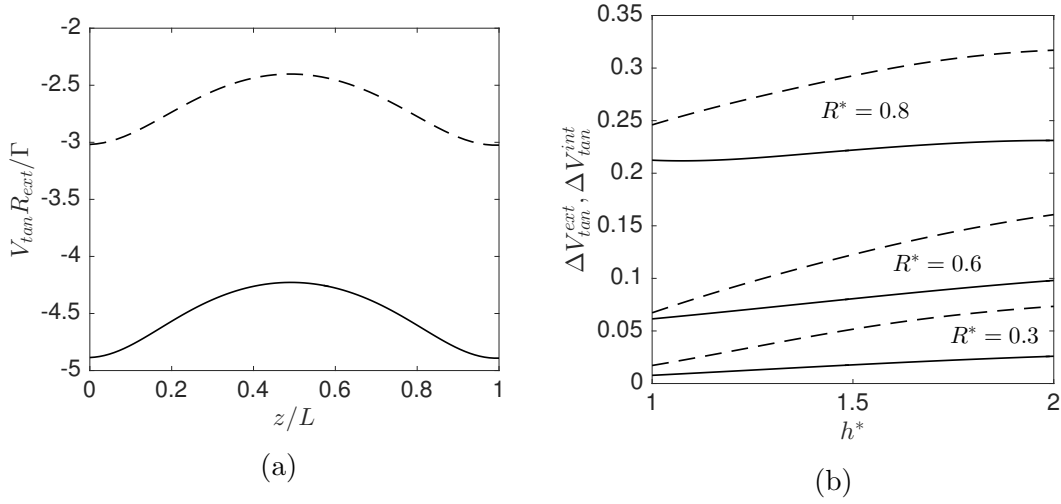


Figure 2.15: (a) Variation of the tangential velocity on a period in the internal vortex (dashed line) and in the external vortex (solid line) for a typical case ($R^* = 0.6$, $h^* = 1.5$, $\alpha = 1.4$ and $\varepsilon = 0.03$, $N = 1$, $\kappa = 1$). (b) Maximum tangential velocity fluctuation in the internal vortex (dashed lines) and external vortex (solid lines) as a function of h^* for different values of R^* and $\alpha = 1.4$, $\varepsilon = 0.03$, $N = 1$, $\kappa = 1$.

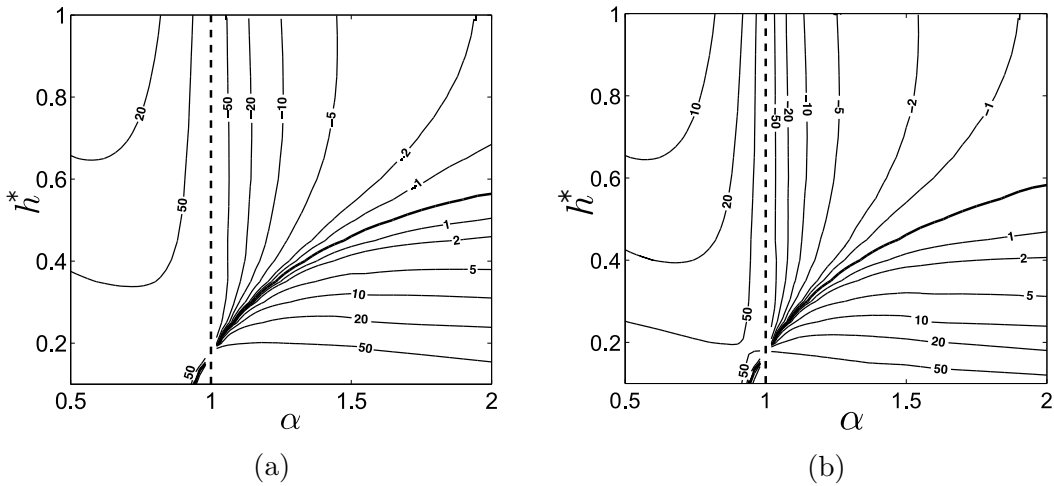


Figure 2.16: Contour values of the mean tangential velocities in the (α, h) plane for $R^* = 0.5$, $\varepsilon = 0.03$, $N = 1$, $\kappa = 1$. (a) External vortex: $\bar{V}_{tan}^{ext} R_{ext}/\Gamma$. (b) Internal vortex: $\bar{V}_{tan}^{int} R_{ext}/\Gamma$. The dashed line ($\alpha = 1$) indicates a line where \bar{V}_{tan}^{ext} and \bar{V}_{tan}^{int} are not defined. The thick solid curve corresponds to the level zero.

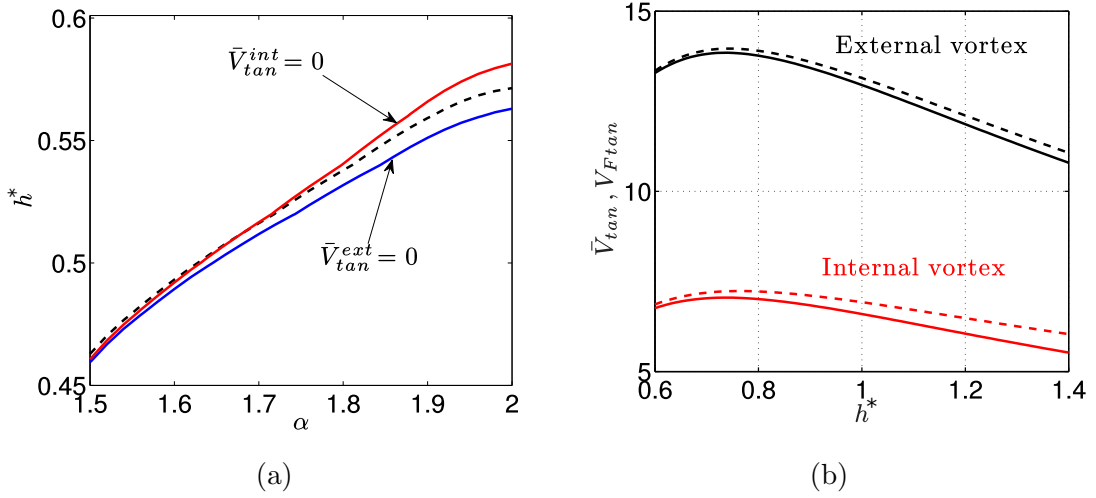


Figure 2.17: (a) Value of h^* versus α for which $\Omega_F = 0$ (black dashed line), $\bar{V}_{tan}^{ext} = 0$ (blue line), $\bar{V}_{tan}^{int} = 0$ (red line) for $R^* = 0.5$, $\varepsilon = 0.03$, $N = 1$, $\kappa = 1$. (b) Comparison of mean tangential velocity \bar{V}_{tan} (solid lines) and tangential frame velocity V_{Ftan} (dashed lines) for external and internal vortices (normalized by Γ/R_{ext}). Parameters are $R^* = 0.5$, $\alpha = 1.2$, $\varepsilon = 0.03$, $N = 1$, $\kappa = 1$.

an helix, this tangential “frame” velocity is given by

$$V_{Ftan}^{int} = -\frac{\Omega_F R_{ext} R^* + W_F h^* / (2\pi\alpha R^*)}{\sqrt{1 + h^{*2} / (2\pi\alpha R^*)^2}}, \quad V_{Ftan}^{ext} = -\frac{\Omega_F R_{ext} + W_F h^* / (2\pi)}{\sqrt{1 + h^{*2} / (2\pi)^2}} \quad (2.23)$$

for the internal and external vortex, respectively. The difference between V_{Ftan} and \bar{V}_{tan} is associated with the vortex induction. In figure 2.17b, we can observe the similar values of \bar{V}_{tan} and V_{Ftan} in the whole range of h^* between 0.6 and 1.4 for a typical case. This means that the most important part of the tangential velocity is associated with the frame velocity and the vortex induction contribution remains in general small.

Induced flow

From the point of view of applications, it is useful to know the velocity field induced by the vortex structure. An illustration of the axial and angular components of such a field in a plane perpendicular to the structure axis is shown in figure 2.18. In these contour plots, the axial velocity W_F and angular velocity Ω_F have been subtracted such that the velocity field vanishes far from the center. The vortex cores where the velocity field is smoothed have also been indicated. We clearly see that the induced velocity field exhibits strong inhomogeneities.

In figure 2.19, we show the azimuthally averaged flow versus r at different axial locations. In the core region of each vortex (at a distance smaller than a for the vortex center), each velocity profile has been replaced by a linear fit. We do see small fluctuations of the profiles between different locations but the profiles remain close to the profiles generated by N pairs of perfect helices. These ideal profiles are given (for infinitely thin vortices)

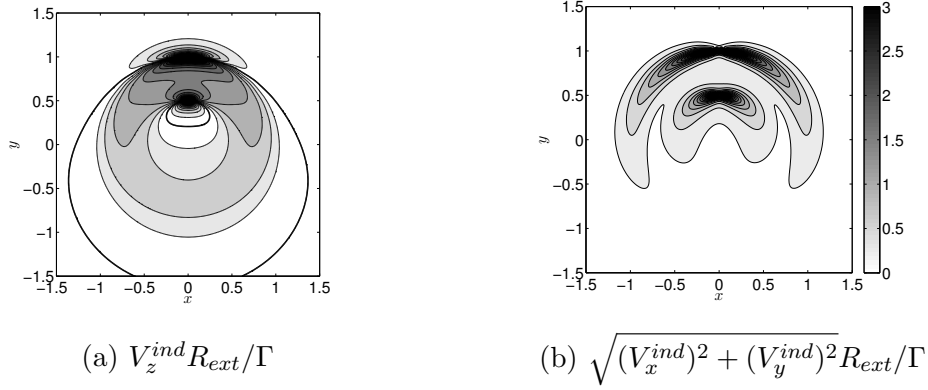


Figure 2.18: Induced velocity contours in a cross section ($z = 0$ plane) for $h^* = 1$, $R^* = 0.5$, $\alpha = 1.5$, $\varepsilon = 0.03$, $N = 1$ and $\kappa = 1$. In (a) colors are for $|V_z^{ind}|$ with the same colormap as in (b).

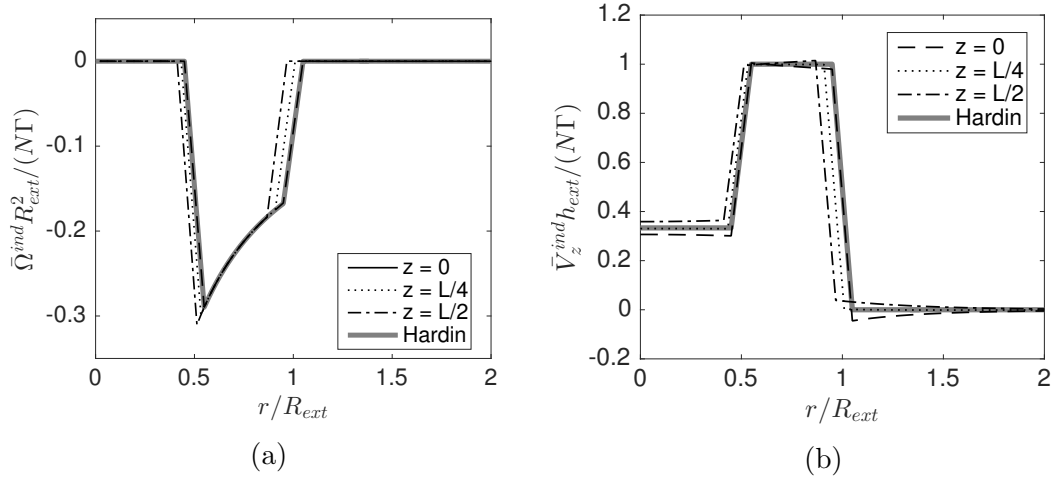


Figure 2.19: Azimuthally averaged induced velocity profile for the same parameters as in figure 2.18. Solid lines: numerical results at different axial locations. Dashed line: theoretical prediction for perfect helices using Hardin model. (a): Angular velocity $\bar{\Omega}^{ind} R_{ext}^2 / (N\Gamma)$. (b) Axial velocity $\bar{V}_z^{ind} h_{ext} / (N\Gamma)$.

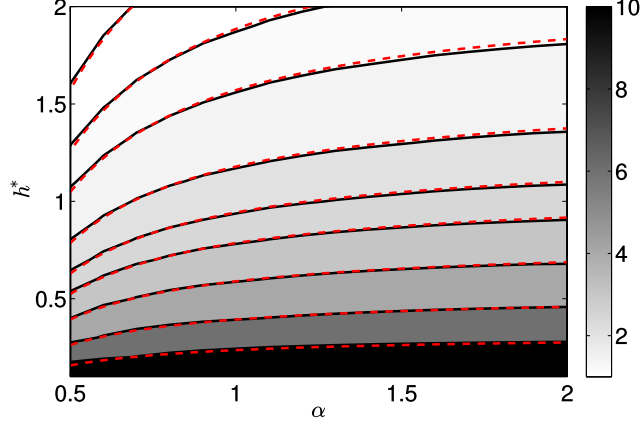


Figure 2.20: Contours of mass axial flow rate M (normalized by $\rho N \Gamma R_{ext}$) in the (α, h) plane for $R^* = 0.5$, $\varepsilon = 0.03$, $N = 1$ and $\kappa = 1$. Contours correspond from top to bottom to $\{1, 1.25, 1.5, 2, 2.5, 3, 4, 6, 10\}$. Solid lines: M ; red dashed lines: M^H .

by Hardin (1982)

$$\bar{V}_z^H = \frac{N\Gamma}{h_{ext}} \begin{cases} 1 - \frac{1}{\alpha} & \text{if } r < R_{int}, \\ 1 & \text{if } R_{int} < r < R_{ext}, \\ 0 & \text{if } r > R_{ext}, \end{cases} \quad (2.24)$$

$$\bar{\Omega}^H = \frac{N\Gamma}{R_{ext}^2} \begin{cases} -\frac{R_{ext}^2}{2\pi r^2} & \text{if } R_{int} < r < R_{ext}, \\ 0 & \text{elsewhere.} \end{cases} \quad (2.25)$$

The fluctuations are mainly associated with the radial displacement of the vortices. When the helices are less deformed, the fluctuations are smaller. It is interesting to note that the azimuthally averaged axial flow changes sign close to the axis when $h_{int} < h_{ext}$, that is $\alpha < 1$.

For the applications, it is also useful to evaluate the mass flow rate induced by the structure. The mass axial flow rate is defined by

$$M = \iiint \rho V_z^{ind} r dr d\phi. \quad (2.26)$$

For N undeformed helical pairs, we get using (2.24)

$$M^H = \rho N \Gamma \pi \left(\frac{R_{ext}^2}{h_{ext}} - \frac{R_{int}^2}{h_{int}} \right), \quad (2.27)$$

that is

$$\frac{M^H}{\rho N \Gamma R_{ext}} = \frac{\pi}{h^*} \left(1 - \frac{(R^*)^2}{\alpha} \right). \quad (2.28)$$

This expression provides a good approximation of the mass flow rate of the deformed structure, as observed in figure 2.20 for a typical example.

Note that M^H changes sign when $\alpha < (R^*)^2$. In this regime, the induced axial flow is sufficiently negative close to the axis to inverse the positive mass flow rate occurring between the internal and external vortices. For the parameters of figure 2.20, this is expected for very small α ($\alpha < 0.25$).

2.3.3 Analysis of the effect of a varying core size

We have seen that the tangential velocity varies along each vortex structure when it is deformed. This implies that each vortex experiences a stretching field that in principle induces a variation of its core size. In this section, our objective is to quantify this effect.

In an inviscid framework, the way the core size varies is simply given by the conservation of the mass flux in the vortex core which imposes

$$a^2 V_{tan} = \text{Cst}. \quad (2.29)$$

As soon as a changes, the self-induced velocity is modified and therefore a different equilibrium solution is obtained.

In figure 2.21, we have analysed the effect of a varying core size in an extreme case ($R^* = 0.8$, $h^* = 1.4$, $\varepsilon = 0.03$, $\alpha = 1.4$, $N = 1$, $\kappa = 1$). As seen in figure 2.15(b), for this value of R^* , the variations of V_{tan} are the largest: they reach 32% for the internal vortex, and 23% for the external one. In figure 2.21(a), we have plotted the variation of the core size in a period for the converged solution in both vortices. The variations of the core size are weaker than of the tangential velocity as expected from (2.29). They are around 10% for the internal vortex, and 7% for the external vortex, with respect to the mean core size $a = 0.03$. In figure 2.21(b), the radial position of the vortices is shown. The solution with a varying core size is compared to the solution with a constant core size. We observe that the difference between both solutions is very small. The largest gaps between both radial positions are 0.78% and 0.66% for internal and external vortices respectively. In terms of moving frame velocities, the differences are also extremely small: we obtain the values $W = 1.826$ and $\Omega = 3.697$ for a varying core size, while we had $W = 1.809$ and $\Omega = 3.610$ for a constant core size.

This comparison guarantees that the effects of a varying core size is negligible for all the cases that we have considered. It a posteriori justifies the use of the approximation of a constant core size in our work.

2.3.4 Discussion in the context of rotors

In this section, we discuss our solutions in the context of rotor wakes. Our objective is to identify as a function of the geometrical parameters which far wake situations the solutions could possibly describe. In other words, if a solution was able to represent the flow generated by rotor, which rotor configuration it would be.

In the previous sections, we have obtained the frame where each solution is stationary. If the flow was created by a rotor, this frame would necessarily be a frame attached to a blade. In other words, the angular velocity $-\Omega_F$ would be the rotation rate of the rotor and $-W_F$ the external wind velocity. Moreover, in the far field, the vortices which have been created by the rotor, would have to move away from it. From the direction of

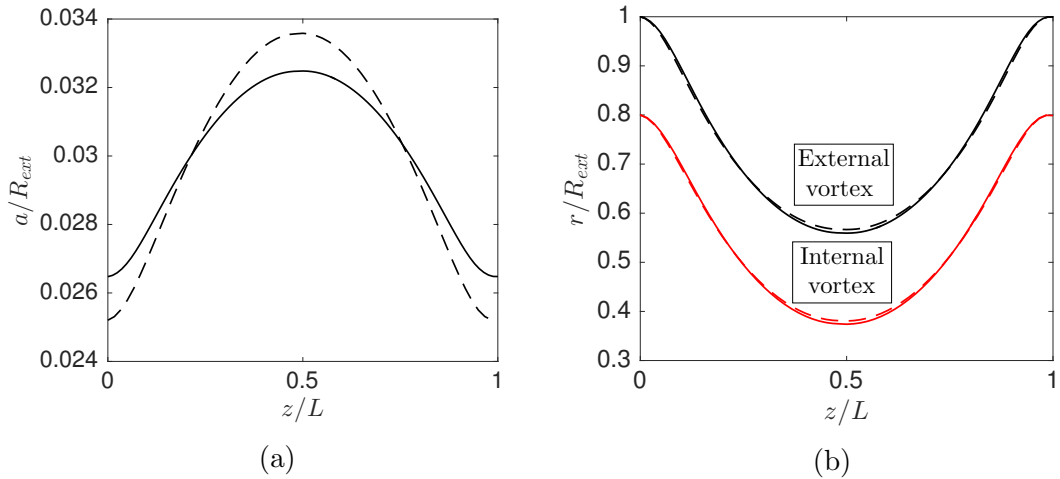


Figure 2.21: (a) Variation of the core size a/R_{ext} for the external (solid line) and internal (dashed line) vortex. The mean core size value in each vortex is $a/R_{ext} = 0.03$. (b) Radial position of the internal and external vortices for a constant core size (dashed line) and for a variable core size obtained using (2.29) (solid line). The parameters in both figures are $R^* = 0.8$, $h^* = 1.4$, $\alpha = 1.4$, $N = 1$, $\kappa = 1$ and a mean core size $a/R_{ext} = 0.03$.

propagation of the vortices, which is given by the sign of the mean tangential velocity, we can then deduce the side where the rotor should be. For example, if $\bar{V}_{tan} > 0$, the vortices move in the positive direction, the rotor should then be located on the negative side.

By analysing the directions of propagation of the vortices and of the external wind, one can build the diagram shown in figure 2.22. The different domains are limited by the curves $W_F = 0$ and $\Omega_F = 0$ and the line $\alpha = 1$, which correspond to changes of signs of the direction of propagation of the vortices or of the external wind. In this figure, we have also indicated the typical azimuthally averaged axial flow corresponding to each regime. For example, in the white region on the right of the line $\alpha = 1$, $W_F > 0$, $\bar{V}_{tan}^{ext} < 0$, $\bar{V}_{tan}^{int} < 0$ and $M > 0$: both vortices moves in the same negative direction as the external wind, which is opposite to the direction of the mass flow rate. Assuming a positive axis downwards, this situation corresponds to the so-called windmill brake regime of an helicopter: the helicopter is going downwards, while the flow and the vortices are going upwards with respect to the helicopter rotor. This regime also corresponds to the wind turbine regime. The difference with the other windmill brake regime obtained for $\alpha < 1$ is in the azimuthally averaged axial flow which is stronger than the external wind close to the axis in that case.

In the light gray regions, the vortex velocities are positive while $W_F < 0$. This regime corresponds to a climbing regime: the vortices moves downwards as the external flow and the mass flow rate. In the dark gray regions, W_F and the vortex velocities are positive as the mass flow rate. This situation corresponds to a slow descending regime: the vortices moves downwards while the external flow goes upwards. It does not tell us anything on the behavior of the vortices close to the rotor. It is not excluded that the vortices exhibit a complex pattern near the rotor as observed in the so-called vortex ring state (Drees & Hendal, 1951; Quaranta, 2017; Durán Venegas & Le Dizès, 2018).

Note that the curve $\Omega_F = 0$ is not exactly the limit between the windmill brake regime

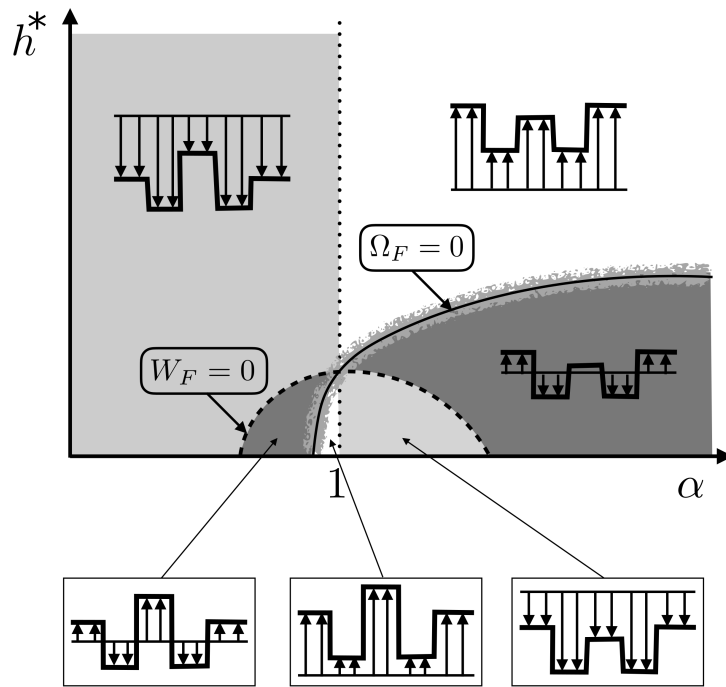


Figure 2.22: Diagram of the different rotor flow regimes. White regions: windmill brake regime or wind turbine regime (both vortices are going upwards as the external wind). Light gray regions: ascending regime (both vortices are going downwards as the external wind). Dark gray regions: slow descending regime and vortex ring state (both vortices are going downwards while the external wind is going upwards). Close to the line $\Omega_F = 0$, there exist a small region where one vortex is going upwards while the other is going downwards: such a solution cannot describe the (far) wake of a rotor.

and the slow descending regime. There is actually a small region close to this curve where the solution cannot correspond to any helicopter flight regime. This region has been displayed in figure 2.17a for a particular set of parameters. In this region, internal and external vortices move in opposite directions. For this reason, they cannot be created by a single rotor located far away.

2.4 Near-wake solutions

In this section, the particularities of the framework for the near-wake are presented, including the coupling with far-wake solutions obtained in the previous section. This framework will be used in the next sections to obtain stationary solutions for the geometry of the wake. Firstly, the standard Joukowski problem will be addressed, when the hub vortex is located on the axis. Then, generalized solutions will be obtained where the emission point of the hub vortex is displaced from the axis. Finally both cases will be compared.

2.4.1 Framework

To obtain the solutions for the near wake, a similar procedure as for the far-wake (section 2.3.1) is followed. Just a few modifications have to be made concerning induced velocity contributions and boundary conditions.

Under the same assumptions of small core size vortices and inviscid framework, the concentrated filaments of vorticity move in the fluid as material lines advected by the velocity field:

$$\frac{d\boldsymbol{\xi}}{dt} = \boldsymbol{U}(\boldsymbol{\xi}) = \boldsymbol{U}^\infty + \boldsymbol{U}^{\text{ind}}(\boldsymbol{\xi}), \quad (2.30)$$

where $\boldsymbol{\xi}$ is the position vector of the vortex filament, \boldsymbol{U} the velocity field, composed of the external velocity \boldsymbol{U}^∞ and the induced velocity $\boldsymbol{U}^{\text{ind}}(\boldsymbol{\xi})$ generated by the vortex filaments. This induced velocity can be in turn decomposed in four velocity contributions:

$$\boldsymbol{U}^{\text{ind}}(\boldsymbol{\xi}) = \boldsymbol{U}^{\text{tip}}(\boldsymbol{\xi}) + \boldsymbol{U}^{\text{hub}}(\boldsymbol{\xi}) + \boldsymbol{U}^{\text{blade}}(\boldsymbol{\xi}) + \boldsymbol{U}^{\text{FW}}(\boldsymbol{\xi}), \quad (2.31)$$

where $\boldsymbol{U}^{\text{tip}}$ is the velocity induced by the tip helical vortices, $\boldsymbol{U}^{\text{hub}}$ is the contribution from the hub vortex, $\boldsymbol{U}^{\text{blade}}$ is the contribution from the bound vortex on the blade and $\boldsymbol{U}^{\text{FW}}$ is the induction effect from the far-wake. The velocity induced by the vortices is calculated with Biot-Savart law. The discretization and the application of Biot-Savart law at each point is done as in section 2.3.

Far-wake contribution

To model the effect of the far wake, it is imposed that, after a certain distance from the rotor (figure 2.23), the wake adopts the geometry of the far-wake solutions previously calculated in section 2.3. The imposed far-wake geometry is extended from the end of the calculation domain for a given number of turns. The far-wake velocity contribution $\boldsymbol{U}^{\text{FW}}$ is calculated as the velocity induced by the far-wake structure on the vortices of the calculation domain.

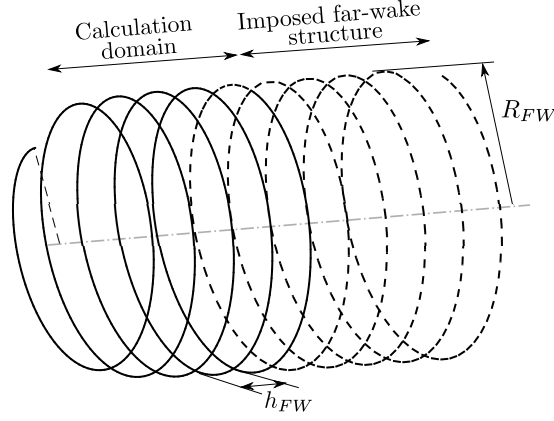


Figure 2.23: Schematic of the complete vortical structure generated at the wake (to simplify the figure, only tip vortex from a single blade is represented). In solid line, the calculation domain. In dashed line, the prescribed far-wake structure.

To obtain the geometrical parameters (2.14) of the far-wake structure, we first calculate the wake geometry assuming that the vortices in the far wake are perfect helices. So, in the first iteration, the far-wake contribution is obtained by calculating the induction of N pairs of undeformed helical vortices. After obtaining this first approximation, the actual far-wake structure is calculated as in section 2.3 with the following geometrical parameters:

$$R^* = R_{\text{hub}}^{\text{FW}}/R_{\text{tip}}^{\text{FW}}, \quad h^* = h_{\text{tip}}^{\text{FW}}/R_{\text{tip}}^{\text{FW}}, \quad \alpha = h_{\text{hub}}^{\text{FW}}/h_{\text{tip}}^{\text{FW}}, \quad \varepsilon^* = a/R_{\text{tip}}^{\text{FW}}. \quad (2.32)$$

The value of the parameters is adjusted iteratively until convergence of the solution for the whole wake.

Steady solutions. Equations

We are looking for helical wake structures that are stationary in the rotor frame. This means that the vortices should be steady in the frame rotating at the angular velocity Ω of the rotor. This condition of steadiness implies a constraint on the velocity field with respect to the vortex structures: it should be tangent to the structure at every point. This condition reads

$$(\mathbf{U}^\infty(\boldsymbol{\xi}_j^m) + \mathbf{U}^{\text{ind}}(\boldsymbol{\xi}_j^m)) \times \boldsymbol{\tau}_j^m = 0, \quad (2.33)$$

where the external field \mathbf{U}^∞ is the combination of the external axial velocity $V_\infty \mathbf{e}_z$ and the azimuthal velocity $-r\Omega \mathbf{e}_\psi$. This condition can be also written for each vortex filament as

$$\frac{dr}{d\phi} = \frac{V_r^{\text{ind}}}{\Omega^{\text{ind}} - \Omega}, \quad \frac{dz}{d\phi} = \frac{V_z^{\text{ind}} + V_\infty}{\Omega^{\text{ind}} - \Omega} \quad (2.34)$$

where $r(\phi)$ and $z(\phi)$ are the radial and axial positions of the filament at the azimuthal position ϕ of the helix. Concerning the boundary conditions, it has been imposed that the free vortices are attached to the blade at their point of emission. Then, if the azimuthal origin is fixed at the blade position, the conditions of attachment are:

$$r_{\text{ext}}(0) = R_{\text{tip}}, \quad r_{\text{int}}(0) = R_{\text{hub}}, \quad z_{\text{ext}}(0) = 0, \quad z_{\text{int}}(0) = 0. \quad (2.35)$$

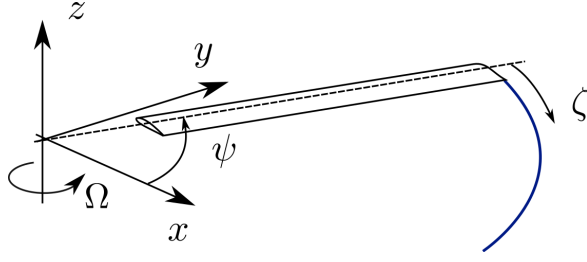


Figure 2.24: Local reference frame used by Leishman *et al.* (2002)

Problem parameters

The problem is governed by 4 non-dimensional parameters:

$$\lambda = \frac{R_{\text{tip}}\Omega_R}{V_\infty}, \quad \eta = \frac{\Gamma}{R_{\text{tip}}^2\Omega_R}, \quad R_b^* = \frac{R_{\text{hub}}}{R_{\text{tip}}}, \quad \varepsilon = \frac{a}{R_{\text{tip}}}, \quad (2.36)$$

where λ is known as the tip-speed-ratio and η and ε represent the vortex strength and the vortex core size. Note that λ can be either positive or negative; positive values correspond to descending flight and wind turbine regimes and negative values to ascending flight. The parameter R_b^* is the radii ratio of the vortex emission points at the rotor blades. The parameter ε , which measures the vortex core size, is assumed small as before.

The details for the computation of far-wake and near-wake solutions are presented in the appendix.

2.5 $R_b^* = 0$ case (Standard Joukowski model)

In this section, an analysis of the wake is addressed with the standard Joukowski model, that is, when the hub vortex is on the axis. After introducing the particularities of this case, a parametric analysis is carried out to obtain the range of regimes reached with the model. Then, the velocity field induced by the wake is calculated and employed to compute the mass flow across the rotor for different rotor regimes. Finally, the model is used to calculate the power extracted from a wind turbine.

2.5.1 Framework

Stationary solutions for the particular case $R_b^* = 0$ can be obtained with the same procedure as presented in section 2.4.1. The only difference is the hub vortex that is considered as a straight filament of circulation $-N\Gamma$ instead of a braid of helical vortices. Fixing the parameter R_b^* to 0, the problem is just described by four parameters: λ , η , ε and N . Contrarily to the generalized Joukowski model, N cannot be fixed to 1 for the classical model. Indeed, the velocity induced by a single helix exhibits on the helix axis a radial component: a straight vortex placed on the axis cannot remain there. A value of $N = 2$ will be fixed for standard Joukowski model solutions.

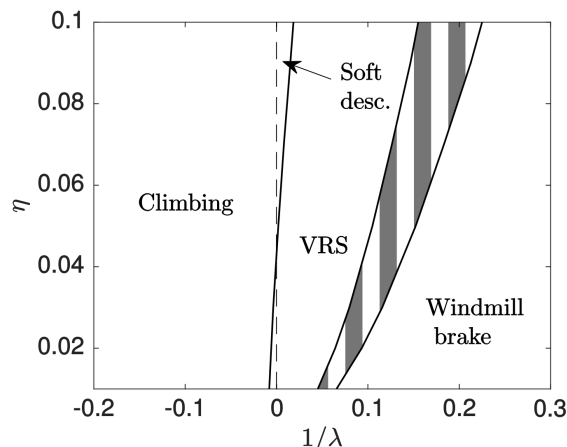


Figure 2.25: Map of the rotor regimes as a function of λ and η . The striped band represents the region where solutions cannot be obtained with the presented model.

In this section, solutions are obtained by a slightly different procedure. The free-vortex discretization scheme presented by Leishman *et al.* (2002) will be used, where vortex position is parametrized through two angular coordinates ψ and ζ :

$$\frac{d\boldsymbol{\xi}(\psi, \zeta)}{dt} = \Omega_R \left[\frac{\partial \boldsymbol{\xi}(\psi, \zeta)}{\partial \psi} + \frac{\partial \boldsymbol{\xi}(\psi, \zeta)}{\partial \zeta} \right] = \mathbf{U}(\boldsymbol{\xi}) \quad (2.37)$$

where $\psi(t)$ is the angular position of the blade at a time t and $\zeta(t)$ is the total azimuth of the blade from its position when the element $\boldsymbol{\xi}$ was created (figure 2.24). In a frame rotating with the blade at the angular velocity Ω_R , the steady problem can be expressed as:

$$\frac{dr}{d\zeta} = \frac{1}{\Omega_R} U_r, \quad \frac{d\phi}{d\zeta} = \frac{1}{\Omega_R} (\Omega - \Omega_R), \quad \frac{dz}{d\zeta} = \frac{1}{\Omega_R} (U_z + U_\infty). \quad (2.38)$$

where r , ϕ and z are the radial, angular and axial position of the vortex at ζ and U_r , Ω and U_z are the respective components of the induced velocity.

This formulation gives geometrically equivalent solutions to those obtained from equations (2.34). The only difference is a different angular discretization of the vortices (A comparison of both formulations will be addressed in the appendix). Now, three variables have to be calculated instead of two, increasing the computational cost; this formulation will however facilitate the stability analysis of the solutions that is performed in chapter 3.

2.5.2 Wake solutions

When the tip-speed-ratio λ and vortex strength parameter η are modified, different rotor regimes are covered. Four main regions can be found (figure 2.25): ascending and descending flight, Vortex Ring State (VRS) and windmill brake flight/wind turbine regime. In the rotor frame, the external flow is going downwards when λ is negative and upwards

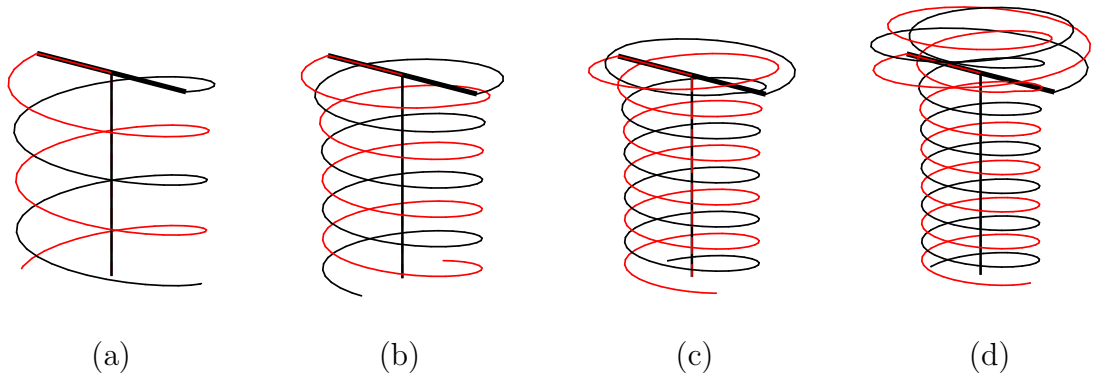


Figure 2.26: Wake structure for a two bladed rotor in (a) $\lambda = -10$ ascending flight, (b) $\lambda = \infty$ hovering flight, (c) $\lambda = 19$ descending flight and (d) $\lambda = 11$ VRS - descending flight. For all cases $\eta = 0.05$ and $\varepsilon = 0.01$.

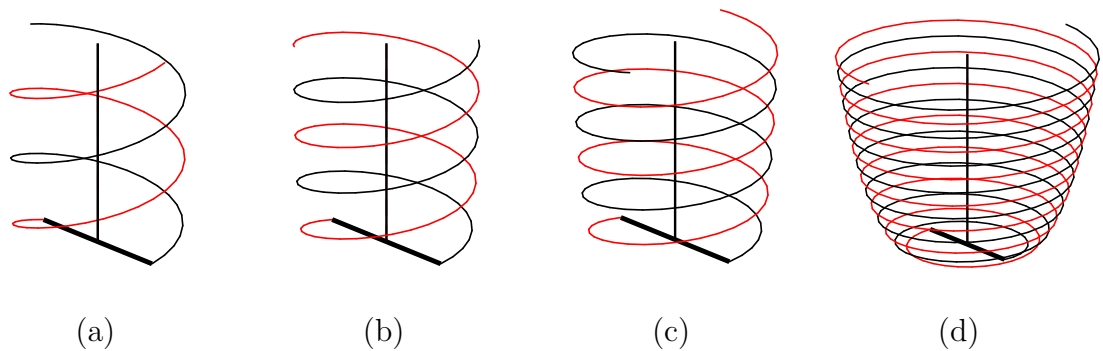


Figure 2.27: Wake structure for a two bladed rotor in windmill brake flight configuration (a) $\lambda = 3.3$, (b) $\lambda = 4.3$, (c) $\lambda = 5.1$ and (d) $\lambda = 6.1$. For all cases $\eta = 0.05$ and $\varepsilon = 0.01$.

when it is positive. So negative values of λ correspond to climbing flight, $\lambda = \infty$ to hovering flight and positive values of λ to descending flight, which includes soft descending, windmill brake flight and VRS cases. The specific value of λ where the transition between two regimes is produced depends on the vortex strength η . Two main regions of solutions are obtained: the wind turbine cases for the largest values of $1/\lambda$, where the vortices go upwards (figure 2.27), and the rest, where vortices go downwards (figure 2.26). Between both regions, there is a strip of parameter for which we have not been able to obtain any solution (figure 2.25).

In figure 2.26, the shape of the vortices is displayed for climbing, hovering and VRS regimes, which correspond to the normal flight situations on a helicopter. For these cases, the structure goes downwards and is subject to contraction. This contraction can also be observed in figure 2.28a, where the radial trajectories of the vortices are shown for several values of λ . The contraction increases when λ becomes more negative, that is when the climbing speed decreases. This contraction process continues when the climbing speed vanishes and changes sign, that is when moving to a slow descent flight regime corresponding to large positive values of λ . In this regime, although the external flow

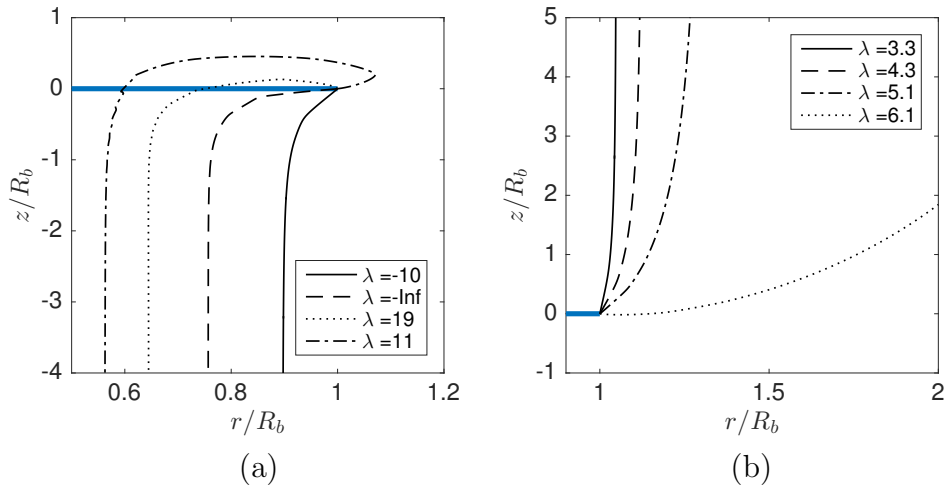


Figure 2.28: Radial position of the wake in the axial direction for different tip-speed-ratio values. With $\eta = 0.05$ and $\varepsilon = 0.01$.

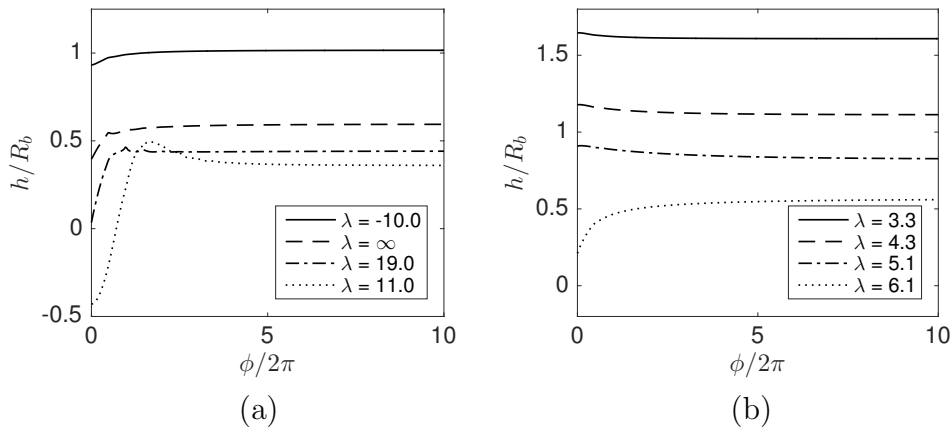


Figure 2.29: Evolution of the local pitch along the wake for different tip-speed-ratio values. With $\eta = 0.05$ and $\varepsilon = 0.01$.

goes upwards, the downwards flow induced by the vortices is stronger. If the descending speed is increased, the vortices can be emitted upwards and then change direction to finally go downwards and cross the rotor plane. Owing to the displacement of the vortices above and below the rotor, we denote this regime as the VRS regime. With this definition, the transition to the VRS regime corresponds to the situation where the vortices are emitted towards the center tangentially to the rotor plane. The VRS regime is reached at a different value of λ depending on η . When η is small, we observe that the VRS regime appears for a negative λ (see figure 2.25, where the VRS frontier crosses the hovering flight line $1/\lambda = 0$ at $\eta = 0.052$, for $\varepsilon = 0.05$).

If $1/\lambda$ increases, there is a critical value of $1/\lambda$ above which a downwards wake ceases to exist. It is above a second critical value of $1/\lambda$ that a new solution with a wake going upwards is obtained. For these large values of $1/\lambda$, the wake expands radially. It corresponds to the windmill brake regime or wind turbine regime. In figure 2.27, some

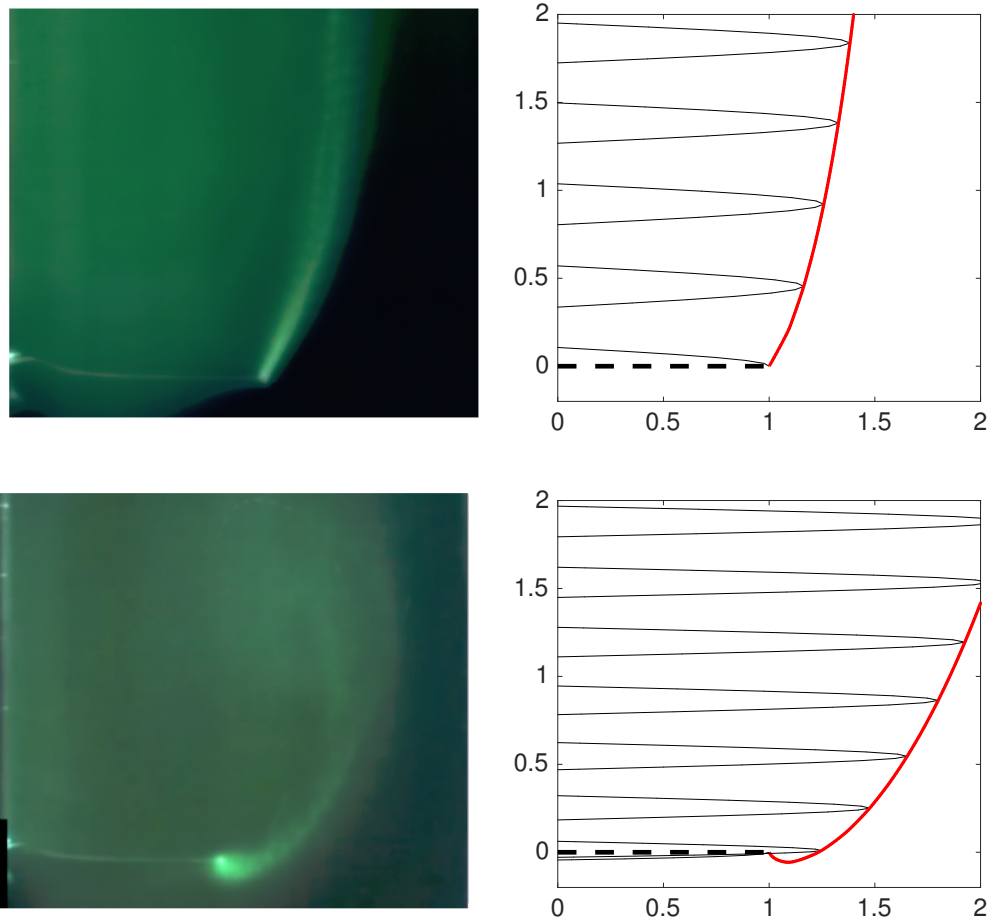


Figure 2.30: Time-averaged dye visualization of the wake behind half of the rotor plane in a wind turbine configuration approaching to VRS at $\lambda = 7.23$ (upper) and $\lambda = 11.2$ (lower) (from Quaranta, 2017). Right plots: qualitative comparison of the wake geometry with the numerical model for wind turbine configuration at high tip-speed-ratio (up: $\lambda = 8$, down: $\lambda = 10$. $\eta = 0.02$, $\varepsilon = 0.01$). The rotor disc is represented in black dashed line. In black solid line, the projection of the tip vortices and, in red, their radial evolution.

vortical structures of wind turbine regime are plotted for different values of λ and, in figure 2.28b, their radial trajectories. As observed for the helicopter flight regimes, the stronger the external flow is (that is, the smaller λ), the less deformed the structure is. For slow external flow in the wind turbine regime, there is a limit value of λ –just before the interruption of the solutions– from which the vortices are emitted downwards and then cross the rotor plane going upwards (see the case of $\lambda = 6.1$ in figure 2.28b). This kind of structure was found experimentally by Quaranta (2017) just before the transition to VRS from a windmill brake regime (figure 2.30). Information on vortex circulation and core size have not been measured in the experiment, so a quantitative comparison cannot be performed. However a very good qualitative agreement with the wake geometry is found using the numerical model

The intervals of λ of existence of downward and upward structure do not seem to overlap. For all the considered parameters, it was found an interval of λ where both

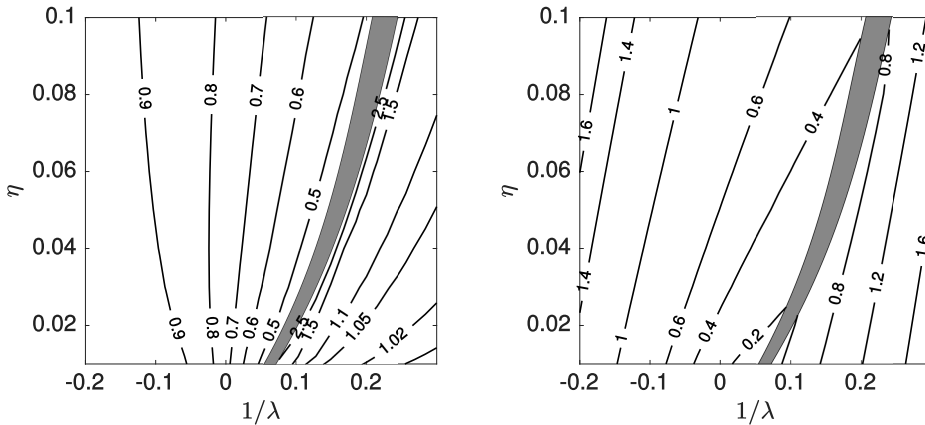


Figure 2.31: Contour maps of (a) radius and (b) pitch of the helix in the far wake, non-dimensionalized by R_{tip} . With $\varepsilon = 0.01$.

solutions cease to exist.

In figure 2.31a the radius of the far-wake helix is shown in the (λ, η) plane. For normal helicopter regimes, it can be seen how the contraction of the structure grows as $1/\lambda$ decreases from a high speed climbing flight (strongly negative $1/\lambda$) to VRS regime (positive $1/\lambda$). For wind turbine regime, the expansion is minimal for high descending speed (large $1/\lambda$) and it grows with λ . The effect of η is minimal around hovering flight, where a constant wake contraction of 72% is observed. Similarly, the lines of constant radial deformation of the helices seems to follow the frontier of downwards/upwards solutions.

The evolution of the local pitch h along the helical structure is shown in figure 2.29. As for the radial trajectories, there are strong variations of the pitch near the rotor plane, but after a few turns it reaches a constant value. By definition, we have chosen h to be positive when the vortices go downwards. Negative values of h then mean that the vortices go upwards. In figure 2.31b, the pitch h_∞ of the far-wake helix in the (λ, η) plane is represented. In climbing flight regime, the pitch gets smaller when the external velocity is reduced. This tendency continues beyond the hovering flight, when the climbing speed vanishes and we move to a slow descent regime. In wind turbine regime, the pitch grows with the external flow.

2.5.3 Induced velocities

In our framework, the condition to obtain stationary solutions is to have a velocity field parallel to the structure. However, this tangential velocity is not uniform. We observe that the tangential velocity is larger near the rotor plane and decreases progressively to a constant value in the far-wake. As explained in the previous section, this variation of the tangential velocity produces a stretching field on the vortices that in principle induces a variation of its core size. However, as it was illustrated in section 2.3.3, for this amount of variation on the tangential velocity, the variation of the core size and its effect are not important.

For the applications, it is useful to know the velocity field induced by the vortex struc-

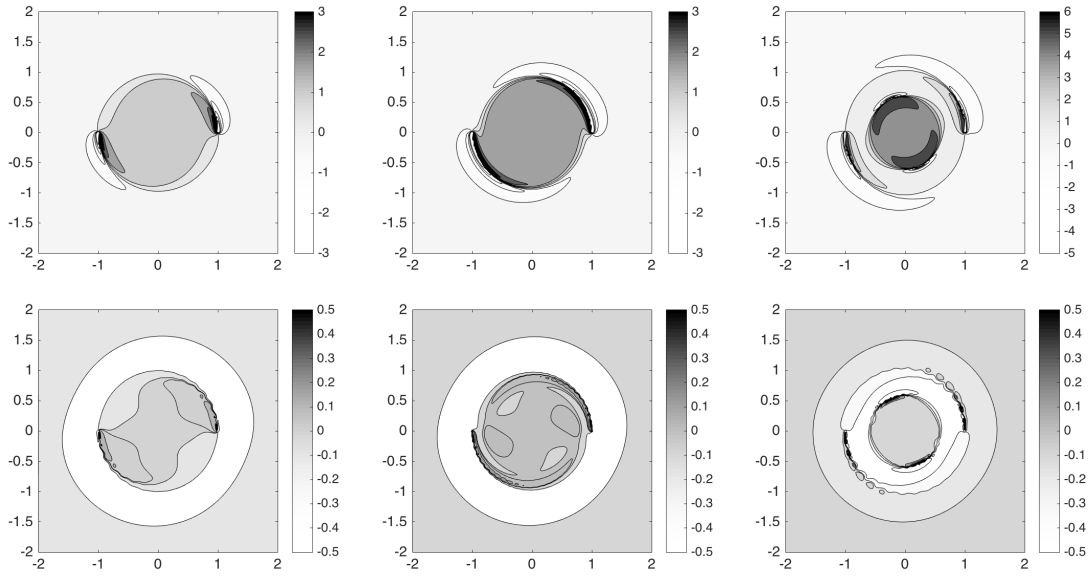


Figure 2.32: Induced velocity contours in a cross section ($z=0$ plane) for $\eta = 0.05$, $\varepsilon = 0.01$ and $\lambda = -15$ (left plots) $\lambda = \infty$ (center), $\lambda = 11$ (right). $\eta = 0.05$, $\varepsilon = 0.01$. Upper plots: $V_z^{\text{ind}} R_{\text{tip}}/\Gamma$, lower plots: $V_\phi^{\text{ind}} R_{\text{tip}}/\Gamma$.

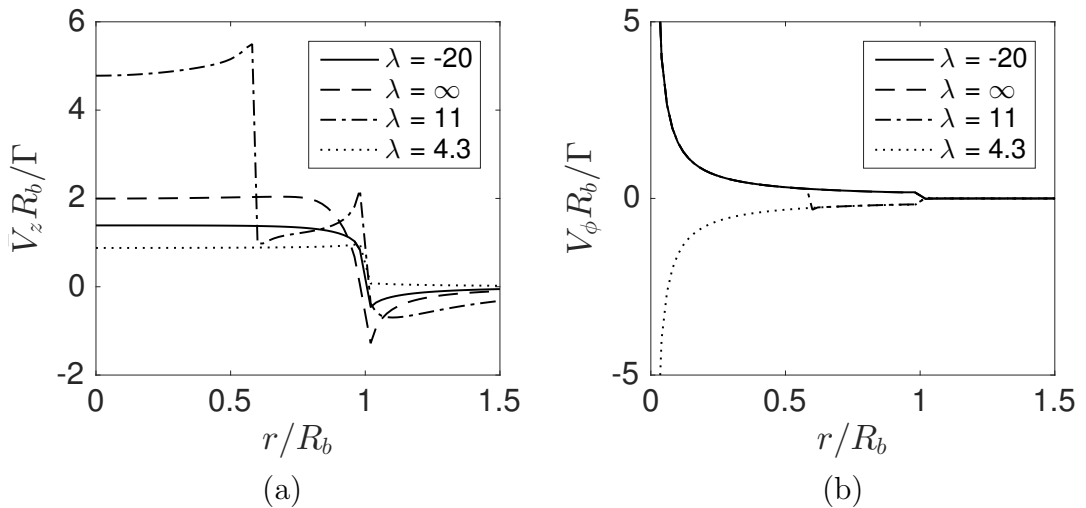


Figure 2.33: Azimuthally averaged induced velocity in axial and azimuthal directions in the rotor plane for different values of λ with $\eta = 0.05$ and $\varepsilon = 0.01$.

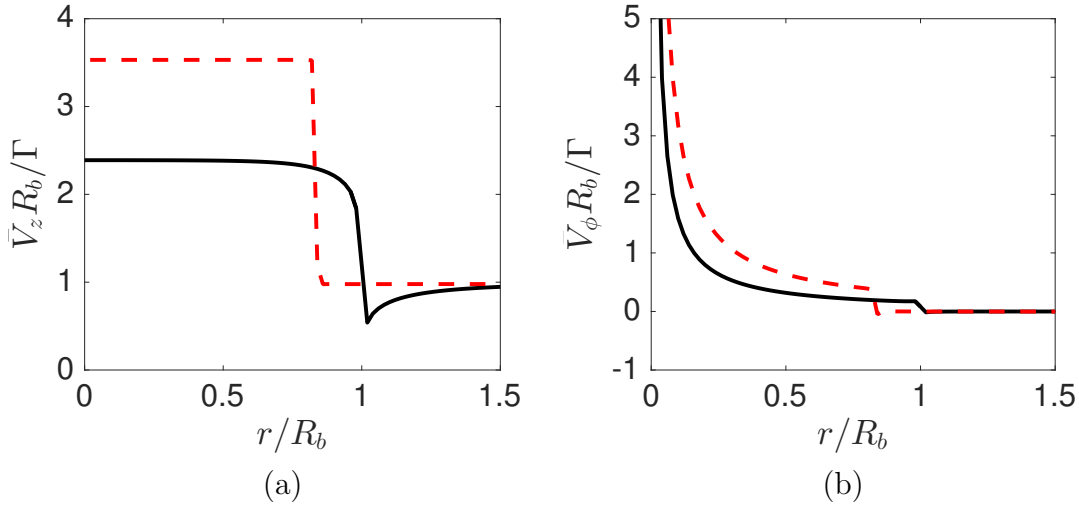


Figure 2.34: Azimuthally averaged induced velocity in axial and azimuthal directions in the rotor plane (solid black) and in the far-wake (dashed red) for $\lambda = -20$, $\eta = 0.05$ and $\varepsilon = 0.01$. For the axial velocity, the external flow is also included.

ture. Figure 2.32 shows the axial and angular components of the velocity field induced at the rotor plane for different helicopter regimes. In these contour plots, the external velocity V_∞ and the angular velocity Ω_R have been subtracted such that the velocity field vanishes far from the center. For a clearer visualization, the induction of the bound vortex has not been plotted. We can see that the homogeneous character of the induced velocity field varies with λ . For climbing and hovering configurations (figure 2.32, left and center), the velocity field is approximately homogeneous inside the rotor disc, with strong variations near the vortices. However, for VRS regimes, the vortices cross the rotor disc producing a very heterogeneous velocity field (figure 2.32, right). For all cases, as for infinite helices (Hardin, 1982; Saffman, 1992), the induced flow is mainly concentrated inside the rotor disc, and vanishes rapidly outside of it.

Figure 2.33 shows the azimuthally averaged flow versus r in the rotor plane for different rotor regimes. In the core region of each vortex (at a distance smaller than a from the center of the vortex), each velocity profile has been replaced by a linear fit. For the axial flow, we obtain similar profiles in almost all the regimes, with a constant upwards flow inside the rotor disc and a varying downwards flow outside that vanishes far from the rotor disc. The total flow grows when the climbing velocity is reduced and also in soft descending flight and VRS regimes. In VRS, two different regions are observed inside the rotor disc, that are delimited by the location where the vortices cross the rotor plane. For the induced azimuthal velocity, the flow profiles are very similar for all the regimes, in clockwise direction for wind turbine regime and counterclockwise for the rest. Outside the rotor disc, the azimuthal flow is inexistent; inside, it is not zero but it vanishes asymptotically as $\bar{V}_\phi \sim 1/r$. For $\lambda = -20$ and $\lambda = \infty$, both profiles are almost equivalent. In VRS, it is also equivalent in the inner region, inside the position where the vortices cross the rotor disc; from this point to the border of the rotor disc, it changes direction and overlaps with the wind turbine curve.

In figure 2.34, the azimuthally averaged flow is compared in the rotor plane and

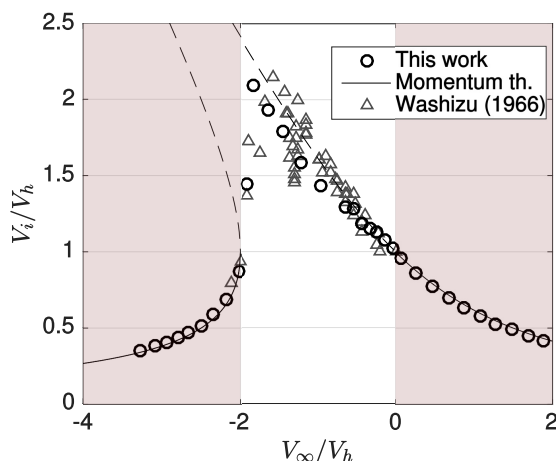


Figure 2.35: Induced velocity variation as a function of climb and descent velocity. Comparison with momentum theory and experimental data from Washizu *et al.* (1966). In coloured background, the regions where momentum theory applies.

the far-wake for a climbing flight case ($\lambda = -20$). For both cases, similar profiles are found. The induced axial flow is constant inside the wake and the rotor disc and vanishes outside. As expected for a climbing flight regime, the flow is accelerated and the induced velocity is higher in the far-wake. In this case, the total velocity in the rotor disc has approximately the mean value between the external flow and the velocity in the far-wake, so the description of momentum theory for the flow on the rotor (1.5) is verified. The induced azimuthal flow is also similar for both cases. It is zero outside the vortices and it vanishes as $\bar{V}_\phi \sim 1/r$ inside. In non-zero regions, the azimuthal induced velocity is the double at the far-wake compared to the rotor plane: $\bar{V}_\phi^{\text{FW}} r/\Gamma \simeq 0.3182$ and $\bar{V}_\phi^{\text{R}} r/\Gamma \simeq 0.1591$

It is common in the literature (see Leishman, 2006) to use the averaged induced velocity V_i crossing the rotor disc to estimate the performance of a rotor. More specifically, one considers the induced velocity ratio V_i/V_h for each climb velocity ratio V_∞/V_h , where V_h is the induced velocity V_i in the hovering regime. In our case, we calculate the induced velocity as:

$$V_i = \int_0^{R_b} r \bar{V}_z(r) dr / R_b^2. \quad (2.39)$$

As it was observed in figure 2.33, the averaged velocity inside the rotor disc is almost constant, so the induced velocity V_i will be very close to the averaged velocity observed on the axis. This does not happen for VRS regimes, where there are different flow regions inside the rotor disc.

The induced velocity ratio can be approximated with the Momentum theory (Leishman, 2006), given by the Froude-Rankine limit. However, this approximation is not valid for soft descending flight and VRS regimes. For these particular cases, the performance of the rotor is normally measured experimentally. Figure 2.35 shows the induced velocity ratio against the climb velocity ratio and compares it with the Froude-Rankine limit and some experimental results from Washizu *et al.* (1966). The agreement with the momentum theory is very good for climbing flight and wind turbine regimes, that is, for climb

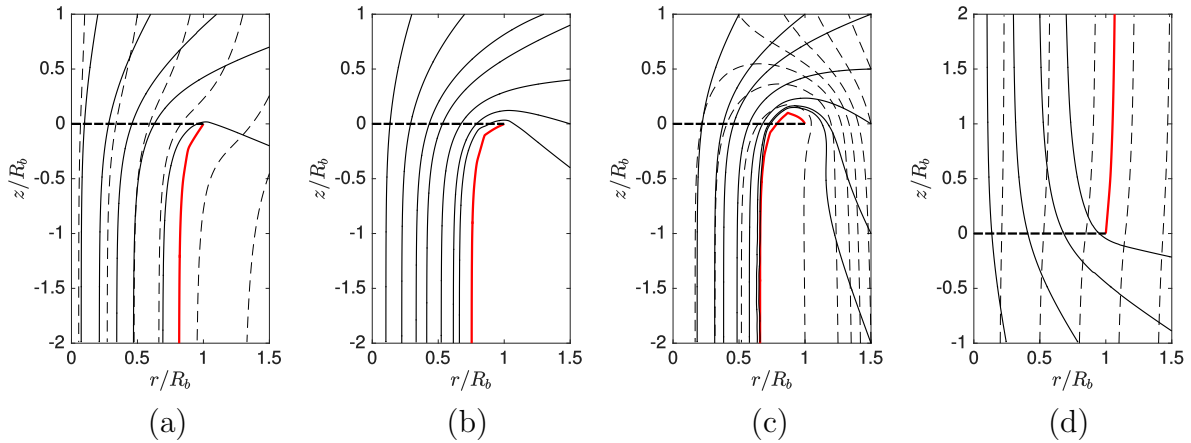


Figure 2.36: Streamlines of the averaged azimuthal flow for (a) $\lambda = -10$ (b) $\lambda = \infty$ (c) $\lambda = 20$ (d) $\lambda = 4$ with $\eta = 0.05$ and $\varepsilon = 0.01$. Black solid line: induced flow. Black dashed line: total flow. Red solid line: radial position of the tip vortex. Black dotted line: rotor disc.

velocity ratios greater than 0 and smaller than -2. For soft descending and VRS regimes, that is, for $-2 < V_\infty/V_h < 0$, the calculated induced velocity ratio is in good agreement with the experimental measurements.

In figure 2.36, the streamlines of the azimuthally averaged flow are displayed in the (r, z) plane for several flight regimes. In solid lines are plotted the streamlines of the induced flow while the total flow is represented with dashed lines. In fast climbing flight and wind turbine regimes (figures 2.36a and 2.36d), the external flow dominates, so the total flow remains unidirectional. When the external flow is reduced, the induced flow becomes more important, until the limit case of the hovering flight regime (figure 2.36b), where the external flow is zero. In VRS, the flow becomes bidirectional (figure 2.36c): outside of the vortical tube the flow goes upwards, while it goes downwards inside of it. This change of direction is associated with a loop of the streamlines around the border of the rotor disc. It is important to notice that these streamlines are obtained under an axisymmetric flow assumption. However, the real flow induced by an helical vortex is not that homogeneous (2.32). For this reason, although the helical vortex correspond with a streamline of the complete 3D flow, the projection of the helical vortex in the (r, z) plane does not really correspond with an streamline of the azimuthally averaged flow.

The total mass rate crossing the rotor disc can be easily calculated by integrating the azimuthally averaged flow:

$$M_T = 2\pi\rho \int_0^{R_b} (V_\infty + \bar{V}_z^{\text{Ind}}(r))rdr, \quad (2.40)$$

where ρ is the density of the fluid. In figure 2.37 a contour map of the non-dimensional mass flow rate $M_T/\pi\rho R_b^3\Omega$ is shown in the $(1/\lambda, \eta)$ plane. When external flow speed is high or vortex circulation is small, the influence of η on the mass flow rate vanishes and it mainly depends on the tip speed ratio. A simple analytic expression can be obtained

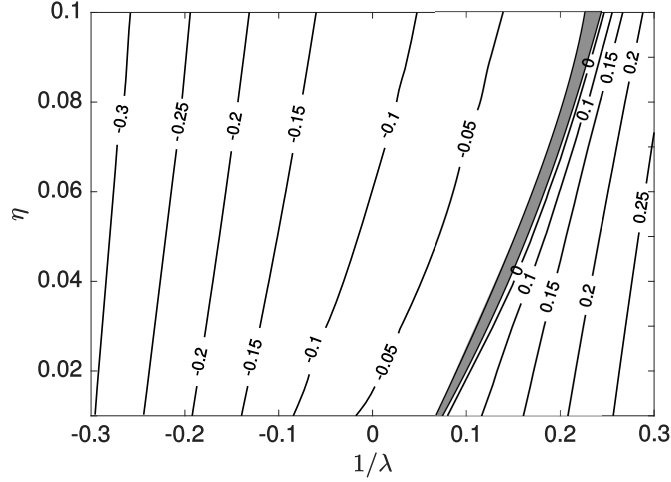


Figure 2.37: Contour map of the non-dimensional mass flow rate $M_T/\pi\rho R_{\text{tip}}^3\Omega$. In a vertical rotor, negative values represent a flow from up to down.

for small values of λ and η :

$$\frac{M_T}{\pi\rho R_{\text{tip}}^3\Omega} = \frac{1}{\lambda} \quad (\text{when } \eta \rightarrow 0 \text{ or } \lambda \rightarrow 0), \quad (2.41)$$

On the other hand, the influence of η grows near the transition between VRS and wind turbine regimes. The mass flow rate is also minimum in these regions, where the total induced flow through the rotor disc is cancelled out by the external flow that is oriented in the opposite direction. The critical case where the total mass flow vanishes occurs in the wind turbine region. This transition is associated with a particular wake geometry close to the rotor: the vortices leave the rotor outwards tangentially to the rotor plane (see figure 2.28b $\lambda = 6.1$). For an helicopter, this situation corresponds to what is called the autorotation regime. It is associated with descending helicopters when the rotor turns just by the action of the air passing through, without any engine driving. In Leishman (2006), this regime is defined as the situation where rotor torque cancels. If blade profile losses are neglected, this is produced when the external velocity and the induced velocity across the rotor are cancelled, that is, when $M_T = 0$. In practice, vertical autorotation is found for a rate of descent, V_∞/V_h (see figure 2.35), around -1.9. In our case, rate descent goes from -1.8 at $\eta = 0.01$ to -2.1 at $\eta = 0.1$ along the contour line $M_T = 0$. In real cases, beyond autorotation state, VRS is reached (this transition from windmill-brake regime to VRS was experimentally documented by Quaranta (2017)).

2.5.4 Energy extracted by a wind turbine

The axial interference factor is a well known quantity in the wind turbine community that measures the importance of the deceleration of the flow across the rotor disc. The total velocity flow crossing the rotor disc can be simply calculated as $V_R = V_\infty + V_i$, which is used in momentum theory to calculate the axial interference factor as:

$$a^* = \frac{V_\infty - V_R}{V_\infty} = -\frac{V_i}{V_\infty}. \quad (2.42)$$

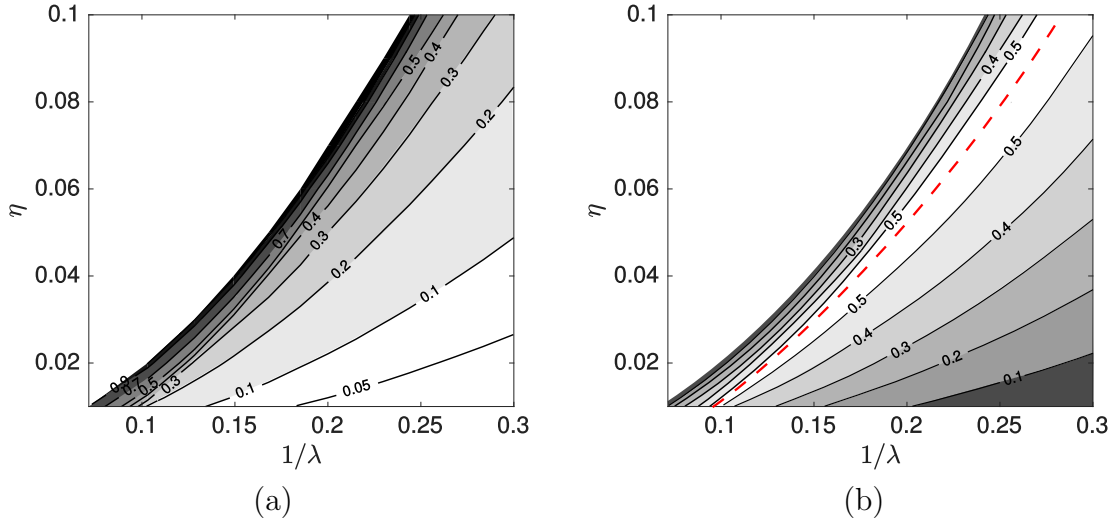


Figure 2.38: Contour maps of (a) axial interference factor a^* and (b) power coefficient C_P . The dashed line corresponds to the contour of $a^* = 1/3$.

In figure 2.38a, the contour map of the interference factor is shown in the $(1/\lambda, \eta)$ plane (in the wind turbine regime). As expected, the interference factor of the rotor is weaker for low values of λ and of η , that is, for high external wind speed and low vortex induction. On the other hand, the axial interference factor grows near the frontier of the wind turbine regime, where the induction effect of the wake is very important compared to the external flow. This feature is directly related with the mass flow rate variation across the rotor (figure 2.37): a high interference factor implies a weak mass flow rate. The limit case $a^* = 1$ matches with the contour line of autorotation at $M_T = 0$.

From the point of view of wind turbine applications, it is specially interesting to estimate the power extracted from the flow by the rotor. In Sørensen (2016), the author proposes an expression derived from the momentum theory to calculate the power extracted by a wind turbine. This expression is obtained from a balance of the energy flux computed upstream and downstream of the rotor:

$$P = 1/2 \rho V_\infty^3 A_0 - \int_{A_1} 1/2 \rho u_1^3 dA_1 - \int_{A_1} \left[1/2 u_{\theta_1}^2 - \int_{r_1}^{R_1} \frac{u_{\theta_1}^2}{r_1} dr_1 \right] \rho u_1 dA_1. \quad (2.43)$$

The two first terms correspond to the axial momentum theory, the last one correspond to the losses due to rotation. A_1 is the cross-section area of the stream tube enveloping the rotor disc in the far-wake, A_0 is the area of the same streamtube upstreams. In our case, u_1 and u_{θ_1} are the azimuthally averaged axial and azimuthal velocities inside this streamtube in the far-wake. The crossareas A_0 and A_1 of the streamtube enveloping the rotor disc are calculated with the relation $uA = \text{Cst}$. In the literature, it is usual to use the power coefficient C_P , defined as:

$$C_P = \frac{P}{1/2 \rho V_\infty^3 A_R} \quad (2.44)$$

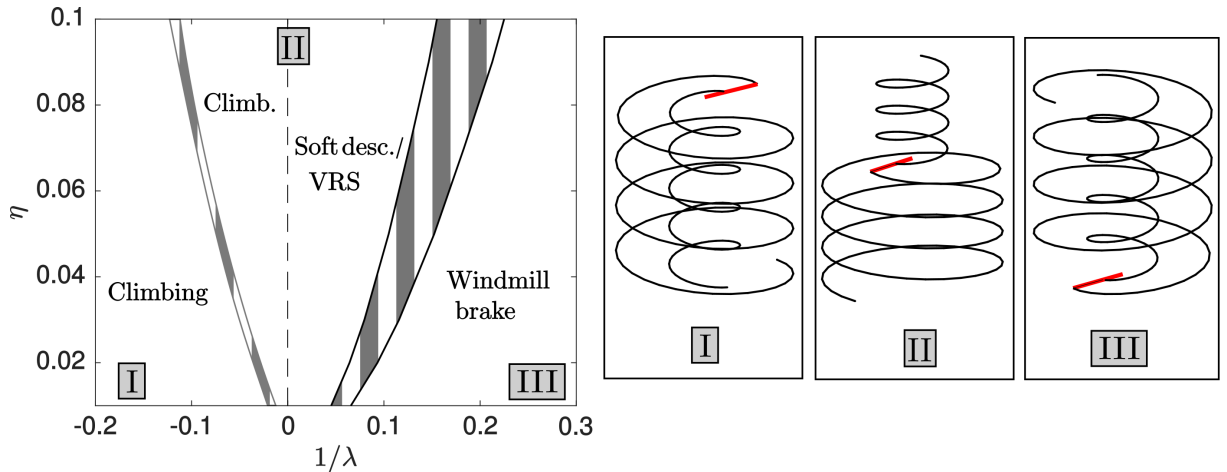


Figure 2.39: Region map in $1/\lambda$ and η of the different solution topologies and rotor regimes. I) Tip and hub vortices go downwards. This kind of solutions are found in climbing flight regime. II) Tip and hub vortices go downwards and upwards respectively. For negative values of λ , climbing flight regime is found, for positive values, soft descending and VRS regimes. Hover flight is found at $1/\lambda = 0$ (dashed line). III) Both vortices go upwards. This kind of solution is found in wind turbine (windmill brake flight) regimes.

In figure 2.38 we show a contour map of the power coefficient of the rotor for different values of λ and η . For the wind turbine regime, we find a maximum value of $C_P = 0.53$, just on the contour line of $a^* = 1/3$. This is in good agreement with the momentum theory, that establishes that the maximum theoretical power coefficient extracted by a wind turbine is $C_P^{\max} = 0.59$ for an axial interference factor of $a^* = 1/3$ (Sørensen, 2016).

2.6 $R_b^* \neq 0$ case (Generalized Joukowski model)

2.6.1 Topology of the solutions

When the hub vortex is not placed on the axis, the complexity of the wake structure is increased. In this case, three different geometries of solutions can be obtained when λ and η are varied. As it was analyzed for $R_b = 0$, the tip-speed-ratio λ gives a characterization of the external flow: it goes downwards for negative values (climbing flight) and upwards for positive values (descending flight), vanishing when $\lambda = \pm\infty$ (hovering). For $R_b \neq 0$, when the external flow is strong, tip and hub vortices are advected downwards, if $\lambda < 0$, or upwards, if $\lambda > 0$. However, for weak external flow, that is, for soft climbing or descending flight, the geometry of the solution changes: external and internal vortices go downwards and upwards respectively. In figure 2.39, a map in λ and η of the regions where the three different solutions are obtained is shown with their respective geometries. Solutions I and III appear exclusively in climbing flight and windmill-brake descending/wind turbine regimes. Solutions II, where each vortex goes in a different direction, are obtained for climbing flight, hovering, soft descending flight and VRS.

2.6.2 Parametrical analysis

In this section, the effect of the tip-speed ratio λ , the vortex strength η , the radii ratio R^* and the number of blades n on the geometry of the wake is analyzed for the three types of solutions.

In figure 2.40, the radial trajectories of the vortices in the wake are shown for the three type of solutions when λ , η and n are varied. For climbing type I solutions, the wake is contracted downwards for tip and hub vortices. This contraction grows when the external flow is reduced or the circulation is increased. Not a big variation is noticed when the number of blades is increased, just a slightly higher contraction for the tip vortex, while the hub vortex remains practically unchanged. A particular modification of the radial trajectory of the internal vortex is observed for high values of λ or η . A small expansion is observed near the rotor, followed by an important contraction to the far-wake state. This occurs when the transition limit to region II is approached (a particular analysis will be addressed later about this point). For type II solutions, similar geometries of the wake are observed independently of the rotor regime. Climbing ($\lambda = -100$), hovering ($\lambda = \infty$) and soft descending ($\lambda = 200$) configurations are very similar. The same contraction of type I solutions is observed for tip vortices. This contraction grows from climbing flight to hovering and it continues to grow in the soft descending regime (just like for $R_b = 0$ case). In hover, the radial trajectory of the tip vortex is almost unchanged when vortex circulation or the number of blades is modified. The hub vortex trajectory is however highly deformed for this type of solution. Firstly, it gets contracted while it goes downwards, then, it goes upwards in the form of a perfect helix. The radius of the far-wake hub vortex is not very sensitive to the variation of λ , however, it noticeably increases with η . For type III solutions, typical wind turbine wake geometries are obtained. A radial expansion is observed for both vortices, especially the external one. This expansion increases with the tip speed ratio, the vortex circulation or the number of blades.

In figure 2.41, the local pitch distribution of the helical vortices is shown for the same cases as figure 2.40. The local pitch is defined for each vortex as

$$h(\phi) = z(\phi + 2\pi) - z(\phi), \quad (2.45)$$

where $z(\phi)$ is the axial location of the helix at its azimuthal position ϕ . For climbing type I solutions, the pitch remains almost constant for both vortices, with a soft increase just after the emission from the rotor. For a single bladed rotor, the pitch is always bigger for the tip vortex, however, an opposed behaviour is observed for 2 or 3 blades. When the external flow is decreased, the wake is decelerated and the pitch is reduced, in the other hand, when vortex circulation is increased, the wake is accelerated and the pitch grows. The inverse behaviour of climbing flight is observed for wind turbine type III solutions. The pitch is softly reduced after the emission from the rotor and it is larger for the hub vortex in single bladed rotors. When λ is increased, the pitch is reduced, as observed in climbing flight, however, in wind turbine configuration, when η is increased the wake is decelerated and the pitch is reduced. For type II solutions, the same tendency as in climbing flight is observed for the tip vortex when λ , η or n are modified. For the hub vortex, a completely different evolution is observed. A strong variation is observed when the vortex changes direction and goes upwards, then, the pitch becomes constant.

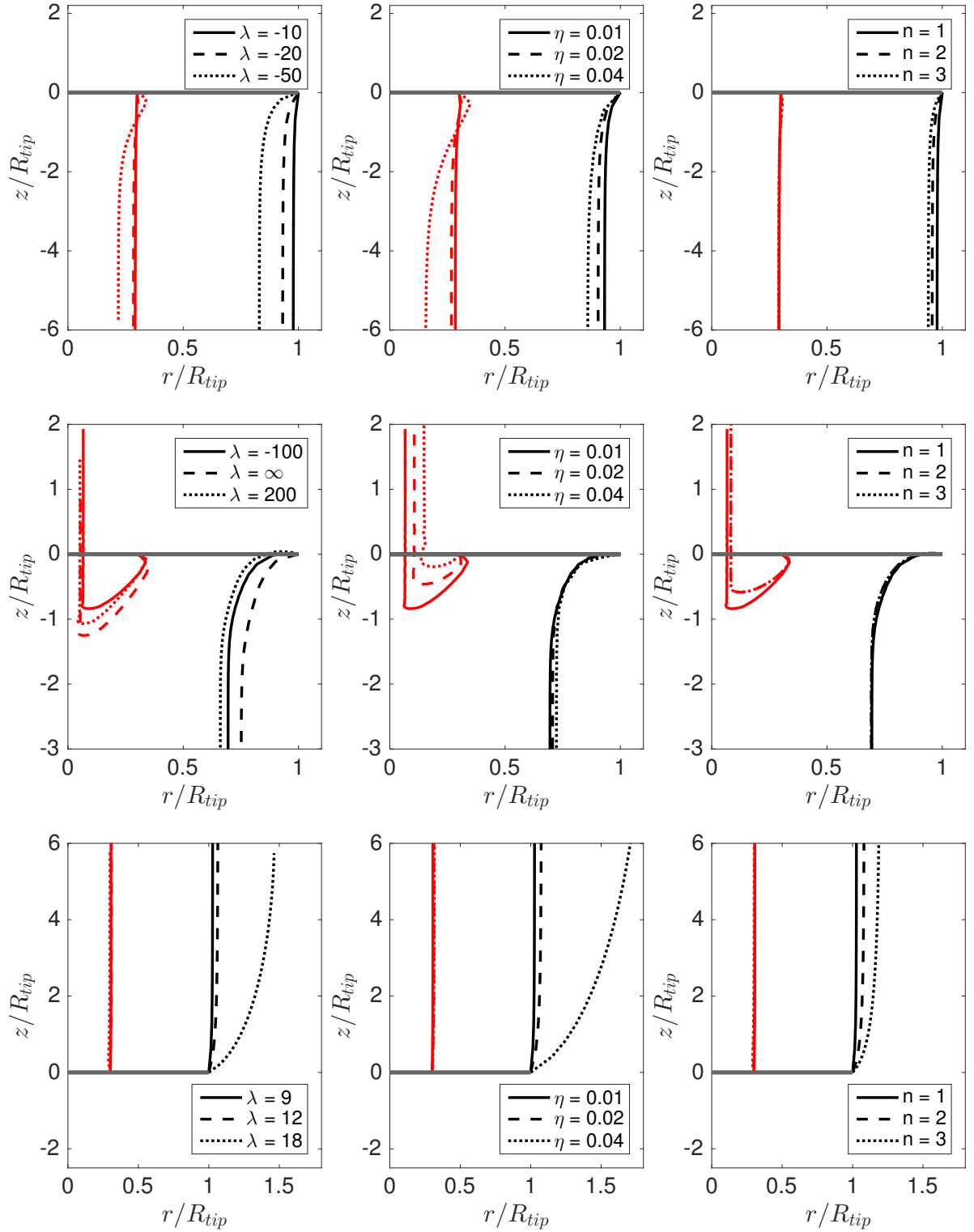


Figure 2.40: Radial trajectories of tip (black) and hub (red) vortices along the wake for different values of λ , η and n . The default parameters are $\eta = 0.01$, $n = 1$ and $\lambda = -20$ for region I solutions (upper line), $\lambda = \infty$ for region II (middle line) and $\lambda = 12$ for region III (lower line). For all the cases $R_b^* = 0.3$ and $\varepsilon = 0.05$. The horizontal thick grey line represents the rotor disc.

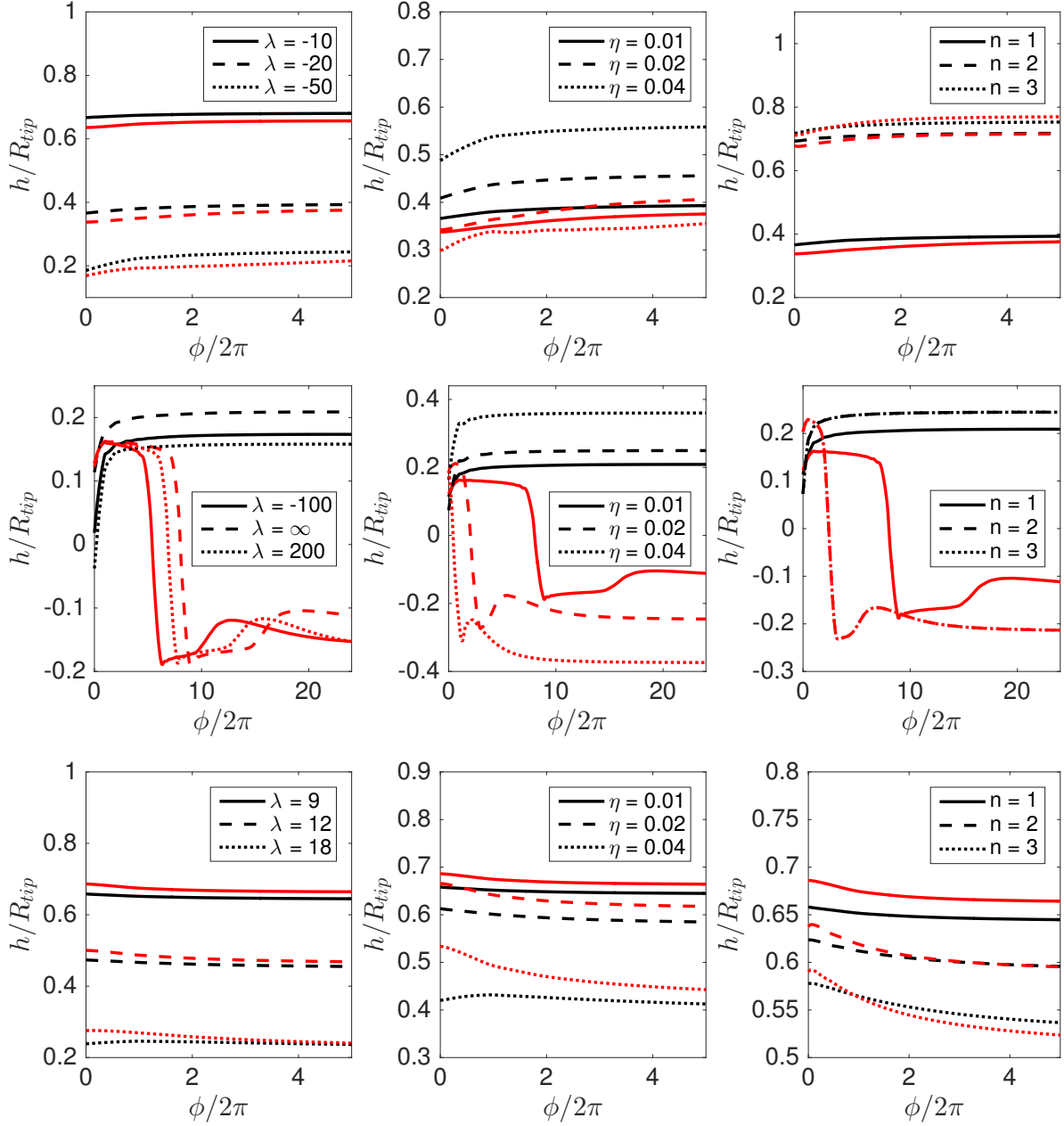


Figure 2.41: Local pitch distribution of tip (black) and hub (red) vortices in the wake along the azimuthal position ϕ of each vortex for different values of λ , η and n . The distributions of the figures and the chosen parameters are the same as in figure 2.40.

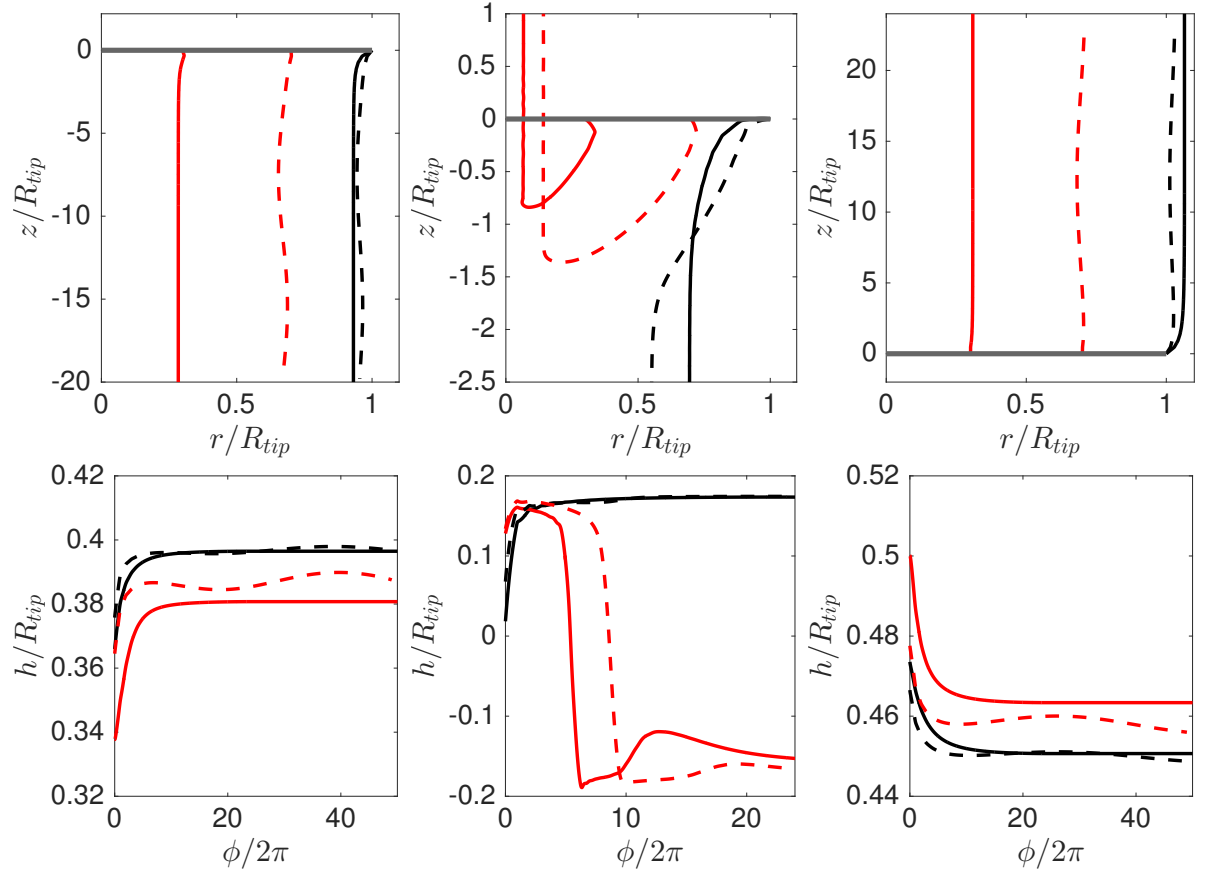


Figure 2.42: Radial trajectories (upper plots) and local pitch distribution (lower plots) of tip (black) and hub (red) vortices in the wake for two different values of radii ratio: $R_b^* = 0.3$ (solid line) and $R_b^* = 0.7$ (dashed line). The tip-speed-ratio is $\lambda = -20$ for left plots (climbing flight, region I), $\lambda = \infty$ for middle plots (hover, region II) and $\lambda = 12$ for right plots (windmill brake flight, region III). For all the cases $\eta = 0.01$, $n = 1$ and $\varepsilon = 0.05$.

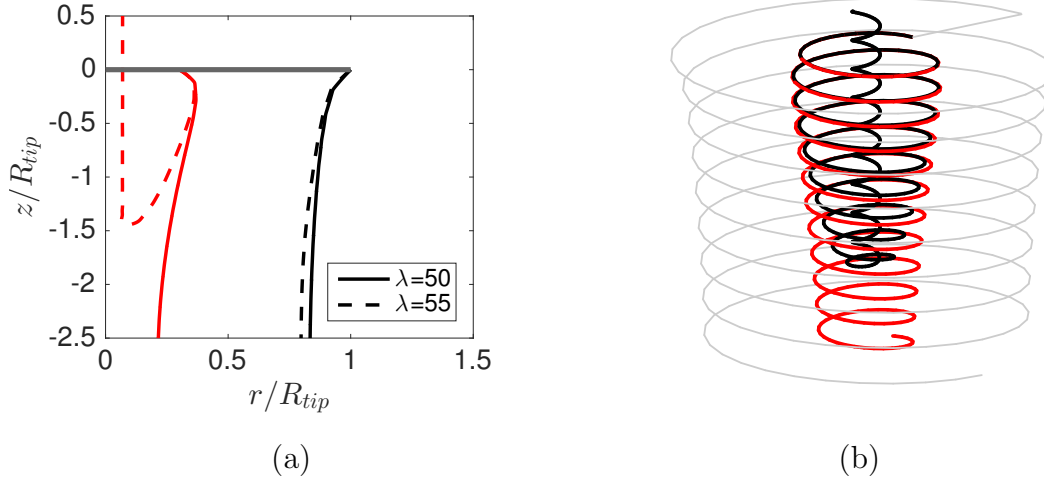


Figure 2.43: Transition in climbing flight regime from type I solutions ($\lambda = 50$) to type II solutions ($\lambda = 55$), with $\eta = 0.01$, $R_b^* = 0.3$ and $\varepsilon = 0.05$. (a) Radial trajectories of tip (black) and hub (red) vortices. For the tip vortex, the transition is very smooth, in both cases the vortex goes downwards and the geometry is conserved. The hub vortex goes downwards for $\lambda = 50$ and upwards for $\lambda = 55$; a overlap of both geometries can however be observed near the rotor disc. This similar behaviour can also be noticed in the perspective view in figure (b). For a better visualization, just the tip vortex for $\lambda = 50$ is shown in light grey line.

In figure 2.42, the effect of the parameter R_b^* is illustrated. Radial trajectories and local pitch distribution for the three different kinds of solutions are shown for $R_b^* = 0.3$ and $R_b^* = 0.7$. In climbing flight and wind turbine configurations, when R_b^* is increased, tip and hub vortices approach and the mutual interaction becomes more important. In figure 2.42 (left and right plots) it can be perfectly noticed in the far-wake the periodical deformation studied in section 2.3. For $R_b^* = 0.3$, the radial interaction of both vortices is very weak and the helices remain undeformed. For the type II solutions, the effect of R_b^* is clearly visible near the rotor. When the hub vortex goes downwards, it influences the contraction of the tip vortex structure: this contraction is weaker close to the rotor but larger in the far-wake. An opposite behaviour is observed for the hub vortex: the far-wake contraction is reduced. The pitch of the external helix remains unchanged. For the hub vortex, the pitch distribution is altered near the rotor when R_b^* is modified, but it reaches a similar value in the far-wake.

In figure 2.40, it is interesting to note the similar behaviour of tip vortex solutions in regions I and II. In both cases, the tip vortex moves downwards with similar radial trajectories and pitch distribution. In figure 2.43, the transition between both regions is illustrated for a climbing flight regime example. For the tip vortex, there is no difference on the geometry when the frontier of the existence domain is reached from both sides and solutions seem to match perfectly. For the hub vortex, solutions are completely different in the far wake, as it goes downwards for region I and upwards for region II. However, near the rotor, a long as both solutions go downwards, they overlap.

In figure 2.44, the contour maps of the far-wake parameters h^* and α are shown in the

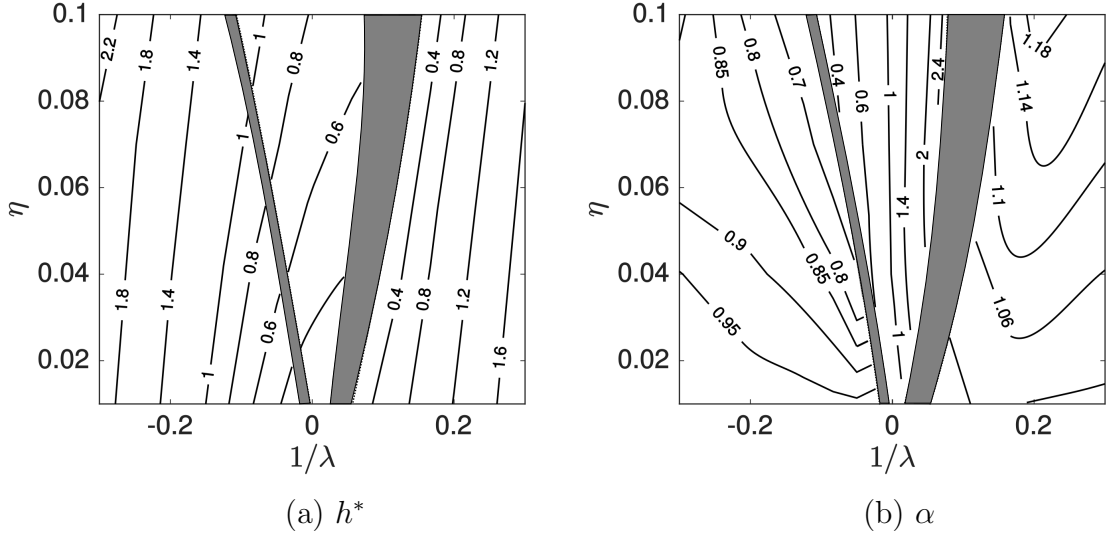


Figure 2.44: Contour maps of the far-wake parameters h^* and α in the $(1/\lambda, \eta)$ with $R_b^* = 0.3$ and $\varepsilon = 0.05$. In grey, regions where no solution has been obtained.

$(1/\lambda, \eta)$ plane. From the contours of h^* , one can notice the continuity of the tip vortex solution across the frontier between regions I and II. However, for wind turbine regimes, the geometry completely changes. Generally, h^* grows for small values of λ , that is, when the external flow is strong, and decreases for slow windmill brake descending and "fast" soft descending, where VRS are expected. Concerning α , we first observe that its range of variation is limited in region I and III. As it was observed in figure 2.40, α is always smaller than 1 for climbing flight regime (region I), that is, the hub vortex has a smaller pitch than the tip vortex. For the wind turbine regime (region III), α is always bigger than one. For both cases, α approaches 1 when η is reduced. For type II solutions, the definition of h^* and α is not strictly the same as presented in section 2.3, in this case, each vortex goes in a different direction and they never interact in the far wake. However, the same logic of the rest of regions is conserved: $\alpha < 1$ for climbing flight and $\alpha > 1$ for descending flight, obtaining $\alpha \simeq 1$ at hovering flight independently of the value of η .

2.6.3 Comparison with the standard model

Almost no difference is found between tip vortex solutions obtained with standard and generalized Joukowski models. In figure 2.45a, a 3D view of a wake is shown for a hovering flight regime obtained with both models. Both solutions are almost identical, with a slight radii difference at the far wake. In figure 2.45b, a contour map of the non-dimensional pitch h^* is plotted in the $(1/\lambda, \eta)$ plane. A very good overlap of the models is noticed for all the regimes. Just a small variation is observed in the VRS region. In this figure, it can also be noticed that more extreme solutions can be found with the standard model. It can be expected that the agreement between both models disappears if high values of R_b^* parameter are considered, especially for VRS regimes, where vortices are greatly deformed due to their mutual interaction (figure 2.42). In figure 2.46, radius and pitch of the external helix at the far-wake are compared for different rotor regimes with several values of parameter R_b^* . One can note that the pitch is the same for both standard and generalized models independently of the regime or the radii ratio R_b^* . However, a visible variation of the tip vortex radius in the far-wake is observed when high values of R_b^* are chosen, specially in VRS cases. For $R_b^* < 0.5$, the difference of the far-wake radius remains small, even in VRS. Only for $R_b^* = 0.7$, a deviation of about 25% is found in VRS. Similar tendencies are observed for different values of vortex strength η .

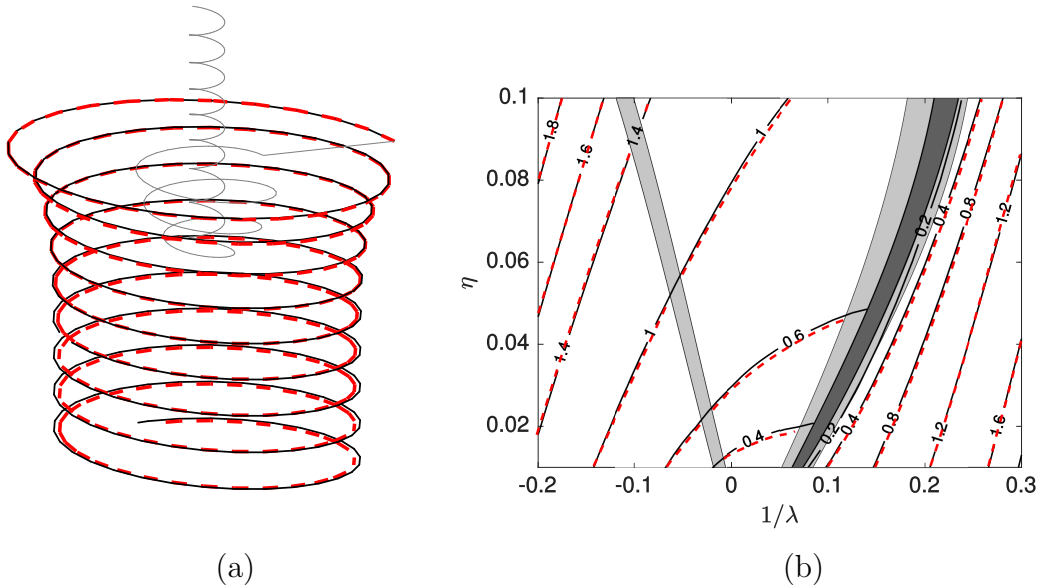


Figure 2.45: (a) Perspective of the wake for $\lambda = \infty$ and $\eta = 0.04$ (To simplify the visualization, just the vortices of a single blade are plotted). (b) Contour map of h^* . In black solid line: standart Joukowski model ($R_b^* = 0$). In red dashed line: the generalized Joukowski model ($R_b^* = 0.3$). For both cases $\varepsilon = 0.01$ and $N = 2$.

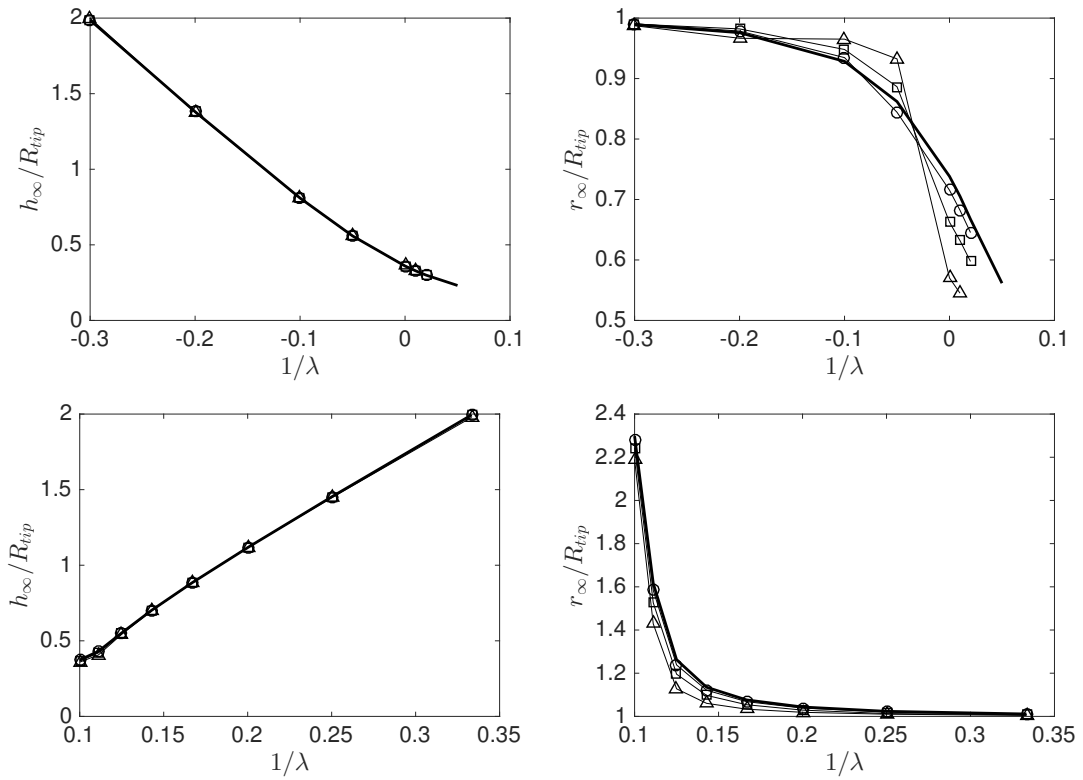


Figure 2.46: Pitch and radius of the tip vortex at the far-wake for climbing flight and VRS (upper plots) and wind turbine regimes (lower plots). Comparison between standart Joukowski solutions (solid line) and generalized model solutions for $R_b^* = 0.3$ (\circ), $R_b^* = 0.5$ (\square) and $R_b^* = 0.7$ (\triangle). $\eta = 0.02$ and $\varepsilon = 0.01$.

2.7 Chapter conclusion

In this chapter, the geometry of the wake behind a rotor has been studied. A Joukowski model has been used for the wake, composed of a bound vortex on the blade and two free vortices emitted from the tip and hub. Solutions are presented for a standard model, where the hub vortex is straight and placed on the axis, and a generalized model, where hub vortex is out of axis, generating a helical vortex.

Near- and far-wake structures have been studied separately. Far-wake solutions have been modeled as infinite structures of coaxial helical vortex pairs. These solutions have been proved to be spatially periodic and stationary in an appropriate moving reference frame. An extensive parametric analysis has been made for this kind of solutions. For the standard case, far-wake solutions are uniform helical vortices with a straight vortex on the axis.

Near-wake solutions have been obtained for any kind of flight configuration. For the standard case, the induced flow across the rotor has been computed and compared with Momentum theory and experimental measurements; a good agreement has been found for all rotor configurations. For the generalized model, three different topologies of solutions have been found, with two small regions in the climbing flight and VRS regimes, where no solutions have been obtained. This region without solutions at the transition to VRS is also found in the standard configuration. A VRS region without solution is also found with the standard model.

Chapter 3

Stability of the wake

Contents

| | | |
|-----|-------------------------------------|----|
| 3.1 | Chapter overview | 78 |
| 3.2 | Perturbation model | 79 |
| 3.3 | Modal decomposition | 81 |
| 3.4 | Spatio-temporal evolution | 84 |
| 3.5 | Chapter conclusion | 86 |

3.1 Chapter overview

In this chapter, the stability of the solutions obtained for the vortical wake is analyzed, in particular, solutions obtained with the standard Joukowski model.

The stability of a perfect helical vortex was studied by Betchov (1965) and Kida (1982) taking into account the local induction approximation where the velocity on a point of the vortex just depends on the local curvature. However, this simplification is only valid for large pitch helices, where the effect of the successive turns of the helix is small compared to local curvature effects. A stability analysis of the problem taking into account the induction effect of the whole structure was made by Widnall (1972). Widnall calculated the self-induced velocities of a single helix using the Biot-Savart law with the cut-off method. She then calculated analytically the displacement of the perturbations and identifying unstable modes at different wavelengths. The modes of instability found by Betchov (1965) or Kida (1982) were completed with new modes for small pitch, where the effect of interaction of successive turns of the helix is important. It was also found how the most unstable perturbation appears when the displacement of the neighboring loops are out of phase. Some years later, Fukumoto & Miyazaki (1991) included an axial flow along the vortex core, finding that the instability may be suppressed for some cases with large pitch. Gupta & Loewy (1974) extended the results of Widnall for multiple interdigitated helices following the same principle of Biot-Savart integration and cut-off formula and obtaining the growth rates of the different unstable modes. In the case of multiple helical vortices, different instability modes appear from the mutual interaction of the different helices. Similar to the single helix case, the most unstable modes for two interlaced helices exhibit an out-of-phase symmetry pairing. Okulov (2004) reconsidered the case of multiple helices using not the Biot-Savart integration but analytic expressions for the induced velocity introduced by Hardin (1982). Later, Okulov & Sorensen (2007) added the central vortex present in Joukowski model. Concurrently, similar stability analysis have been made for an infinite array of vortex rings (Levy & Forsdyke, 1927; Bolnot *et al.*, 2014), which presents important similarities with helices of small pitch.

A number of authors have worked on these stability problems using numerical simulations and experimental studies of rotor wakes. Ivanell *et al.* (2010) and Sarmast *et al.* (2014) studied numerically the instability of the wake in wind turbines, using the actuator line method (Sorensen & Shen, 2002) to model the rotor. In these works, the authors calculated the spatial growth rate of the individual modes through a spectral analysis of the non-linear flow. A temporal linear stability analysis was recently performed by Brynjell-Rahkola & Henningson (2017) and Selçuk *et al.* (2018), obtaining the growth rate of different unstable modes using time-stepping methods on the linearised Navier-Stokes equations. On the experimental side, Quaranta *et al.* (2015) did a complete comparison with Widnall (1972) results, reproducing the main unstable modes with their growth rates. They also explained why the instability mechanism is associated with local pairing. In a more recent work, Quaranta *et al.* (2018) presented a similar analysis for two interlaced helical vortices and captured the unstable pairing modes predicted by Gupta & Loewy (1974).

In this chapter, a temporal linear stability analysis of our solutions will be performed. In section 3.2, the methodology to perturb the solutions and analyze the evolution of the perturbation in time will be presented. In section 3.3, the evolution of the perturbation

will be processed to obtain the growth rate as a function of wave number. In section 3.4, spatio-temporal analysis of the perturbation will be performed, studying how they propagate in the wake. Thanks to this analysis, the rotor regimes for which the solution is convectively or absolutely unstable will be identified.

3.2 Perturbation model

To analyze the stability of the solutions calculated in section 2.5, a perturbation is introduced on the stationary wake structure in the rotating local frame:

$$\mathbf{s}(t) = \mathbf{s}_0 + \mathbf{s}'(t), \quad (3.1)$$

where $\mathbf{s}_0 = (r_0(\zeta), \phi_0(\zeta), z_0(\zeta))$ is the base solution and $\mathbf{s}' = (r', \phi', z')$ is the perturbation. Introducing the complete perturbed solution \mathbf{s} on the problem equation (2.37) and linearizing, we obtain a first order system of equations for the temporal evolution (on ψ) of the perturbation:

$$\frac{\partial r'}{\partial \psi} = -\frac{\partial r'}{\partial \zeta} + \frac{1}{\Omega_R} \left[\frac{\partial U_r}{\partial r} r' + \frac{\partial U_r}{\partial \phi} \phi' + \frac{\partial U_r}{\partial z} z' \right], \quad (3.2)$$

$$\frac{\partial \phi'}{\partial \psi} = -\frac{\partial \phi'}{\partial \zeta} + \frac{1}{\Omega_R} \left[\frac{\partial \Omega}{\partial r} r' + \frac{\partial \Omega}{\partial \phi} \phi' + \frac{\partial \Omega}{\partial z} z' \right], \quad (3.3)$$

$$\frac{\partial z'}{\partial \psi} = -\frac{\partial z'}{\partial \zeta} + \frac{1}{\Omega_R} \left[\frac{\partial U_z}{\partial r} r' + \frac{\partial U_z}{\partial \phi} \phi' + \frac{\partial U_z}{\partial z} z' \right]. \quad (3.4)$$

The system is solved numerically. For that, a finite difference discretization scheme has been applied in ψ and ζ :

$$\frac{\mathbf{s}'_{j+1} - \mathbf{s}'_j}{\Delta \psi} = \left[-D_\zeta + \frac{1}{\Omega_R} \nabla \mathbf{U}(\mathbf{s}_0) \right] \mathbf{s}'_j \quad (3.5)$$

where the index j represents the discretized position in ψ , D_ζ is the discretization matrix on ζ and $\nabla \mathbf{U}(\mathbf{s}_0)$ is the Jacobian matrix of the complete induced velocity field on the base solution. To avoid numerical stability problems, a robust discretization scheme has to be chosen for the matrix D_ζ . In our case, a five point symmetric discretization scheme has been used.

The perturbation is introduced as an impulsion displacement in the axial direction at the azimuthal position ζ_p :

$$\mathbf{s}'_{j=0}(\zeta) = \begin{pmatrix} 0 \\ 0 \\ A_p \delta(\zeta - \zeta_p) \end{pmatrix}, \quad (3.6)$$

where A_p is the amplitude of the initial perturbation and δ is the Dirac delta function. The perturbation is applied for each vortex in the same axial position, so symmetry is forced.

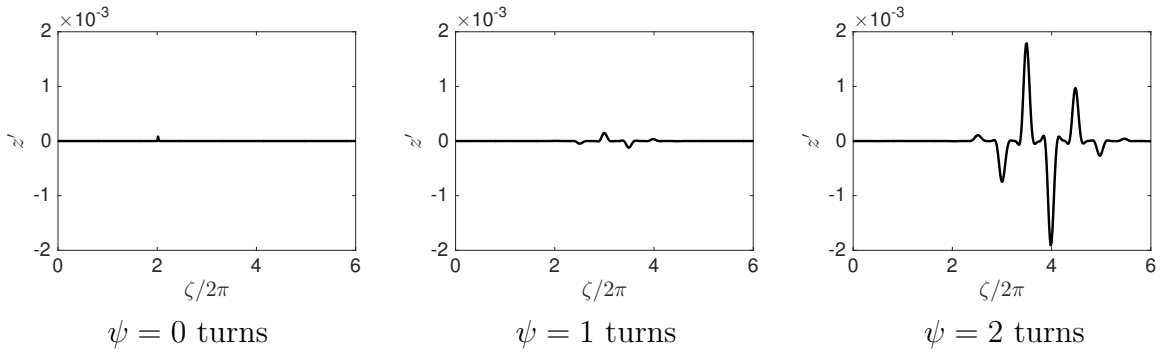


Figure 3.1: Axial coordinate of the perturbation at three different instants. Parameters of the base solutions are $\lambda = -10$, $\eta = 0.04$, $\varepsilon = 0.05$. Perturbation amplitude and initial position $A_p = 10^{-4}R_{\text{tip}}$ and $\zeta_p = 4\pi$.

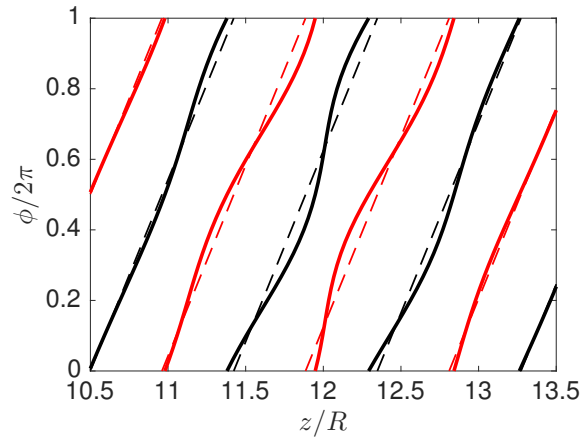


Figure 3.2: View of the perturbed helical vortex in the axial-azimuthal plane. Solid line: perturbed solution. Dashed line: base solution. The same parameters of figure 3.1 are used for the base solution. The system is dominated by the pairing instability.

In figure 3.1, the evolution of an axial perturbation on a climbing flight wake is shown. In this case, the perturbation is introduced at $\zeta_p = 4\pi$, however, for climbing flight, similar propagations are normally found independently of the initial position of impulse forcing. As soon as it is created, the perturbation propagates downstream and starts to interact with the surrounding turns of the helices. This interaction produces new peaks in the perturbed signal. Unstable solutions are found for all rotor regimes. The perturbation is always amplified in time and the system is dominated by a pairing instability mode. In figure 3.2, a view of the perturbed solution in the axial-azimuthal axis is shown where the pairing pattern can be perfectly seen.



Figure 3.3: Schematic of the deviation d of the perturbed solution. (a) Unperturbed and (b) perturbed system.

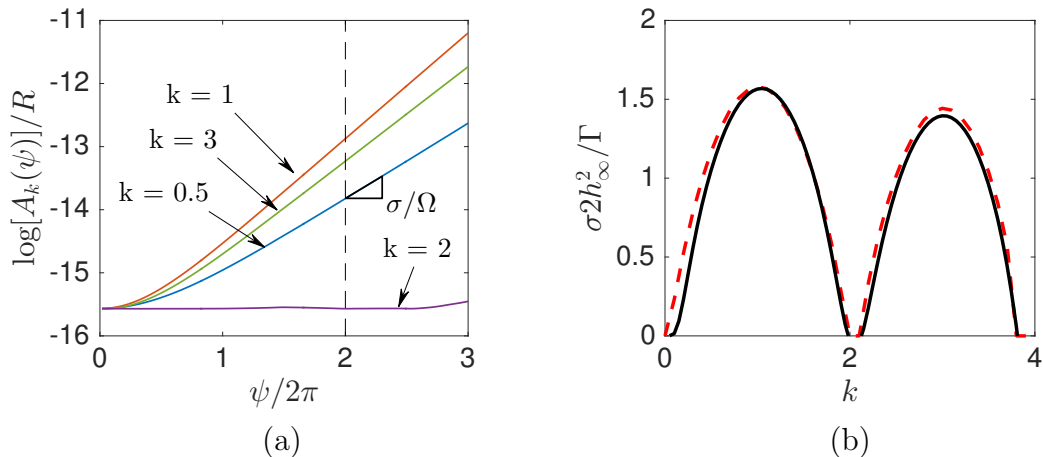


Figure 3.4: (a) Temporal evolution of the perturbation decomposed for different wavenumbers. In dashed line, the position in time where the slope is measured to obtain the growth rate. (b) Growth rate as a function of the wave number. Solid line: distribution for a wake solution with $\lambda = -10$, $\eta = 0.04$, $\varepsilon = 0.05$ and $\zeta_p = 4\pi$. Dashed line: theoretical prediction for $h/R = 1.03$ and $a/R = 0.055$, obtained from the geometrical parameters of the solution in the far-wake.

3.3 Modal decomposition

The particularity of introducing a Dirac perturbation is that all the wavenumbers are excited and they grow together in a wave packet. A spectral analysis is made to separate and find the growth rate of each wavenumber. Instead of analyzing the perturbation in a particular frame, we first consider the total deviation d of the vortex from its unperturbed position (figure 3.3). To have a equispaced discretization of the vortices in the azimuthal direction, original solution in ζ is interpolated and parametrized in terms of the azimuthal coordinate ϕ .

At each time step, spatial Fourier transform is applied to the deviation function $d(\phi)$ in order to obtain the amplitude of different modes. For each mode, associated with a wavenumber k , the temporal evolution of the amplitude $A_k(\psi)$ is obtained (figure 3.4a). After a transient, the amplitude evolution can be fitted by an exponential expression $A_k(\psi) \sim \exp(\sigma\psi)$, where σ is the growth rate of the instability mode of wavenumber k .

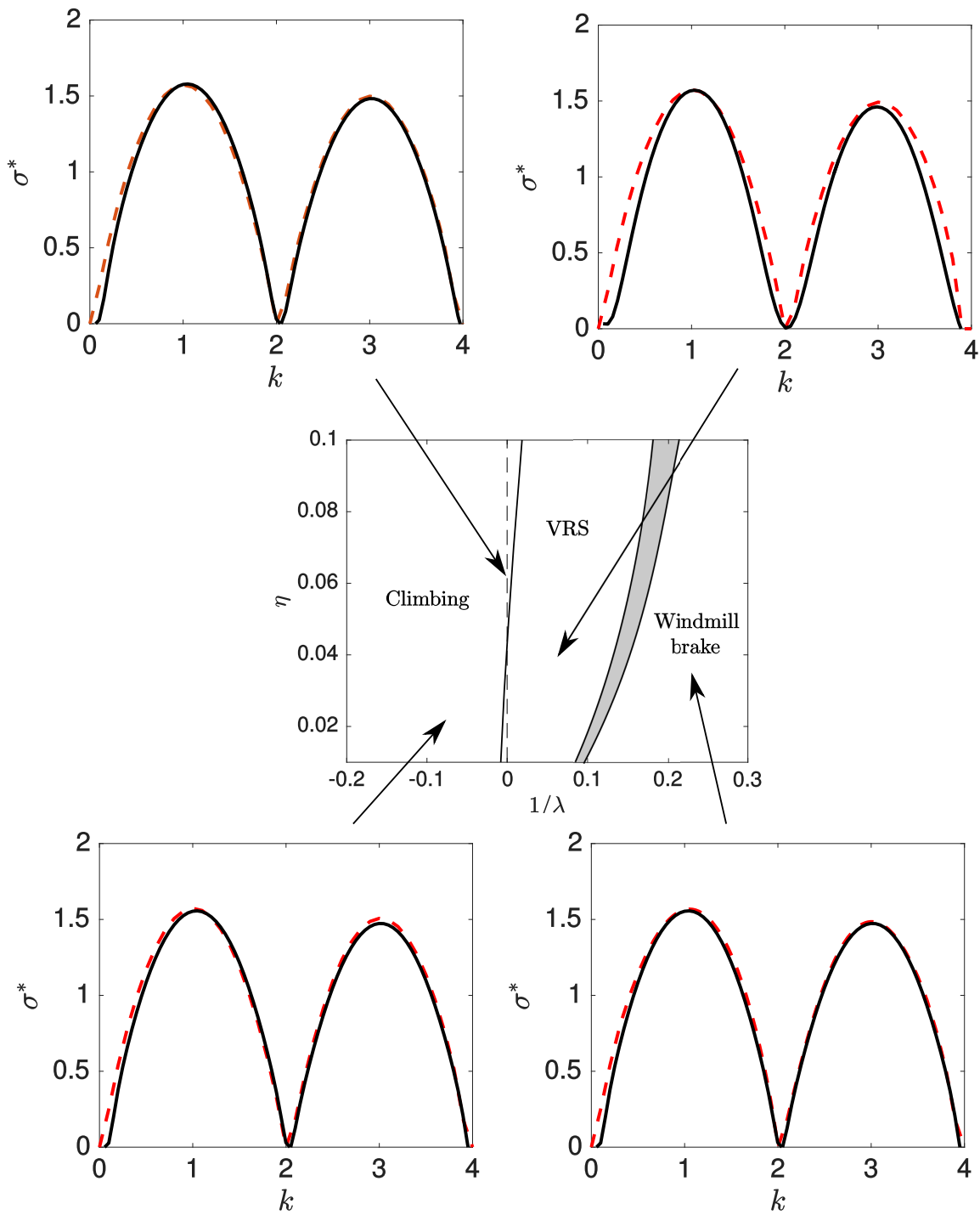


Figure 3.5: Growth rate distribution for different rotor regimes with $\varepsilon = 0.01$ and $\zeta_p = 20\pi$ for all cases. Solid line: numerical analysis of the perturbed solutions. Dashed line: theoretical prediction from Gupta & Loewy (1974).

Then, it can be calculated as:

$$\sigma(k) = \frac{d}{d\psi} \log [A_k(\psi)] \quad (3.7)$$

In figure 3.4a, the temporal evolution of the perturbation associated with different wave numbers is plotted. To obtain the growth rate, the slope of the perturbation is measured after 2 turns of rotor ($\psi = 4\pi$), when the exponential growth is established.

In figure 3.4b we show a typical distribution of the growth rate as a function of the wavenumber. We plot the non-dimensional growth rate σ^* , defined as:

$$\sigma^* = \text{Re}(\sigma)2h_\infty^2/\Gamma \quad (3.8)$$

It can be observed the more unstable mode at $k = 1$ with a value of $\sigma^* \simeq \pi/2$, which corresponds to the local pairing mode shown in figure 1.15b. Successive highly unstable modes are found for odd wavenumbers. A comparison is made with the analytical results obtained by Gupta & Loewy (1974) for infinite multiple helical vortices. The theoretical curve for $\sigma(k)$ is calculated by taking $h/R = h_{FW}/R_{FW}$ and $a/R = a/R_{FW}$ as parameters for the infinite helix.

In their work, Gupta & Loewy (1974) used the same procedure as that of Widnall (1972). On a perfect helix that rotates and axially translates without changing shape due to its self-induction, they consider perturbations of the form:

$$\delta\mathbf{r}_h = \delta\hat{\mathbf{r}}_h \exp(\sigma t + ik\theta_h), \quad (3.9)$$

where $\delta\mathbf{r}_h$ is the perturbation in a cylindrical frame, $\delta\hat{\mathbf{r}}_h$ is the amplitude of the perturbation in the three directions and θ_h is the azimuthal coordinate of the helix. The evolution of the filament shape is obtained by computing its self-induced velocity from the Biot-Savart law. To desingularize the integral, contrary to Widnall (1972), who used a cut-off method, Gupta & Loewy (1974) used a Rosenhead formula (Saffman, 1992), that replaces the denominator of Biot-Savart integral by $|(\mathbf{r} - \mathbf{r}_0)^2 + \mu^2|^3$, where μ is a parameter proportional to the core size. This procedure is equivalent to cut-off for $\mu = a \exp(-3/4)$ (Saffman, 1992). However, Gupta & Loewy (1974) erroneously used $\mu = a$, so a correction has to be made to compare with their results. Independently of the desingularization procedure, the main difference with Widnall (1972) is that they extended the analysis to multiple helical vortices.

In the theory, different growth rate distributions are obtained when pitch or core size are modified, consequently, the growth rate will be also modified when the rotor regime is changed and the wake structure varies. In figure 3.5, examples of the growth rate distribution are presented for different rotor regimes. For all cases, the same distribution can be observed, with most unstable modes located at $k = 1$ and $k = 3$. A good agreement is found with the theoretical prediction independently of the regime.

It is important to note that, for this modal analysis, the perturbation has to be introduced where the wake structure is already uniform. Near the rotor, the spatial distribution of the vortex is not uniform and the dynamic of the perturbation is not clear, so exponential growth is not necessarily expected. Here, we have therefore mainly computed the stability properties of the far-wake, which is well described by perfect helices. This explains the very good agreement with Gupta & Loewy (1974) that we have observed even for the non-conventional VRS regime.

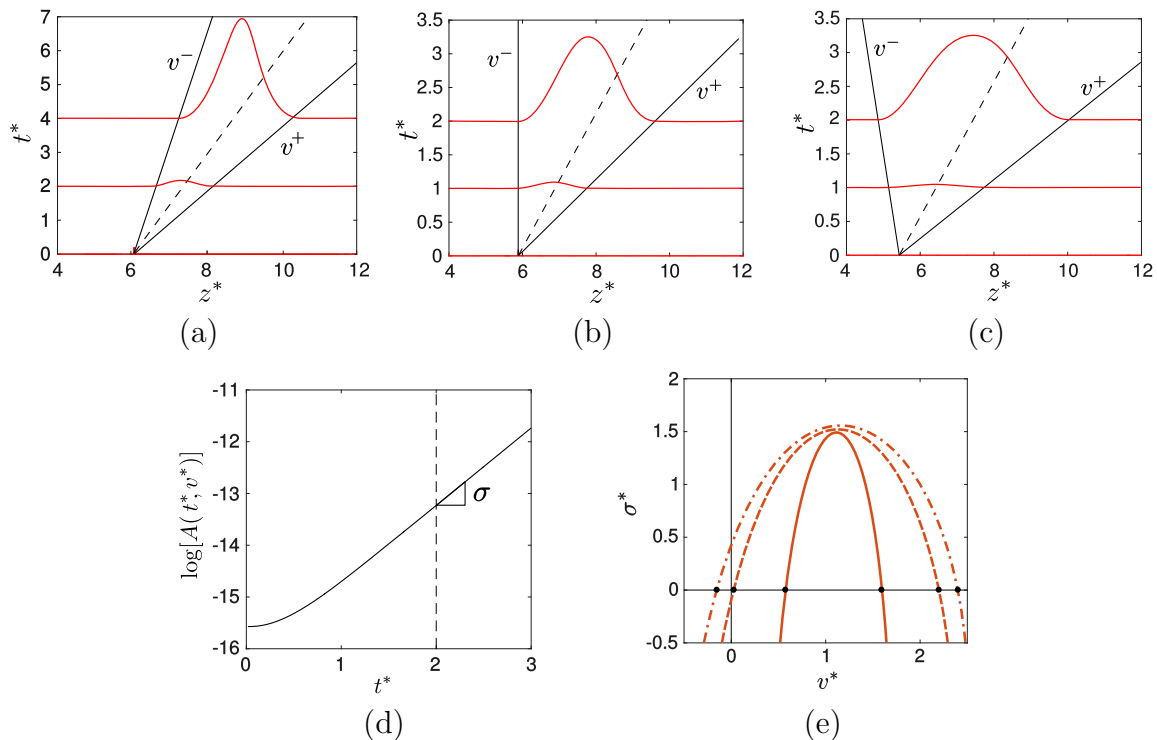


Figure 3.6: Spatio-temporal evolution of the perturbation for (a) a convectively unstable case ($\lambda = -50$), (c) an absolutely unstable case ($\lambda = 20$) and (b) a case on the convective/absolute limit ($\lambda = -600$). For the three cases, the perturbation is introduced at 6 turns of the helix from the rotor. (d) Typical temporal evolution of the amplitude of the perturbation at a frame velocity v^* . (e) Growth rate versus frame velocity for the three cases of upper figures: $\lambda = -50$ (solid), $\lambda = -600$ (dashed), $\lambda = 20$ (dash-dotted).

3.4 Spatio-temporal evolution

To analyze the spatio-temporal development of the perturbations, the domain of simulation is fixed to 30 turns, plus 25 turns in the far wake domain. The idea is to have a long domain of simulation to analyze the temporal evolution before boundary effects appear when the perturbation reaches the frontier of the domain. In practice, to avoid this effect, the simulation is stopped before the perturbation has reached half of the length of the domain. The simulation is started with a localized initial condition in the form of a Dirac impulse, as in previous section. The size of the initial perturbation is fixed at $10^{-4}R$ in the axial direction (similar results were obtained applying it in azimuthal and radial directions). The initial location of the perturbation ζ_p is fixed at 6 turns from the rotor plane. If the perturbation is introduced after the the point where the wake structure becomes uniform, similar evolutions of the perturbations are observed. Similarly as for the modal analysis, spatio-temporal stability will be analyzed in the far wake. Near the rotor, the dynamic of the perturbation is not clear. Note that, even if the far-wake is only convectively unstable, nothing prevents the near-wake to be absolutely unstable. We will not study these cases here.

From now, the spatio-temporal evolution of the wavepacket will be analyzed in the

axial direction z , which is related to coordinate ζ by:

$$\frac{dz}{d\zeta} = \frac{1}{\Omega_R} (U_z^{\text{ind}} + V_\infty). \quad (3.10)$$

In figure 3.6a-c, temporal evolution of the wavepacket is plotted. The axial direction and time are normalized as:

$$z^* = \frac{\Omega_R/2\pi}{N\Gamma/2h_\infty + V_\infty} z, \quad t^* = \frac{\Omega_R}{2\pi} t. \quad (3.11)$$

Note that normalized time is equivalent to rotor azimuth ψ . If we move in the wake with the wavepacket, we will see how the amplitude of the perturbed solution grows in time. Then, following the same procedure as for the modal analysis, the growth rate can be calculated by measuring the slope of the amplitude evolution (figure 3.4a). This procedure can be used for any frame velocity $v = z/t$, obtaining a particular amplitude evolution $A(t, v)$ and its related growth rate $\sigma(v)$ (figure 3.6d). Then, downstream v_+ and upstream v_- propagation velocities are calculated as the values of v where the growth rate is zero, that is, where the perturbation is no longer amplified. Transition from convective to absolutely unstable is found when $v_- = 0$ (figure 3.6b).

In figure 3.6e, $\sigma^*(v^*)$ distribution is plotted for the three regimes of the figure. v^* is the frame velocity normalized as

$$v^* = \frac{v}{N\Gamma/2h_\infty + V_\infty}. \quad (3.12)$$

Under this normalization, the maximum growth rate values are found at $v^* = 1.103$, $v^* = 1.111$ and $v^* = 1.145$ for $\lambda = -50$, $\lambda = -600$ and $\lambda = 20$ respectively, which correspond to the velocity of displacement of the vortices. This velocity does not coincide with $v^* = 1$ because the axial induced velocity of the helices is not exactly $\Gamma/2h_\infty$, as in the two-dimensional case of an array of vortices. For the three cases, the maximum growth rate is closed to $\sigma^* \simeq \pi/2$, and it corresponds to the contribution of mode $k = 1$, as it was seen in the previous section. A narrower peak of $\sigma^*(v^*)$ corresponds to a slower expansion of the wavepacket. If the expansion is slower than the advection, the system remains convectively unstable, otherwise the system becomes absolutely unstable. In other words, if there are negative values of v^* for positive values of σ^* , the system is absolutely unstable.

Concerning rotor regimes, $\sigma^*(v^*)$ has a narrower peak for high external velocity regimes, and it gets wider when approaching hover and soft descending flights. In figure 3.6, the velocity of expansion of the perturbation is minimal for the climbing flight and it grows when approaching VRS. In figure 3.7, the regions of stability for in the $(1/\lambda, \eta)$ plane are shown. Climbing and windmill brake flight regimes are generally convectively unstable. The transition to absolutely unstable regimes occurs near hovering flight, which is also the region where the transition to VRS is observed. Another transition to absolutely unstable solutions is observed in wind turbine regimes, just before the region where solutions cannot be obtained. This transition occurs around the limit when the wake overtakes the rotor plane and the mass flow across the rotor disc falls to zero. However, for this kind of solution, the wake structure requires a great distance from the rotor to become uniform, so it is not excluded that the impulse has been positioned too close to the rotor in this case.

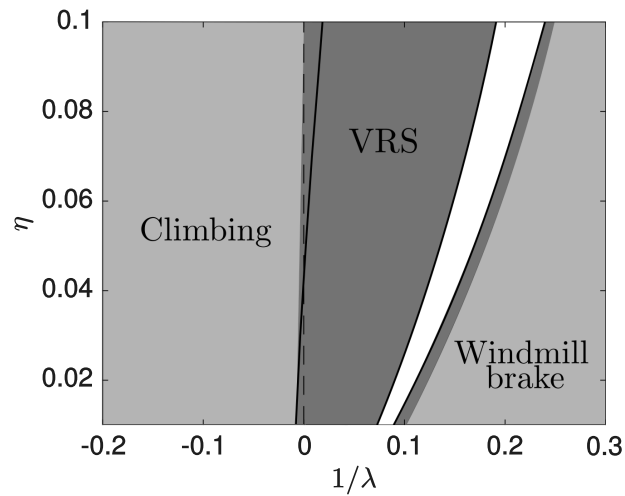


Figure 3.7: Convective (light grey) and absolute (dark grey) instability regions ($\varepsilon = 0.01$).

3.5 Chapter conclusion

An stability analysis of wake solutions obtained in the previous chapter has been addressed. An axial impulse perturbation is introduced in the helical structure to observe its evolution in time. Firstly, a qualitative analysis of perturbed solutions has been presented, identifying a pairing instability mechanism. A quantitative analysis has then been included, giving the distribution of the growth rate of the perturbation as a function of the wavenumber. This analysis has been presented for different flight configurations. Finally, the spatio-temporal evolution of the perturbation has been analyzed, identifying the regimes where solutions are convectively and absolutely unstable.

Chapter 4

Rigid blade

Contents

| | | |
|------------|---|------------|
| 4.1 | Chapter overview | 88 |
| 4.2 | Rigid blade framework | 88 |
| 4.2.1 | Induced velocity on the rotor | 88 |
| 4.2.2 | Circulation law and equivalent Joukowski profile | 89 |
| 4.2.3 | Aerodynamic loads | 91 |
| 4.2.4 | Tip effect correction | 91 |
| 4.2.5 | Model parameters | 92 |
| 4.3 | Comparison with numerical and experimental results | 92 |
| 4.3.1 | MEXICO rotor project | 92 |
| 4.3.2 | The Unsteady Aerodynamic Experiment (UAE) | 96 |
| 4.3.3 | A hovering case: NASA Technical report TM81232 | 98 |
| 4.4 | Chapter conclusion | 100 |

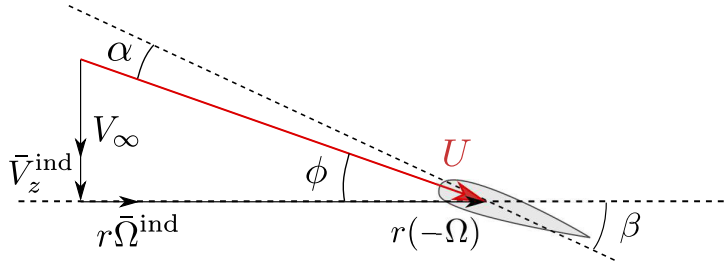


Figure 4.1: Schematic of the airfoil and the different contributions to the local velocity U for a climbing helicopter flight configuration

4.1 Chapter overview

In this chapter, a coupled blade/wake model is developed for a rigid rotor. Helical wake solutions obtained in chapter 2 are used to compute the induced flow across the rotor. In section 4.2, the problem framework is presented. The calculation of the velocity on the rotor is detailed, evaluating the effect of the velocity induced by the wake. The computation of the circulation profile and the aerodynamic loads for a given blade geometry is performed, establishing the coupling between the wake and the rigid rotor. Then, in section 4.3, some experimental and numerical examples are compared with the solutions obtained by the model in order to validate it.

4.2 Rigid blade framework

4.2.1 Induced velocity on the rotor

To compute the circulation or the aerodynamic forces along the blade the local velocity on the blade is required. To avoid singularity problems coming from integrating Biot-Savart law on the blades, especially at the emission points of the vortices, the induced velocity at each radial position of the rotor is calculated as the average value around all the rotor disc:

$$\bar{\mathbf{V}}^{\text{ind}}(r) = \frac{1}{2\pi r} \int_0^{2\pi} \mathbf{V}^{\text{ind}}(r, \theta) d\theta. \quad (4.1)$$

This average procedure is justified by the azimuthal symmetry observed on the induced velocity field (figure 2.32). It also strongly stabilizes the numerical algorithm.

Then, the local velocity is computed as the combination of the external axial velocity, the rotation of the blades and the velocity induced by the wake:

$$\mathbf{U} = V_\infty \mathbf{e}_z + r(-\Omega) \mathbf{e}_\theta + \bar{\mathbf{V}}^{\text{ind}}, \quad (4.2)$$

so the modulus of the local velocity and the angle of attack (figure 4.1) at each radial position of the blade are given by :

$$U(r) = \sqrt{(V_\infty + \bar{V}_z^{\text{ind}}(r))^2 + r^2(-\Omega + \bar{\Omega}_l^{\text{ind}}(r))^2}, \quad (4.3)$$

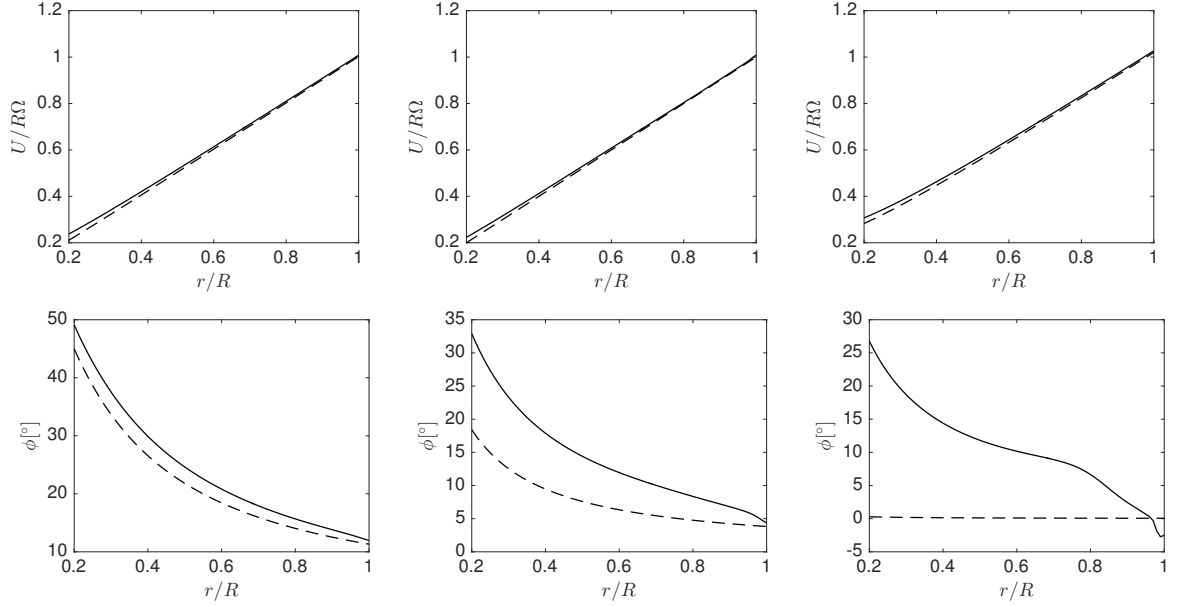


Figure 4.2: Comparison of the local velocity (upper) and the angle of the flow with the rotor plane (lower), considering just the external flow and the rotation of the blades (dashed line) and considering also the velocity induced by the wake (solid line). The wake is calculated with a circulation parameter of $\eta = 0.05$, a normalized core size of $\varepsilon = 0.01$ and a tip-speed-ratio of $\lambda = -5$ (left), $\lambda = -15$ (center) and $\lambda = \infty$ (right).

$$\alpha(r) = \beta(r) - \phi(r) = \beta(r) - \arctan \left(\frac{V_\infty + \bar{V}_z^{ind}(r)}{r(-\Omega + \bar{\Omega}^{ind}(r))} \right), \quad (4.4)$$

where β is the pitch angle of the blade and ϕ is the angle of the flow with the rotor plane.

In figure 4.2, the effect of the wake induction on the rotor is illustrated. The local velocity and its angle with the rotor plane is shown for different tip-speed-ratio and compared with the external velocity observed by the rotor without considering the induced velocity. For the local velocity U , there is not a significant difference for any tip-speed-ratio, just a small difference that appears near the axis, where the contribution from the rotation of the blades is reduced. However, the angle ϕ is crucially affected when the tip-speed-ratio grows. For $\lambda = -5$, a small gap is observed in the effective angle when the induction is considered or not. For $\lambda = -15$, the difference grows, especially near the axis, where the azimuthal velocity is reduced with the radial position. Finally, in hovering flight, the external axial flow disappears and the angle ϕ falls to 0 if the induced velocity is not considered.

4.2.2 Circulation law and equivalent Joukowski profile

Once the flow across the rotor disc is known, the circulation profile can be calculated applying the Kutta-Joukowski formula at each radial position:

$$\bar{\Gamma}(r) = \frac{1}{2}c(r)U(r)C_L(\alpha; r), \quad (4.5)$$

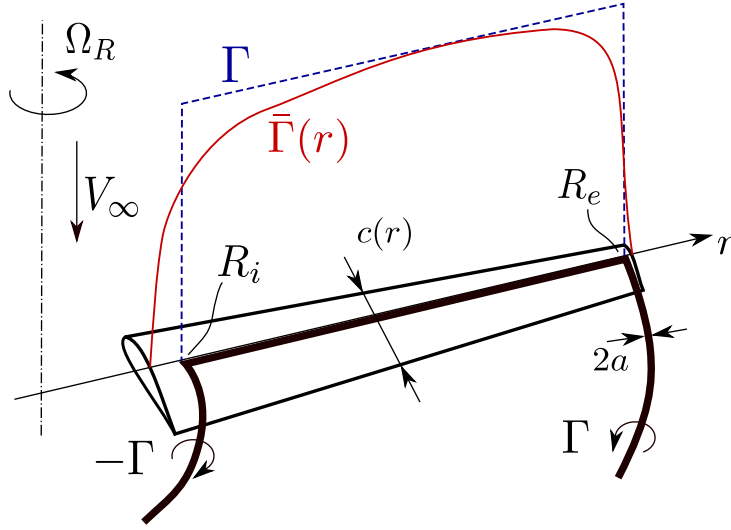


Figure 4.3: Scheme of the circulation profile $\bar{\Gamma}$ along a blade and the equivalent Joukowski profile of constant circulation Γ between the vortex emission points R_i and R_e .

where c is the chord of the blade and C_L is the lift coefficient as a function of the angle of attack for a given airfoil geometry.

As it was presented in section 1.2.3, the variations of the circulation profile along the blade are responsible of the emission of a vorticity sheet on the wake. In the Joukowski model analyzed in chapter 2, all the vorticity is concentrated in two vortices, at the tip and the hub. To obtain this wake configuration, the circulation profile along the blade has to be constant, so all the variation of circulation is produced at the ends of the blade and concentrated just in two vortices. In real cases, there are always variations on the circulation profile. To obtain wake solutions such as those studied in the previous chapter, the variable circulation profile is transformed into an equivalent Joukowski profile.

From a circulation profile $\bar{\Gamma}(r)$, calculated from Kutta-Joukowski law (figure 4.3), the circulation Γ of the equivalent Joukowski profile is obtained as the maximum value on the calculated profile:

$$\Gamma = \max(\bar{\Gamma}(r)). \quad (4.6)$$

For the generalized Joukowski model, the radial position of the points of the blade where the vortices are emitted are calculated as the centroid of the gradient of circulation at both sides of the maximum value of $\bar{\Gamma}(r)$:

$$R_i = \frac{\int_0^{r(\Gamma)} r \frac{d\bar{\Gamma}}{dr} dr}{\int_0^{r(\Gamma)} \frac{d\bar{\Gamma}}{dr} dr}; \quad R_e = \frac{\int_{r(\Gamma)}^R r \frac{d\bar{\Gamma}}{dr} dr}{\int_{r(\Gamma)}^R \frac{d\bar{\Gamma}}{dr} dr}, \quad (4.7)$$

where $R_i = 0$ for the standard Joukowski model.

As initially explained by Goldstein (1929), when the circulation is not uniform, vorticity is emitted all along the blade with a circulation per length equal to $-\partial_r \Gamma$. The subsequent evolution is a complicated roll-up process of the vortex sheet into vortices of

positive and negative circulation (1.6b). In the simplest case where the circulation profile has a single maximum, each blade is expected to create two concentrated vortices of opposite circulation at the positions of the center of mass of $\partial_r \Gamma$ distribution at both sides of the maximum. In that case, after the roll-up phase, the flow is then composed of N pairs of vortices of opposite circulation for a N blade rotor. In our model, we assume that this rolling-up is produced instantly after the rotor. In the standard Joukowski model, it is assumed that all hub vortices merge together in a single straight vortex on the axis of circulation $-N\Gamma$. In the case of several local maximum values in the circulation along the blade, the vorticity sheet will be expected to roll-up in several vortices of alternative circulation sign.

4.2.3 Aerodynamic loads

Similarly to the circulation profile, the aerodynamic loads are calculated at each radial position of the blade. The forces normal and tangential to the airfoil are given by

$$f_n = \frac{1}{2} \rho c U^2 (C_L(\alpha) \cos(\alpha) + C_D(\alpha) \sin(\alpha)), \quad (4.8)$$

$$f_t = \frac{1}{2} \rho c U^2 (C_D(\alpha) \cos(\alpha) - C_L(\alpha) \sin(\alpha)). \quad (4.9)$$

In this chapter, these forces are computed and compared with results published in the literature. These formulas can be directly derived from lift and drag forces expressions (1.16).

4.2.4 Tip effect correction

The trailed vortex generated at the tip of the blades generates in that region a high local inflow that reduces the lifting capability. This is commonly known as *tip loss* (Leishman, 2006). It is a 3D effect that is not considered in many two-dimensional models as the BET.

To model the effect of these tip losses that our two-dimensional model for blade loads does not take into account, a correcting factor extracted from Sørensen (2016) will be employed:

$$F = \frac{2}{\pi} \arccos \left[\exp \left(-\frac{N_b(R-r)}{2r \sin \phi} \right) \right]. \quad (4.10)$$

This formula is the classic Prandtl's tip loss factor (Glauert, 1935), which is directly applied to correct the loading:

$$\bar{\Gamma}^* = F \bar{\Gamma}, \quad f_n^* = F f_n, \quad f_t^* = F f_t. \quad (4.11)$$

In figure 4.4, the effect of Prandtl's tip loss factor on the circulation and the aerodynamic loads is illustrated. In the three cases a similar effect is observed. Before applying the correction, circulation and aerodynamic forces grow along the blade (which is a typical distribution on the straight rotor blades) until the tip, where they fall suddenly to 0. When the correction factor is applied, the pressure drop near the tip is modeled and the fall of the circulation and the forces is smoother.

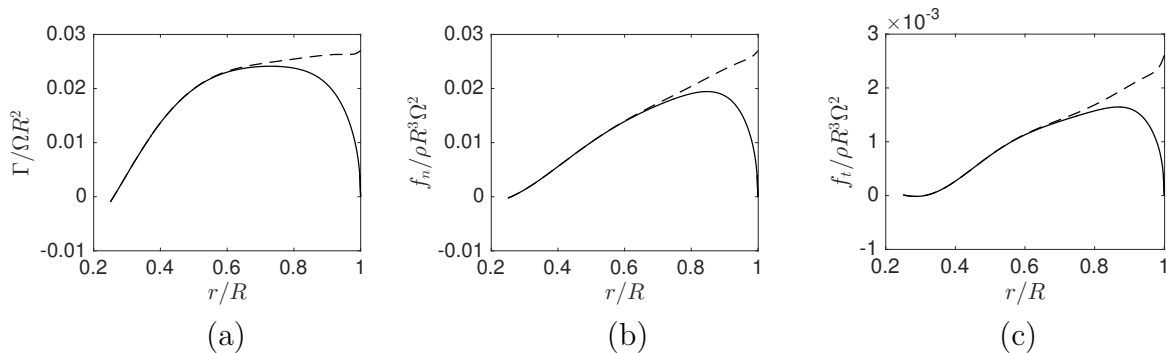


Figure 4.4: (a) Circulation, (b) normal force and (c) tangential force profiles along the blade with (solid line) and without (dashed line) tip-loss correction. Wind turbine configuration at $\lambda = 7$ for the *UAE* blade (section 4.3.2).

4.2.5 Model parameters

After the coupling between the wake and the rotor through the circulation law and the Joukowski equivalent model, for a given tip-speed-ratio, the rigid rotor problem is governed just by the geometry of the blade. The geometry is characterized by the distribution of the chord $c(r)$ and the pitch angle $\beta(r)$ and the lift and drag coefficients of the airfoil profile C_L and C_D .

The problem is solved iteratively in two main steps. First, the wake is computed using initial guess values for η , R_{tip} and R_{hub} . Then, from the wake, we compute the averaged velocity on the rotor and, using the geometrical properties of the blade, the circulation profile. With this circulation profile, new values for η , R_{tip} and R_{hub} are obtained. This process is explained in detail in the appendix.

4.3 Comparison with numerical and experimental results

In this section, the model is compared to several experimental and numerical results: two wind turbine rotors and one helicopter rotor in hovering regime. Both wind turbine cases are calculated at different tip-speed-ratios. Experimental measurements of aerodynamic loads are used to compare and validate the model. Additionally, comparisons with numerical and experimental results are addressed for the wake geometry or the local velocity and angle of attack on the blades. For each case, the circulation profile along the blade is computed and plotted together with the equivalent Joukowski circulation profile.

4.3.1 MEXICO rotor project

The MEXICO (Model experiments in Controlled Conditions) (Schepers & Snel, 2007; Schepers *et al.*, 2012; Snel *et al.*, 2007) was a project developed in Netherlands with the objective of creating a database with aerodynamic and flow measurements on a wind turbine to be used as a benchmark for model validation. The database contains exhaustive experimental and numerical results from BEM and CFD modelling for the near wake flow

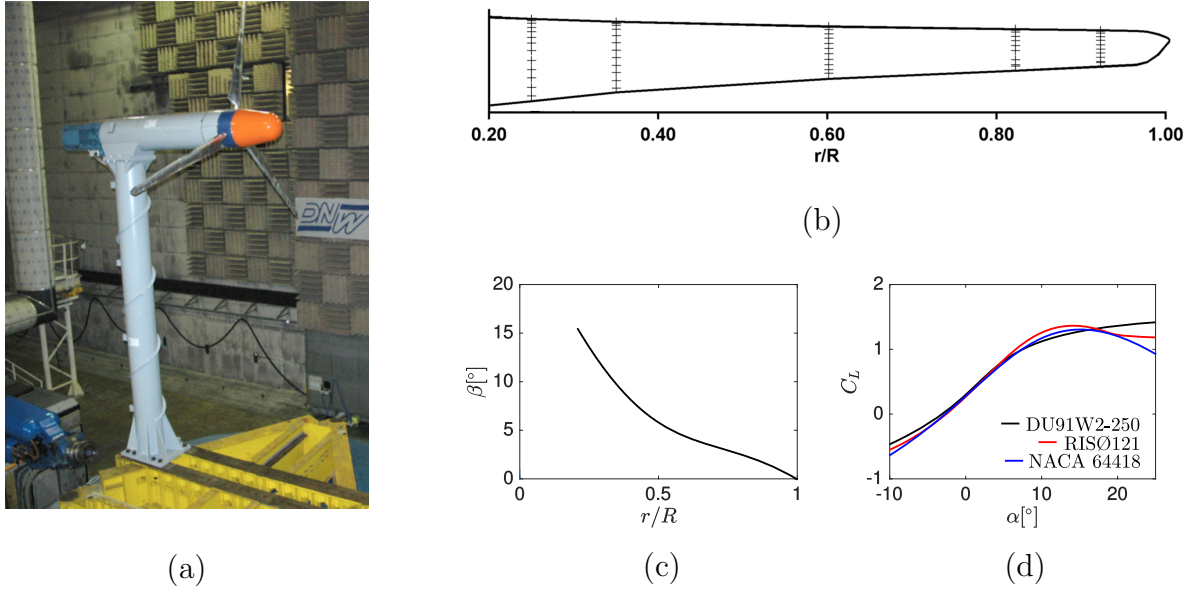


Figure 4.5: (a) MEXICO wind turbine installation (from Schepers & Snel (2007)). (b) Chord distribution of the blade (c) Pitch angle (d) Lift coefficient of the three airfoil geometries.

and the rotor loads. The experiment consists of a three bladed wind turbine model, 4.5 m in diameter, installed in a wind tunnel of squared section ($9.5 \times 9.5 \text{ m}^2$) (figure 4.5). The airfoil profile is not constant along the span but it changes between three different geometries: DU91W2-25, RISO121 and NACA64418 (in figure 4.5 are shown the lift coefficients for the three airfoil geometries). Chord and pitch distributions are shown in figure 4.5b and figure 4.5c. All the measurements were made for three different tip-speed-ratio values, modifying the external flow at $V_\infty = 10 \text{ m s}^{-1}$ ($\lambda = 10$), $V_\infty = 15 \text{ m s}^{-1}$ ($\lambda = 6.67$) and $V_\infty = 24 \text{ m s}^{-1}$ ($\lambda = 4.17$) for a fixed rotation of 424.5 rpm .

In figure 4.6 the distributions of the local velocity and of the angle of attack are shown for the three tip-speed-ratio configurations analyzed in MEXICO. The local velocity is very similar for the three cases, especially at the tip; however, the flow is slightly stronger near the axis, when the wind speed is higher ($\lambda = 4.17$). Concerning the angle of attack, the differences are more important. For $\lambda = 10$ the angle of attack does not vary very much: the variation of the incident velocity direction is balanced by the twist of the blade. When the wind speed increases, the blade twist is not sufficient, so the variable distribution due to the rotation of the blades (see figure 4.2) becomes more evident. A maximum variation of 9° and 18° are observed for the angle of attack for $\lambda = 6.67$ and $\lambda = 4.17$ respectively. A comparison with numerical results extracted from Schepers & Snel (2007) is presented. A perfect agreement is observed for the local velocity (it mainly depends on the external velocity, as was analyzed in section 4.2.1). For the angle of attack, a very good agreement is found with the published numerical results, both qualitatively and quantitatively.

In figure 4.7, the circulation profile along the blades is shown for the three rotor configurations. A quite constant distribution is observed, especially for the higher tip-

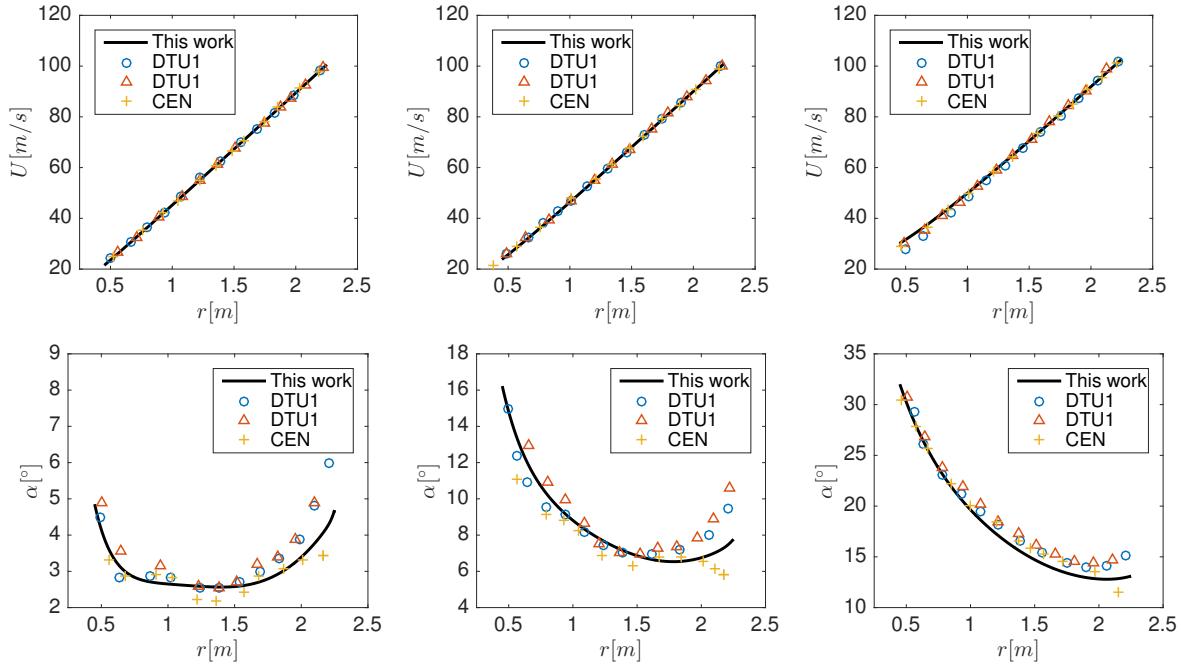


Figure 4.6: Distribution of the local velocity (upper) and the angle of attack (lower) for the three different axial velocities: $\lambda = 10$ (left), $\lambda = 6.67$ (center) and $\lambda = 4.17$ (right). The results obtained with our model (solid line) are compared to three different numerical results extracted from Schepers & Snel (2007): two different contributions from DTU (Delft University of Technology) and one from CENER (National Renewable Energy Center of Spain).

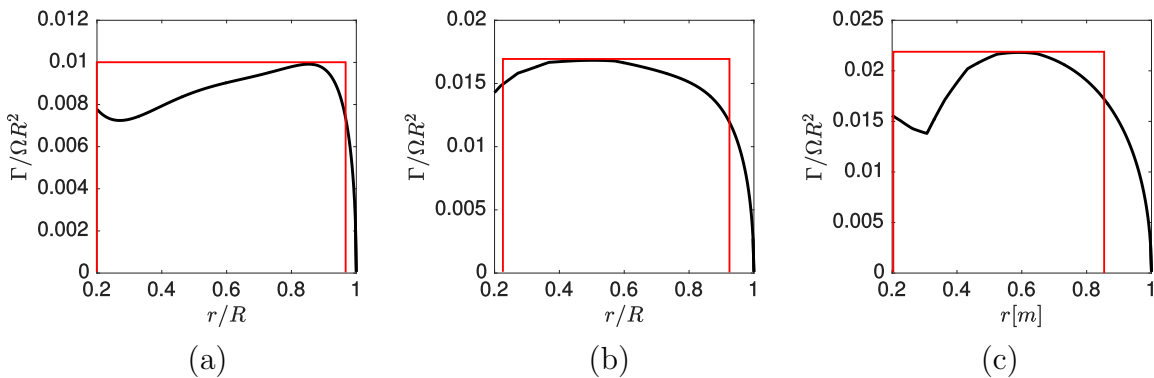


Figure 4.7: Distribution of the circulation along the blades for the three different axial velocities: $\lambda = 10$ (left), $\lambda = 6.67$ (center) and $\lambda = 4.17$ (right). In red line, the equivalent Joukowski constant circulation profile.

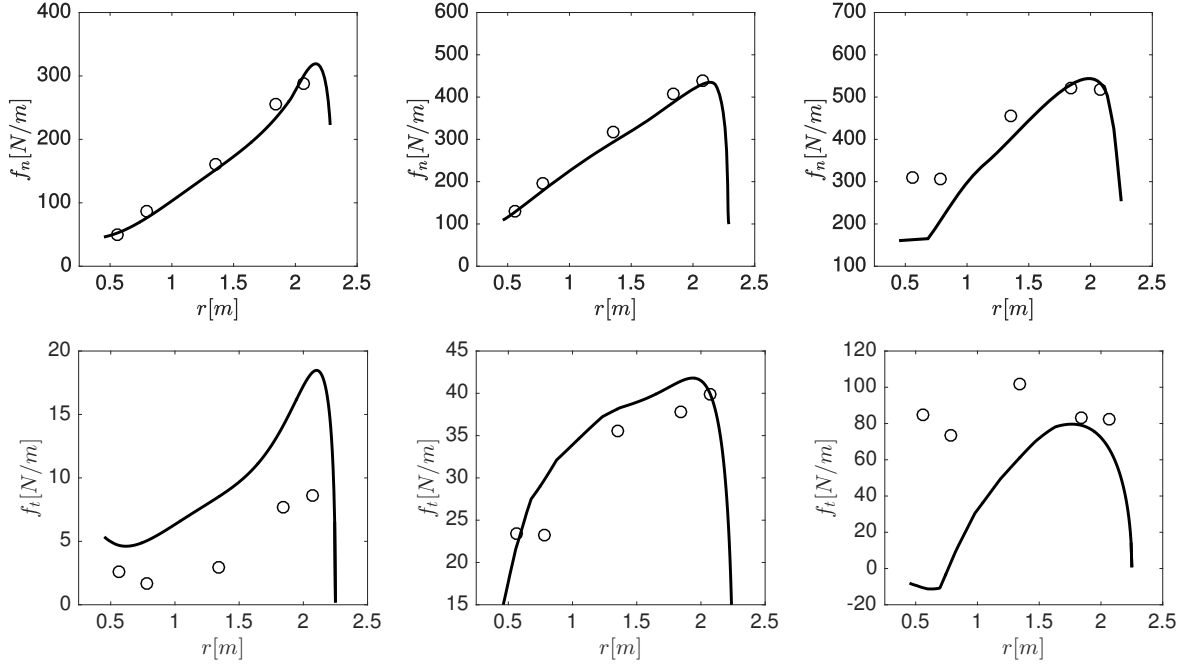


Figure 4.8: Distribution of the normal (upper) and tangential (lower) forces for $\lambda = 10$ (left), $\lambda = 6.67$ (center) and $\lambda = 4.17$ (right). The markers correspond to the experimental measurements from Schepers & Snel (2007).

speed ratio cases. For the low tip-speed ratio case, the circulation is softened near the tip, so the vortex emission point is displaced inside the blade. These distributions are in good agreement with the hypothesis of Joukowski's constant circulation profile. It can be observed a linear increase of the maximum circulation value with the external velocity

In figure 4.8, distribution of the normal and tangential aerodynamic forces is shown. The similar growing tendency is observed for both forces for every tip-speed-ratio. The strength of the forces grows with the local velocity, that also increases with the external wind. The tangential force is approximately one order of magnitude weaker than the normal force. Compared to the experimental measurements, a very good agreement is found, especially for the normal force at $V_\infty = 10 \text{ m s}^{-1}$ and $V_\infty = 15 \text{ m s}^{-1}$. For the tangential force, a quantitative deviation is noticed, although the agreement is still qualitatively good. A discrepancy between theory and experimental data is observed for the tangential force for $V_\infty = 24 \text{ m s}^{-1}$, however, the same observation was also made with all the numerical results presented in Schepers & Snel (2007) for the same case.

In figure 4.9, the geometry of the wake is shown for $\lambda = 6.67$ ($V_\infty = 15 \text{ m s}^{-1}$) and $\lambda = 10$ ($V_\infty = 10 \text{ m s}^{-1}$). As it was analyzed in chapter 2, the wake gets more expanded for high tip-speed-ratios. In this case, the solutions are compared to CFD results from Carrion *et al.* (2015). The agreement is specially good for $V_\infty = 15 \text{ m s}^{-1}$. For $V_\infty = 10 \text{ m s}^{-1}$, some differences are found for the pitch of the hub vortices. This deviation can be explained by the dissipation of the vortices in the CFD results. In Carrion *et al.* (2015), the external vortices start to dissipate at a distance of $1.2R$ from the rotor, this probably affects the induced flow on the hub helices: they are not slowed down by the external vortices so they get axially expanded.

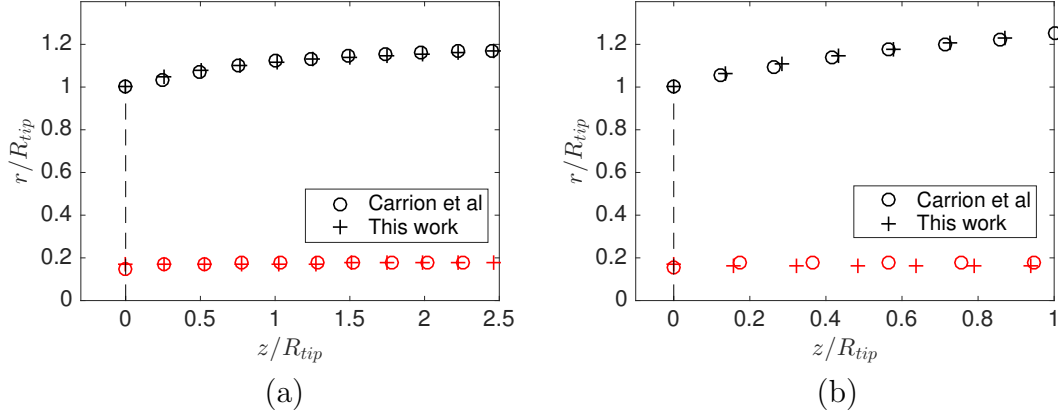


Figure 4.9: Geometry of the wake for (a) $\lambda = 6.67$ and (b) $\lambda = 10$. The markers correspond to the position of the tip (black) and hub (red) vortices of the wake crossing the $r - z$ plane. Comparison with numerical CFD results from Carrion *et al.* (2015).

4.3.2 The Unsteady Aerodynamic Experiment (UAE)

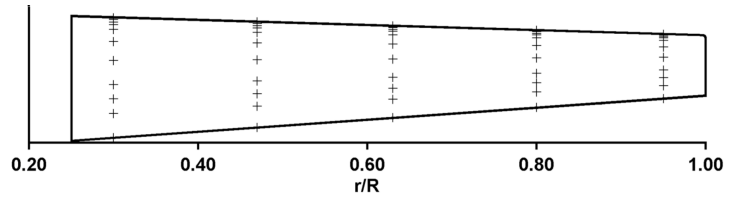
The UAE (Hand *et al.*, 2001) is a experiment similar to the MEXICO project. It consist in a two-bladed wind turbine rotor with a diameter of 10.1m (figure 4.10a) in the NASA Ames wind tunnel (24 x 36m). The chord of the blade is shown in figure 4.10b. The airfoil profile is a tS809 for all the blade, twisted with a variable angle distribution (figure 4.10c). The experiment presents an extensive variety of measurements with different rotor configurations, including yawed flow, parked rotor, variable cone angle, different blade pitches or transitory regimes. In this work, only the measurements of *sequence H* (see Hand *et al.* (2001)) are used, which correspond to a rotation of $72rpm$ for three different axial flows of $V_\infty = 5 m s^{-1}$, $V_\infty = 7 m s^{-1}$ and $V_\infty = 10 m s^{-1}$, giving tip-speed-ratios of $\lambda = 7.58$, $\lambda = 5.41$ and $\lambda = 3.79$ respectively.

In figure 4.11, the circulation profile along the blades is shown for the three rotor configurations. A blunt distribution is observed for the three cases. However, Joukowski's equivalent circulation profile is still satisfactory. In this case, as the circulation distribution is quite soft at the ends of the blade, the emission points are slightly displaced inside the blades. As occurs with MEXICO rotor, it can be observed a linear increase of the maximum circulation with the external velocity.

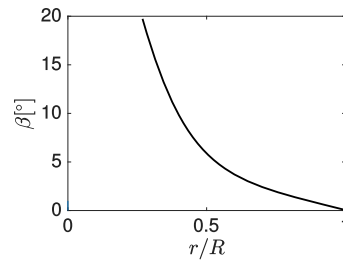
In figure 4.12 we show the distribution of the normal and tangential aerodynamic forces. Similar distributions as in MEXICO measurements are found when the external flow is increased. A very good agreement with the experimental data is noticed for both forces, even for a low tip-speed-ratio of $\lambda = 3.8$. Although a certain deviation is observed for some specific points, the distribution of the forces is always quantitatively and qualitatively reproduced.



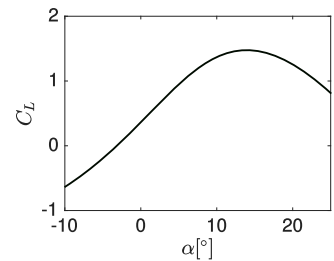
(a)



(b)

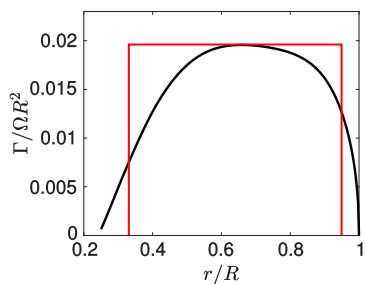


(c)

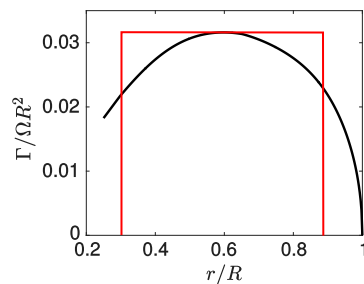


(d)

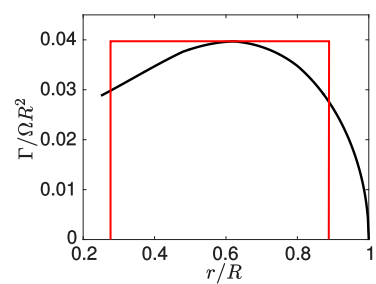
Figure 4.10: (a) UAE Phase VI wind turbine installation (from Sicklinger *et al.* (2015)). (b) Chord distribution of the blade (c) Pitch angle (d) Lift coefficient of the airfoil geometry.



(a)



(b)



(c)

Figure 4.11: Distribution of the circulation along the blades for the three different axial velocities: $\lambda = 7.58$ (left), $\lambda = 5.41$ (center) and $\lambda = 3.79$ (right). In red line, the equivalent Joukowski constant circulation profile.

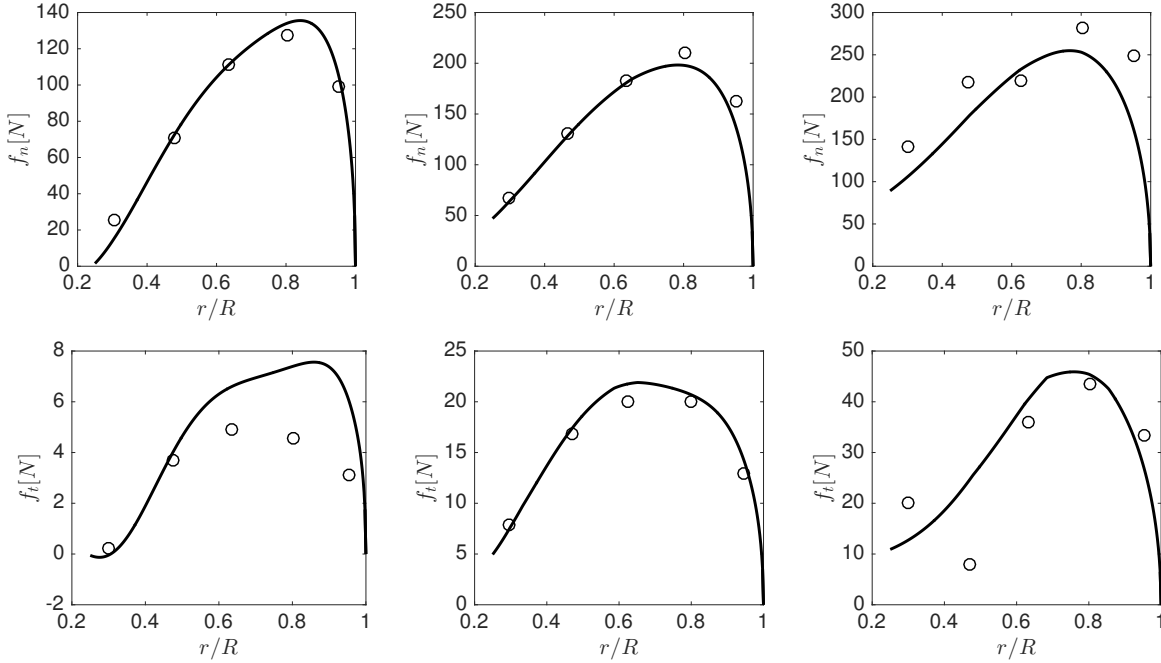


Figure 4.12: Distribution of the normal (upper) and tangential (lower) forces for $\lambda = 7.58$ (left), $\lambda = 5.41$ (center) and $\lambda = 3.79$ (right). The markers correspond with the experimental measurements from Hand *et al.* (2001).

4.3.3 A hovering case: NASA Technical report TM81232

To compare the model in a hovering case, some data have been extracted from a two-bladed rotor experiment from NASA technical rapport TM81232 (Caradonna & Tung, 1981). The rotor has in this case an untwisted constant-chord blade with a uniform pitch angle and a NACA0012 airfoil profile. It is installed on a vertical axis, inside a wake exhaust channel to avoid a possible ground effect with the limits of the room (figure 4.13). Several measurements are presented in this rapport with different pitch angles, always in a hovering configuration, without forced external flow.

For this rotor, the agreement with the model is not as good as for the two previous cases. In the model, the wake is more contracted and the lift is underestimated in the inner part of the blade and weakly overestimated near the tip. The circulation profile obtained from the model is shown in figure 4.14a. It strongly varies with the radial position. Note in particular that it becomes negative for $r/R < 0.4$. In principle, with such a circulation profile, we expect, from Prandtl lifting-line theory, vortex sheet shedding all along the blade, and the formation for each blade of three vortices: an inner vortex at $r/R \approx 0.2$, a tip vortex at $r/R \approx 1$ and third opposite sign vortex close to $r/R = 0.6$ resulting from the roll-up of the vortex sheet. It is the merging of the root and middle vortices of all the blades that is supposed to give the hub vortex of Joukowski model. This complicated roll-up and merging process is not considered and a classical Joukowski model is used for the wake, with the hub vortex placed on the axis. It may naturally affect the induced flow in the rotor plane. For the rotor in hover, the induced flow becomes the dominant part of the flow close to the rotor center. It is therefore in this region that the largest

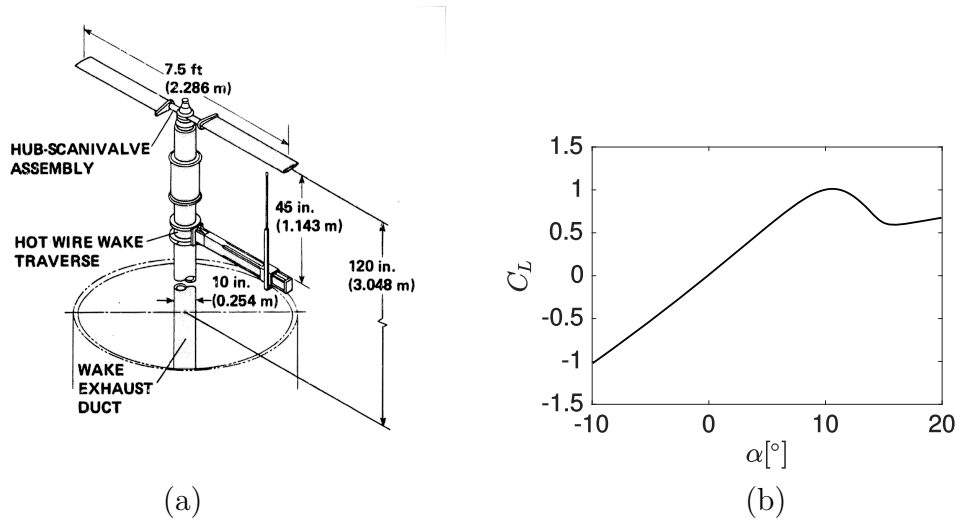


Figure 4.13: (a) Scheme of the rotor installation for NASA technical report TM81232. (b) Lift-coefficient profile of the NACA0012 airfoil.

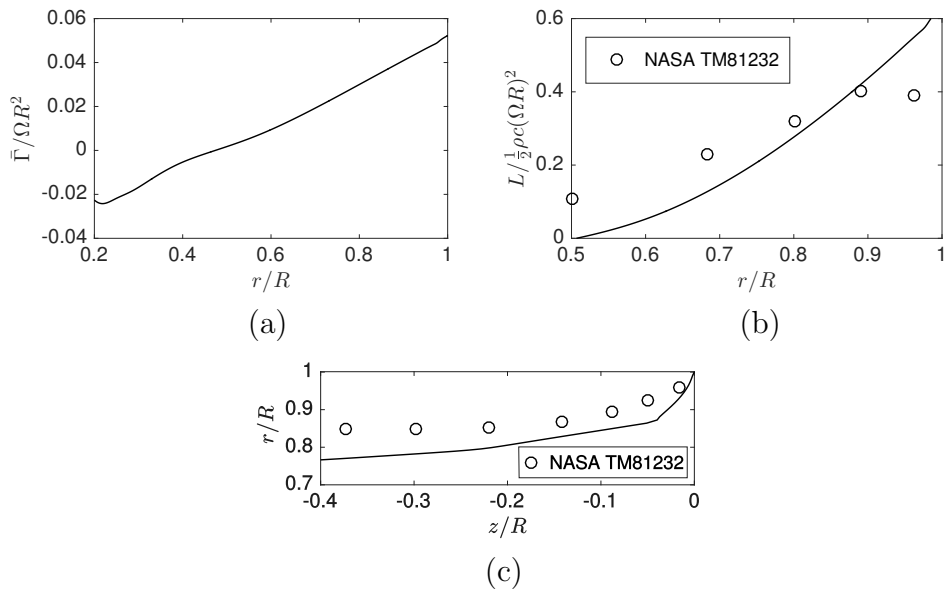


Figure 4.14: (a) Circulation and (b) lift force along the blade. (c) Radial trajectory of the wake. Comparison between our numerical results (-) and the experimental data from NASA technical rapport TM81232 (o).

inaccuracy can be expected.

The discrepancy observed in the wake geometry (figure 4.14c) may not be associated with the model. Indeed, the experimental rotor is fixed on a big shaft aligned with the wake axis. We suspect that the shaft limits the contraction of the wake. It is not excluded that it could also influence the lift forces. For these reasons, it is difficult to have a definite opinion on the errors associated with the model for this case.

4.4 Chapter conclusion

In this chapter, the coupling between the wake and a rigid rotor has been implemented. A model has been presented where the effect of the wake induction on the blades is taken into account. The importance of this effect has been analyzed for different tip-speed-ratios. For a given blade geometry, defined by the chord, the twist angle and the aerodynamic coefficients, the problem is completely defined for a chosen tip-speed-ratio. To validate the model, a comparison with several numerical and experimental examples of the literature has been made. A very good agreement has been found with wind turbine cases. The comparison with hovering rotor case is still good, but not as good as with the wind turbine rotors. Moreover, we cannot exclude that the discrepancies are associated with particularities of the experimental set up. Further comparisons would be needed to fully assess the validity of the model in hover or for other rotors.

Chapter 5

Flexible blade

Contents

| | | |
|------------|------------------------------------|------------|
| 5.1 | Chapter overview | 102 |
| 5.2 | Deformation model | 102 |
| 5.3 | Fluid-structure interaction | 105 |
| 5.4 | Applications | 105 |
| 5.4.1 | Description of the rotors | 105 |
| 5.4.2 | Results | 106 |
| 5.5 | Chapter conclusion | 109 |

5.1 Chapter overview

In this chapter, we implement the last part of the model: the deformation of the rotor blades. The model for the rigid rotor presented in the previous chapter will be still used to compute aerodynamics loads. However, these loads will deform the blades. We introduce a elastic beam model to obtain the deformation of the blades under different conditions. Most of the content of the chapter is extracted from the paper *A strongly-coupled model for flexible rotors* (Durán Venegas *et al.*, 2019), published in the *Journal of Fluids and Structures*. In this paper, all the coupled model has been developed for a rod model, including a detailed framework and a parametric analysis for two different blade geometries.

5.2 Deformation model

The blade deformation is obtained using a beam model for the blade. Such a 1D model provides a simple way to compute bending and torsion from the forces exerted on the blade. We are looking for equilibrium configurations. These configurations satisfy the Kirchhoff equations (Dias & Audoly, 2015), expressing the balance of forces and moments on the blade element located at the curvilinear coordinate s

$$\frac{\partial \mathbf{T}}{\partial s} + \mathbf{f} = 0, \quad (5.1)$$

$$\frac{\partial \mathbf{M}}{\partial s} + \mathbf{d}_3 \times \mathbf{T} + \mathbf{m} = 0. \quad (5.2)$$

where \mathbf{f} and \mathbf{m} are the external forces and moments per unit length, \mathbf{T} and \mathbf{M} the internal forces and moments and \mathbf{d}_3 the vector tangent to the blade centerline. These equations are conveniently written in the local orthonormal frame $(\mathbf{d}_1, \mathbf{d}_2, \mathbf{d}_3)$ (figure 5.1a). These vectors \mathbf{d}_i , $i = 1, 2, 3$ satisfy

$$\frac{\partial \mathbf{d}_i}{\partial s} = \boldsymbol{\omega}(s) \times \mathbf{d}_i(s), \quad (5.3)$$

where the Darboux vector $\boldsymbol{\omega}(s)$ is defined by

$$\boldsymbol{\omega} = \kappa_1(s)\mathbf{d}_1(s) + \kappa_2(s)\mathbf{d}_2(s) + \tau(s)\mathbf{d}_3(s). \quad (5.4)$$

The components of $\boldsymbol{\omega}$ in the local frame are the normal curvature $\kappa_1(s)$, the geodesic curvature $\kappa_2(s)$ and the torsion $\tau(s)$. The normal curvature κ_1 and the torsion τ can also be defined in terms of a bending angle θ and a torsion angle γ (figure 5.1b)

$$\frac{\partial \theta}{\partial s} = \kappa_1, \quad \frac{\partial \gamma}{\partial s} = \tau. \quad (5.5)$$

Equations (5.1) and (5.2) have to be completed by the beam constitutive law

$$\mathbf{M} = EI\kappa_1\mathbf{d}_1 + \frac{EJ}{2(1+\nu)}\tau\mathbf{d}_3, \quad (5.6)$$

where ν is the Poisson ratio, E the Young modulus, I and J the second moments of area in the direction \mathbf{d}_1 and \mathbf{d}_3 respectively. We have assumed uniform elastic properties of the blades and neglected deformations in the direction \mathbf{d}_2 ($\kappa_2 = 0$).

Moreover, in the following, we assume that the airfoil profile is the same all along the blade, meaning that we can write $I = I^*c^4$ and $J = J^*c^4$, where I^* and J^* are dimensionless quantities. The cross section area of the airfoil can also be written as $A = A^*c^2$ where A^* is a dimensionless quantity.

The blade deformation problem is then defined by the parameters linked to the blade profile (C_L , C_D , I^* , J^* and A^*), one parameter characterizing the blade aspect ratio $c^* = c/R_b$ and three parameters associated with the blade material

$$\nu, \quad E^* = \frac{E}{\rho_b g R_b}, \quad \rho_b^* = \frac{\rho_b}{\rho}, \quad (5.7)$$

where R_b is the length of the blade, ρ_b and ρ the density of the blade and of the fluid respectively, and g the gravitational acceleration. The parameter E^* compares the elastic forces with gravity. It is also useful to introduce the Froude number Fr that compares gravitational forces with centrifugal forces:

$$Fr^2 = \frac{R_b \Omega^2}{g}. \quad (5.8)$$

In order to obtain two differential equations for θ and γ , we manipulate equations (5.1)-(5.6). For the equation on θ , we differentiate equation (5.2) with respect to s and we take its projection on the local direction \mathbf{d}_1 . After imposing $\kappa_2 = 0$, we obtain for the first term:

$$\mathbf{d}_1 \cdot \frac{\partial^2 \mathbf{M}}{\partial s^2} = \frac{\partial^2}{\partial s^2} (\mathbf{M} \cdot \mathbf{d}_1) + \tau^2 (\mathbf{M} \cdot \mathbf{d}_1) \simeq \frac{\partial^2}{\partial s^2} (\mathbf{M} \cdot \mathbf{d}_1), \quad (5.9)$$

where we neglect the term implying τ^2 , as the torsion curvature is small compared to the deflection, which will be verified a posteriori. So the final expression will be:

$$\frac{\partial^2 (\mathbf{M} \cdot \mathbf{d}_1)}{\partial s^2} + \frac{\partial \mathbf{T}}{\partial s} \cdot \mathbf{d}_2 = 0, \quad (5.10)$$

where $\kappa_2 = 0$ has been used again to obtain the second term and neglect the term coming from the external moments.

From the constitutive law (5.6) and using the definition (5.5), the first term of equation (5.10) can be written as

$$\frac{\partial^2 (\mathbf{M} \cdot \mathbf{d}_1)}{\partial s^2} = E \left(I \frac{\partial^3 \theta}{\partial s^3} + 2 \frac{\partial I}{\partial s} \frac{\partial^2 \theta}{\partial s^2} + \frac{\partial^2 I}{\partial s^2} \frac{\partial \theta}{\partial s} \right). \quad (5.11)$$

The second term of (5.10) is the projection on the direction \mathbf{d}_2 of the forces exerted on the blade (see equation (5.1)). They include the aerodynamic force perpendicular to the blade f_n , calculated using equation (4.8), the centrifugal force and the weight of the blade per unit length. In the following, the rotor axis will be assumed to be aligned with the direction of gravity, as for a helicopter in vertical flight. The projection on \mathbf{d}_2 of the centrifugal force and weight can then be written:

$$\mathbf{f}_{cent} \cdot \mathbf{d}_2 = A \rho_b r_b(s) \mathbf{e}_r \cdot \mathbf{d}_2 = A \rho_b \Omega r_b(s) \sin \theta = A \rho_b \Omega \left[R_b \int_0^s \cos \theta ds \right] \sin \theta, \quad (5.12)$$

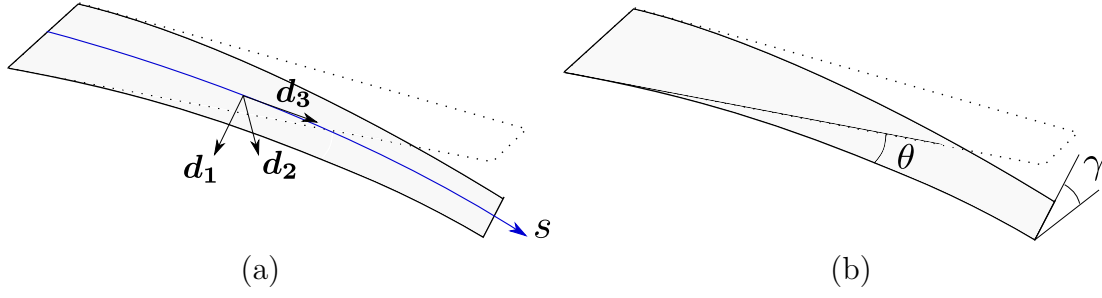


Figure 5.1: Blade schemes showing the local orthonormal frame (a) and bending and torsion angles (b).

$$\mathbf{f}_w \cdot \mathbf{d}_2 = A \bar{\rho}_b g \mathbf{e}_z \cdot \mathbf{d}_2 = A \rho_b g \cos \theta \sin(\beta + \gamma). \quad (5.13)$$

Developing equation (5.10) with (4.8), (5.11)-(5.13) we obtain the final equation for θ . The equation for γ is obtained by projecting equation (5.2) on \mathbf{d}_3 with (5.5) and (5.6). Finally, the two dimensionless differential equations for the bending and torsion angles θ and γ are:

$$\begin{aligned} \frac{\rho_b^* E^* I^*}{\text{Fr}^2} [c^{*4} \theta''' + 8c^* c'^3 \theta'' + 4(3c^* c'^2 + c^{*''} c^{*3}) \theta'] - \frac{1}{2} c^* U^{*2} (C_L(\alpha) \cos \alpha + C_D(\alpha) \sin \alpha) \\ + \rho_b^* A^* c^{*2} \left[\int_0^s \cos \theta ds \right] \sin \theta + \frac{\rho_b^* A^* c^{*2}}{\text{Fr}^2} \cos \theta \sin(\beta + \gamma) = 0, \end{aligned} \quad (5.14)$$

$$\frac{\rho_b^* E^* J_0^*}{2(1 + \nu) \text{Fr}^2} [c^{*4} \gamma'' + 4c^{*3} c'^3 \gamma'] - \frac{1}{2} c^{*2} U^{*2} [(C_L(\alpha) \cos \alpha + C_D(\alpha) \sin \alpha) \delta_{\text{cm}}^{\text{ac}} + C_{\text{m,ac}}(\alpha)] = 0, \quad (5.15)$$

where the prime denotes differentiation with respect to s . The last two terms of the bending equation (5.14) correspond to the centrifugal force and the weight of the blade. The second term of the torsion equation (5.15) corresponds to the aerodynamic moment. The quantity $\delta_{\text{cm}}^{\text{ac}}$ is the distance (non-dimensionalized by c) from the center of mass to the aerodynamic center of the airfoil, typically located at a distance of $c/4$ from the leading edge for subsonic flows. The coefficient $C_{\text{m,ac}}$ is the pitching moment coefficient of the airfoil, which is in general constant for small angles of attack and equal to zero for symmetric airfoils. The angle of attack $\alpha(s)$ and the normalized incident velocity $U^*(s) = U(s)/(\Omega R_b)$ are obtained from the wake model discussed in the next two subsections. These equations have to be integrated with the following boundary conditions

$$\theta(0) = \theta'(1) = \theta''(1) = 0, \quad \gamma(0) = \gamma'(1) = 0, \quad (5.16)$$

that correspond to a “clamped” condition at the blade root, and a “free” condition at the blade tip.

In order to analyze the blade deformations in a more intuitive way, we also introduce the bending deflection function $f_\theta(s)$ that measures the distance of each blade element from its original undeformed position.

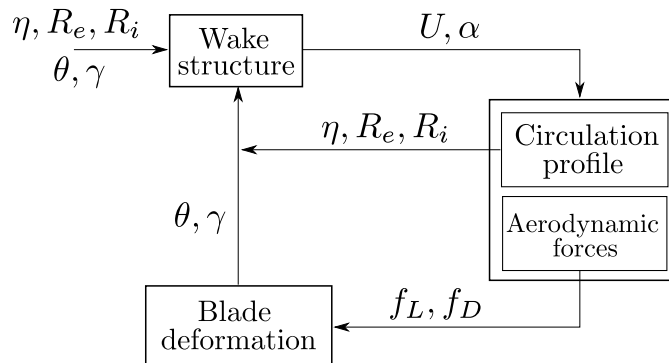


Figure 5.2: Fluid-structure loop scheme.

5.3 Fluid-structure interaction

To obtain the circulation profile of the blade, we must determine the flow in the rotor plane. But this flow, especially the induced flow, also depends on the circulation and emission point of the vortices. The wake/rotor problem is thus always strongly coupled. The solution to this problem is here obtained through an iterative procedure following a fluid-structure interaction loop (see figure 5.2).

In practice, the problem is first solved for a rigid rotor. The first loop is performed by neglecting the induced velocity, so that first estimates for the circulation profile and the resulting wake can be computed from the external velocity only. This first loop also gives an estimate of the induced velocity, so that a second loop can be performed with the full velocity field. The process is repeated until convergence.

The flexible case is treated by considering the rigid rotor configuration as guess value. The difference with the respect to the rigid case is that the circulation profile is now obtained after having computed the new position of each blade element using the beam model (section 5.2). As for the rigid case, the process is repeated until convergence.

For both rigid and flexible rotors, convergence is typically obtained in 5 or 6 loops.

5.4 Applications

5.4.1 Description of the rotors

In this section, we apply the model to two different two-bladed rotors, named here rotor A and rotor B. For both rotors, we consider a same NACA0012 profile for the blade cross-section. The characteristic constants for this profile are $I^* = 0.0033$, $J^* = 3.28$ and $A^* = 0.0822$. For the aerodynamic coefficients C_L and C_D , we assume the functions given in Chritzos *et al.* (1955) and shown in figure 5.3(b) and, for the aerodynamic moment, we use $C_{m,ac} = 0$ and $\delta_{cm}^{ac} = 0.15$. The blades of rotor A have a simple geometry with a uniform dimensionless chord $c^* = 0.1$ and a uniform twist angle β . We shall vary this angle β . Rotor B is inspired by the rotor used in the experiments by Quaranta *et al.* (2015), which was designed to have a constant circulation profile. The original geometry has been slightly modified to operate in a larger range of tip-speed ratio λ . The distributions of

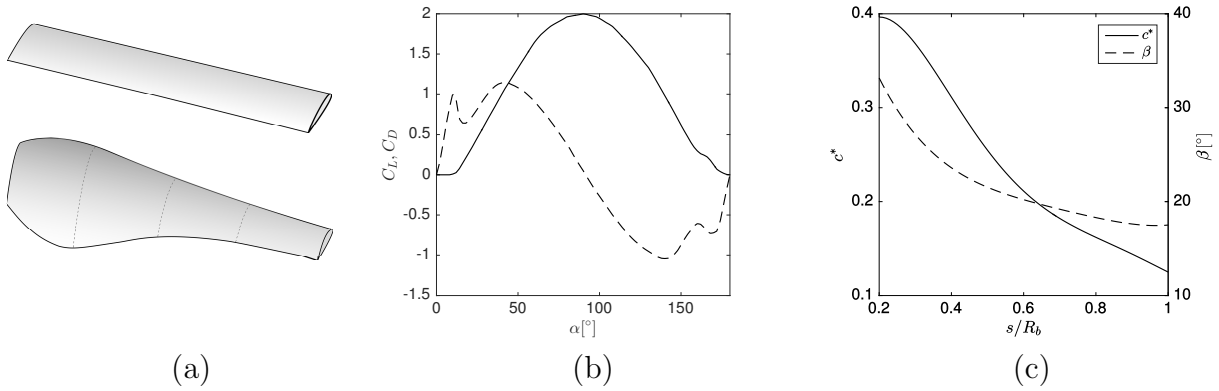


Figure 5.3: (a) Blade geometry of rotor A (upper plot) and rotor B (lower plot). (b) Lift coefficient C_L (dashed line) and drag coefficient C_D (solid line) with respect to the angle of attack α for a NACA0012 profile, from Chritzos *et al.* (1955). (c) Chord c^* and twist angle β (in degree) along the rotor B blade. Adapted from Quaranta *et al.* (2015).

chord and twist angles are shown in figure 5.3(c). The geometry of the blades of each rotor is illustrated in figure 5.3(a).

In the following section, we shall vary the operational conditions of the rotors (i.e. the angular rotation Ω and the external wind speed V_∞) that affect the tip speed ratio λ and the Froude number Fr . The material properties of the blade will also be varied such that the effect of the dimensionless parameters ρ_b^* and E^* will be considered. However, the Poisson ratio will be kept fixed and equal to $\nu = 0.5$.

Except for the twist angle of the rotor A blade, the geometry of the two rotors without external forces will not be varied. We shall also not analyse the effect of the vortex core size that is fixed to $\varepsilon = 0.01$.

5.4.2 Results

In this section, we first analyse the effect of the tip-speed ratio λ on the wake characteristics and blade shape of rotor A. We fix the Young modulus E^* , the density ratio ρ_b^* , the Froude number Fr , and vary λ by changing the external fluid velocity.

In figure 5.4, we have illustrated the radial trajectories of the vortices in the wake when λ is varied. In the rotor frame, the external wind is going downwards when λ is negative and upwards when it is positive. For a helicopter, this means that negative values of λ correspond to climbing flight, and positive values of λ to descending flight. Hover is associated with an infinite value of λ . Normal flight situations of a helicopter are shown in figure 5.4(a). For this case, the wake is contracting and moves downwards. The contraction increases when λ becomes more negative, that is when the climbing speed decreases. This contraction process continues when the climbing speed vanishes and changes sign, i.e. when we move to a slow descent flight regime corresponding to large positive values of λ . However, for this regime, the vortices are emitted upwards and therefore cross the rotor plane before going downwards. For smaller values of λ , a downward wake ceases to exist, and we jump to another type of solution shown in figure

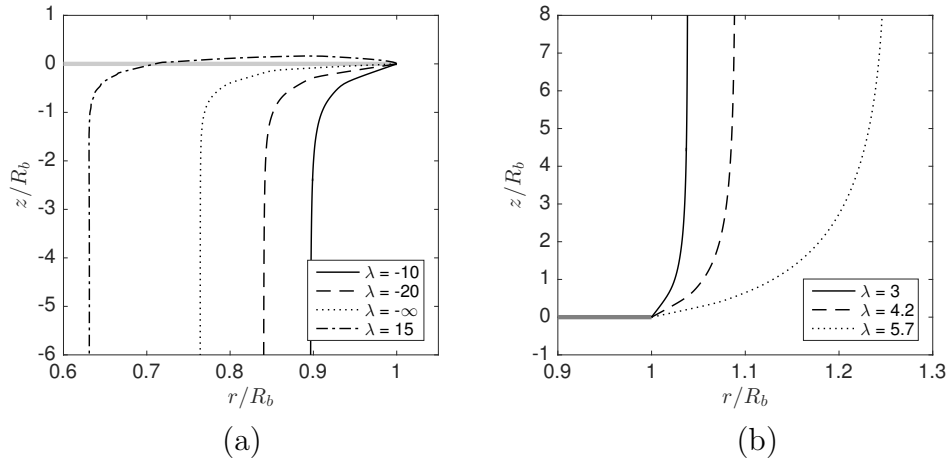


Figure 5.4: Radial position of the wake in the axial direction for different tip-speed-ratio values of rotor A. (a) Helicopter regimes for $\beta = 40^\circ$. Climbing flight ($\lambda = -10$, $\lambda = -20$), hover ($\lambda = \infty$), and weakly descending flight ($\lambda = 15$). (b) Wind turbine (or windmill brake) regimes for $\beta = 15^\circ$. Other parameters are $E^* = 10^7$, $\rho_b^* = 100$, $\text{Fr}^2 = 1000$.

5.4(b): the wake expands and goes upwards. This situation corresponds to the so-called windmill brake regime of helicopters. If gravity was not aligned with the rotor axis, it would correspond to the wind turbine regime. As expected, the stronger the external wind (i.e. the smaller λ), the less expanding is the wake.

The intervals of λ where downward and upward wakes exist do not seem to overlap. For all the parameters that we have considered, we have found an interval of λ where both solutions cease to exist. The limits of this interval are different for each case. We suspect that this is reminiscent of the Vortex Ring State (VRS) (Drees & HENDAL, 1951).

In figure 5.5, we have plotted the circulation profile obtained on the blade for the configurations shown in figure 5.4. For normal flight conditions (figure 5.5(a)), the circulation profile is found not to vary much. It is mainly associated with the blade rotation that prescribes a linear dependence of the circulation on the radial coordinate. The small bump observed for small values of s/R_b is associated with the lift coefficient crisis obtained for small angles of attack [see figure 5.3(b)]. The small overshoot of circulation observed when $\lambda = 15$ corresponds to an induction effect of the vortices that are above the rotor plane for $s/R_b > 0.7$. In the windmill brake regimes (figure 5.5(b)), a larger effect of variation is observed, with an increase of 40 % of the total circulation when λ changes from 3 to 5.7. This can be understood by the larger relative contribution of the axial wind in the total velocity for these cases.

The effect of λ on the blade deformation is shown in figure 5.6. The material chosen for the blade is weakly flexible so the deformation in terms of torsion angles (left plots) and bending angles (central plots) remains small. For normal flight conditions (upper plots), the deformation increases as the climbing velocity decreases. The largest deformation is reached for the slow descending regime. In the windmill brake regime (lower plots), the opposite behavior is observed : the deformation diminishes when the descent speed decreases. Both behaviors are in agreement with the variation of circulation with respect

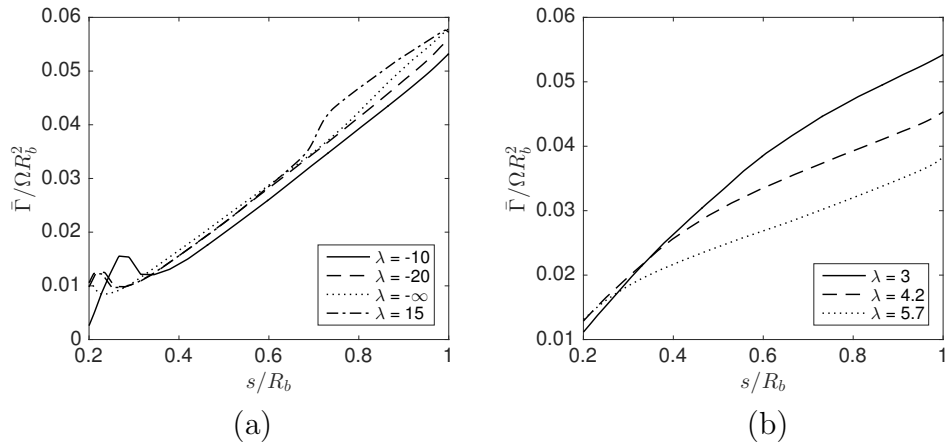


Figure 5.5: Circulation profile obtained along the blade of rotor A for different tip-speed-ratio values. (a) Helicopter regimes ($\beta = 40^\circ$); (b) Wind turbine regimes ($\beta = 15^\circ$). Other parameters are the same as in figure 5.4.

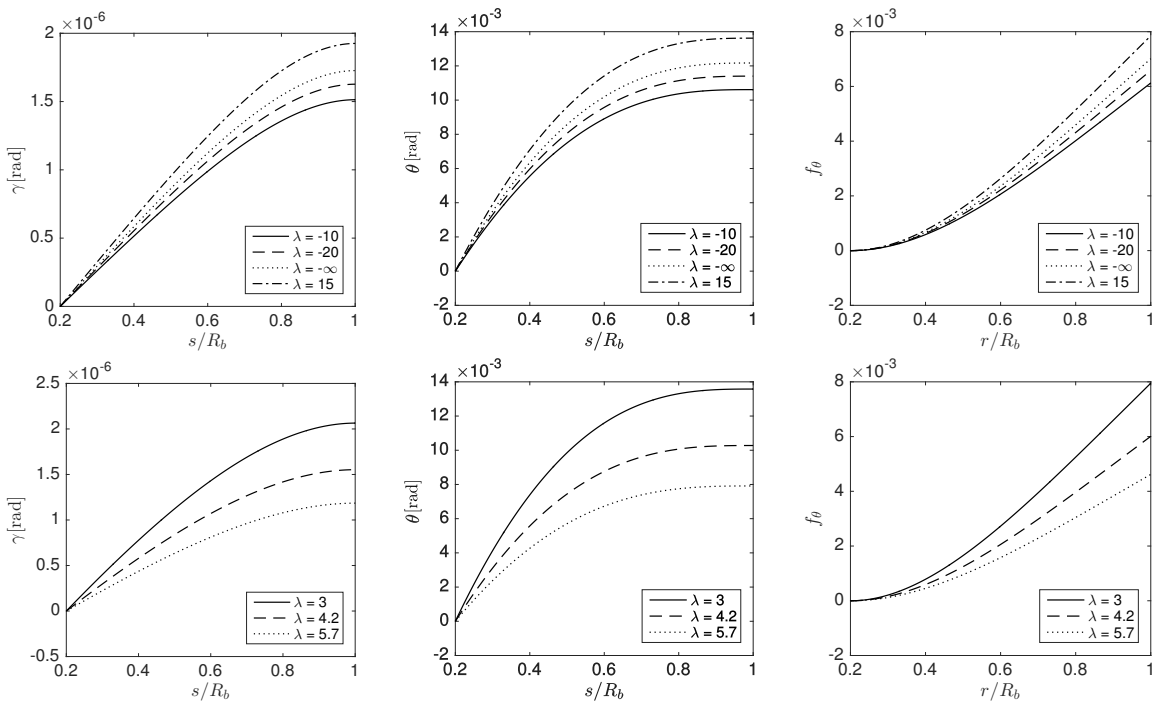


Figure 5.6: Blade deformation of rotor A for the helicopter regimes with $\beta = 40^\circ$ (upper plots) and for the wind turbine regimes with $\beta = 15^\circ$ (lower plots). Left: Torsion angle γ ; Center: Bending angle θ ; Right: Bending deflection function f_θ . The other parameters are the same as in figure 5.4.

to λ . Larger circulation leads to larger deformation. Note however that the variations of γ and θ along the blade are much smoother and do not exhibit the bumps and jumps observed in the circulation profile.

The effect of the other parameters on blade deformation for a typical climbing regime of rotor A ($\lambda = -20$) is analyzed in figure 5.7. The torsion angle γ remains always much smaller than the deflection angle θ . However, both are similarly affected by variations of E^* (upper plots), ρ_b^* (central plots) and Fr (lower plots): twisting and bending increase when E^* or ρ_b^* decreases or when Fr increases. These similarities can be understood by going back to equation (5.14). For the parameters of figure 5.7, weight and centrifugal forces remains small. If the corresponding terms (third and fourth terms in equation (5.14)) are neglected, the equations for θ and γ become dependent on the parameters E^* , ρ_b^* and Fr^2 through the combination $\rho_b^* E^* / \text{Fr}^2$ only. It is then obvious that decreasing ρ_b by a factor of 10 is equivalent to decreasing E^* by the same factor, or to increasing Fr^2 by a factor of 10.

In figure 5.7, the deformation is relatively small. Highly deformed cases can nevertheless be calculated in the same way. In figure 5.8 we illustrate such a configuration by considering a very compliant material for rotor A. We observe in figure 5.8(c), that the deflection reaches 50% of the blade length when we consider the flow conditions $\lambda = -10$, $\rho_b^* = 1$ and $\text{Fr}^2 = 100$. The same rotor at rest is however almost undeformed as seen on this figure. We see also that, even for this very deformed case, the torsion remains very small compared to the deflection. This agrees with the assumption made in equation (5.9), where the terms involving τ^2 were neglected.

So far, we have considered the simple geometry of rotor A. There is no difficulty to consider the more complex geometry of rotor B. In figure 5.9, we compare the circulation profile and blade deformation of both rotors for the same flow conditions, and the same material. We have chosen a value of λ close to conditions for which the rotor B has been designed. In figure 5.9(a), we observe that the circulation profile associated with rotor B is almost constant for $s/R_b > 0.4$ in agreement with the design properties (Quaranta *et al.*, 2015). The circulation profile obtained by rotor A is completely different. It gives a smaller vortex circulation but it gets more deformed by the flow (see figure 5.9(b-c)).

5.5 Chapter conclusion

In this chapter, the coupling between the wake and a flexible rotor has been implemented. The deformation of the blades has been added to the rigid model discussed in the previous chapter. To compute this deformation, a unidimensional beam model has been used in a local Frenet-Serret reference frame. In addition to the geometrical parameters of the rigid problem, a few parameters concerning the material properties of the blades are required. The model is used to compute the geometry of the wake, the circulation profile and the deformation of the blades at different flight configurations. In this case, the standard Joukowski model is used to compute the geometry of the wake. Stationary solutions have been obtained even for complex blade geometries and very flexible cases.

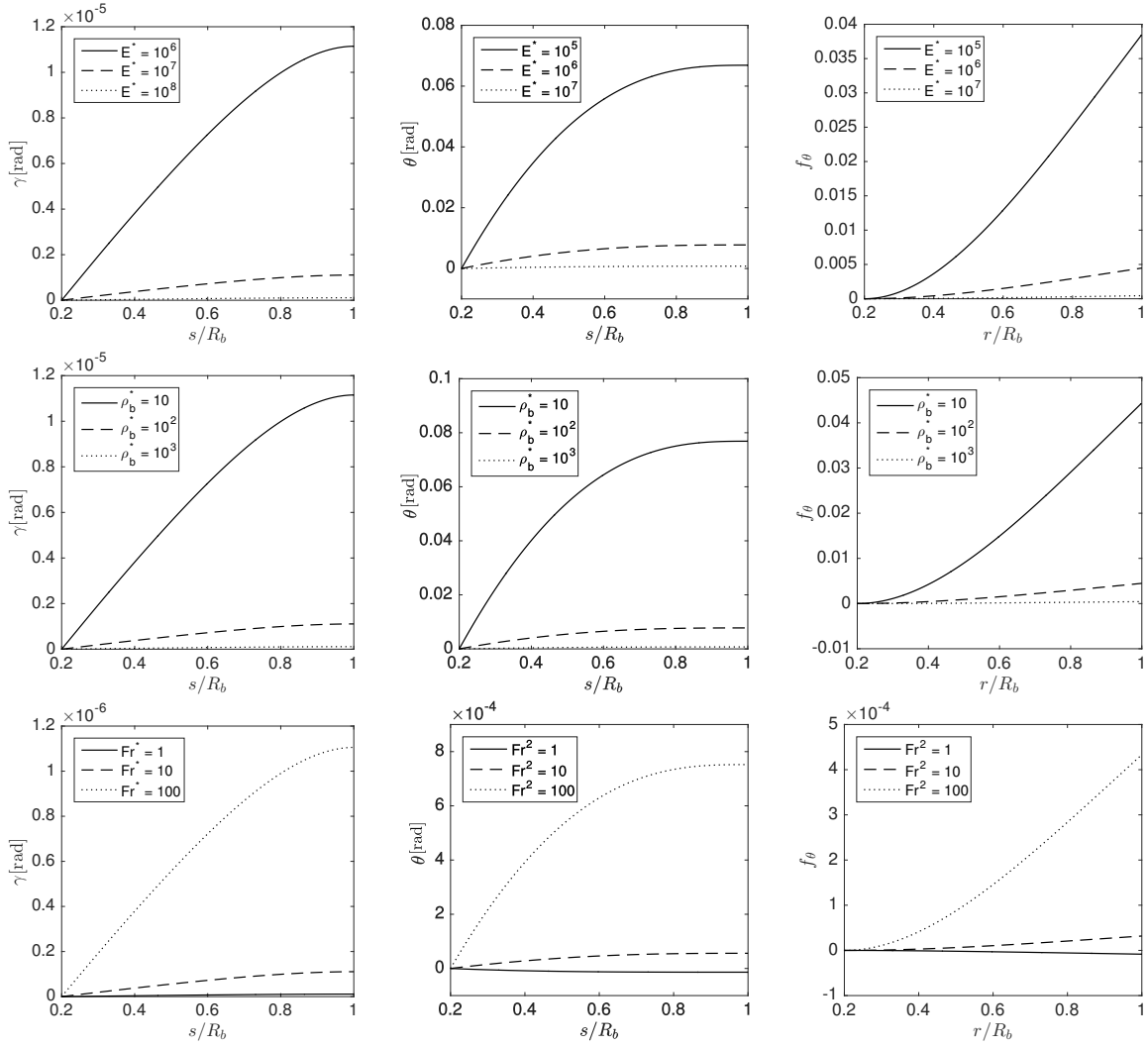


Figure 5.7: Effect of the other parameters on blade deformation of rotor A for $\beta = 30^\circ$ and $\lambda = -20$. The default parameters are $E^* = 10^6$, $\rho_b^* = 100$ and $Fr^2 = 100$. Left column: Twist angle γ ; Central column: Bending angle θ ; Right column: Bending deflection function f_θ . Upper line: Young Modulus effect. Middle line: Blade density effect. Lower line: Froude number effect.

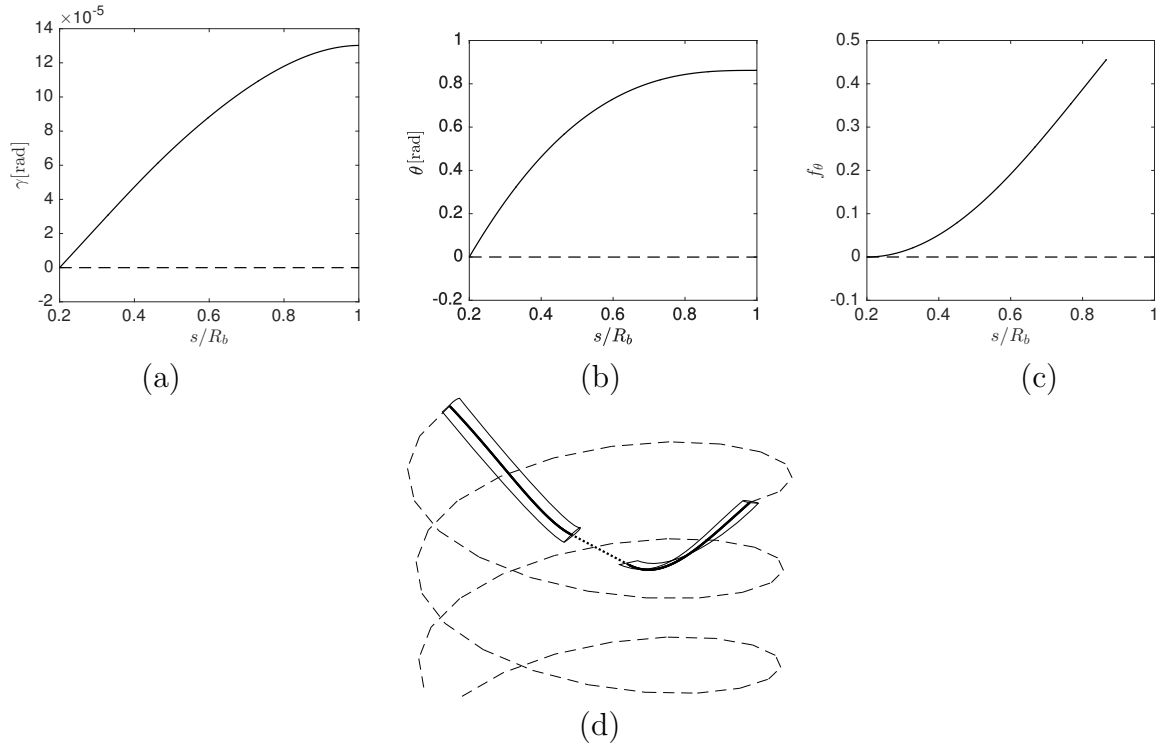


Figure 5.8: Highly deformable case. Rotor A with a twist angle $\beta = 30^\circ$ for $E^* = 10^6$, $\rho_b^* = 1$ and $\lambda = -10$. Solid line: $\text{Fr}^2 = 100$; Dashed line: $\text{Fr} = 0$ (rotor at rest). (a) Torsion angle γ ; (b) Bending angle θ ; (c) Bending deflection function f_θ . (d) Three-dimensional visualization of the wake and the deformed rotor.

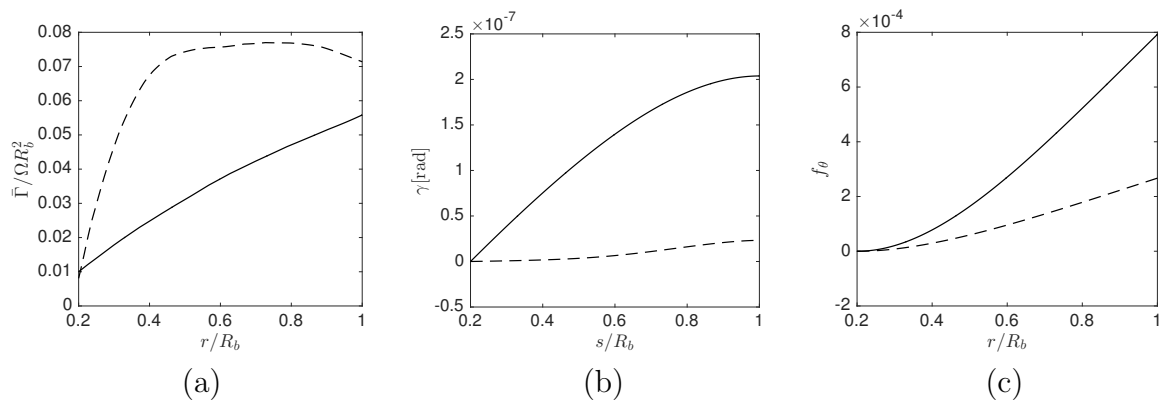


Figure 5.9: Effect of the blade geometry. Solid lines: rotor A with $\beta = 20^\circ$; Dashed lines: rotor B. (a) Circulation $\bar{\Gamma}$ along the blade; (b) Torsion angle γ ; (c) Bending deflection function f_θ . The other parameters are $\lambda = 3.5$, $E^* = 10^7$, $\rho_b = 100$, $\text{Fr}^2 = 100$.

Chapter 6

Conclusions

6.1 Achievements

The purpose of this work was to develop a model simple enough to allow an extensive parametric analysis but still physically relevant. The model provides the equilibrium state of a flexible rotor in vertical flight conditions. The solution is assumed stationary (in the frame rotating at the rotor angular speed), but takes into account the strong coupling between the rotor geometry and its wake. A simple but complete description of the blade deformation and of the wake generated by the rotor has been provided. We have shown that the model is able to describe rigid as well as very flexible rotors. The present model also works in operational conditions where classical momentum theory does not apply. In particular, it has been shown that it can describe rotors in slow descending regimes of helicopter flight, where the vortices created by the rotor move above the rotor plane before being advected downwards. This regime is often referred to as the Vortex Ring State in the helicopter community.

The achievements of this work are divided in two main parts: the analysis of the wake and its coupling with the blades, rigid or flexible.

To model the wake, a Lagrangian free-vortex model has been implemented on a prescribed Joukowski model. A generalization of the original Joukowski model has been developed where hub vortices are not necessarily placed on the axis but emitted from the blade out of axis. In that situation, each blade creates two counter-rotating vortices emitted at two different non-vanishing radii. This configuration is close to the actual wake generated by the rotors used for wind turbines. A complete analysis of far-wake structure for this generalized Joukowski model has been addressed. New numerical solutions have been obtained that extend the uniform helices that are usually used to describe the far wake generated by a rotor in axial wind. These solutions are spatially periodic and steady in a rotating and translating frame. We have shown that these solutions can be considered as deformed helices. They exhibit radial variations that increase as the internal vortex get closer to the external vortex. Simple numerical approximations have been provided that capture the main features of these solutions. We have also considered the variation of the vortex core size associated with the deformation, proving that it has a very weak effect on the main characteristics of the solutions. However, in this study, the inner structure of the vortices has not been considered. The phenomena occurring in the vortex cores,

such as short-wavelength instabilities, have therefore not been analyzed.

After having looked at the properties of the far-wake, the near wake has been analyzed. Solutions have been obtained for a wide range of rotor regimes. Classical and generalized Joukowski models have been used to describe the wake. Both models have shown to provide very similar solutions for tip vortices. A discontinuity on the topology of the solutions has been found at the transition from wind turbine to VRS regimes. For generalized model, another discontinuity is also found for climbing flight rotors. The total flow induced on the rotor disc has been calculated for the wide range of regimes and compared with momentum theory prediction. For VRS regimes, for which momentum theory does not apply, our induced flow predictions are in good agreement with experimental data. An analysis of the maximum power extracted by a wind turbine has also been performed. A very good agreement has been also found with momentum theory prediction.

The stability of classical Joukowski model solutions has been analyzed, showing that all the regimes are unstable. The instability growth rate has been extracted as a function of the wavenumber for different rotor regimes. We have shown that it is very close to the analytical results obtained by Gupta & Loewy (1974) for uniform helices. Finally, the spatio-temporal evolution of the perturbation has also been analyzed in order to identify the nature convective or absolute of the instability. Climbing flight and wind turbine regimes have been found to be convectively unstable, while VRS regimes produce absolutely unstable solutions. This naturally questions whether the solutions we have obtained in the VRS regime can be observed. It nevertheless agrees with the idea that in this regime we expect a complex temporal dynamics.

Concerning the coupling with the blades, a parametric study has been performed with a flexible rotor model. It has been shown that we are capable to describe rigid as well as very flexible rotors. The rigid version of the model has been compared to experimental data for several rotors. A good agreement has been found for the lift distribution and the wake geometry for a wind turbine rotor exhibiting an almost constant circulation distribution along its blades. However, further comparisons are needed to fully assess the validity of the model in hover or for other rotors.

It is worth emphasizing that only steady solutions have been considered. The dynamic of strongly unsteady regimes as experimentally observed in VRS regimes (Stack *et al.*, 2005; Quaranta, 2017) are outside the scope of the present work. Moreover, we have no information on the stability of the coupled solutions. We have shown that the wake is unstable with respect to long-wavelength instability (Widnall, 1972; Gupta & Loewy, 1974; Quaranta *et al.*, 2015). But other instabilities associated with the blade flexibility, such as flutter, may also be present (Eloy *et al.*, 2007; Shelley & Zhang, 2011).

6.2 Future work

Internal core structure and short-wave instabilities in helical vortices

Concerning the description of the wake, it would be interesting to include the internal structure of the vortices in the description of the helical wake. Fukumoto & Okulov (2005) and Blanco-Rodríguez *et al.* (2015) among others have shown that the core of helical vortices is deformed due to the effects of curvature, torsion and strain. In this thesis, we

have seen that the helical vortices generated by a rotor are subject to important deformations. These deformations are known to be responsible of short-wavelength instabilities that develop in vortex cores. Local curvature induces the curvature instability (Hattori & Fukumoto, 2014; Blanco-Rodríguez & Le Dizès, 2017) while strain causes the elliptic instability (Blanco-Rodríguez & Le Dizès, 2016). Both instabilities are expected to be present in the inner core of solutions. Numerical and experimental analysis of these instabilities in rotor wakes could be an interesting future work.

Vortex-Ring State dynamics

All solutions obtained in this work are stationary. For many different regimes, as climbing and hovering flight or wind turbine, equilibrium steady state is currently reached. For these cases, the model has proved to give accurate solutions. On the other hand, as it was mentioned before, some particular regimes as the Vortex Ring State are, in essence, strongly unsteady. For this kind of solutions, the study presented in this work can be very useful to predict the transition between regimes for given rotor conditions. However, the dynamic of unsteady wakes has not been addressed, which could be an interesting issue for future studies.

It would be also interesting to study the dynamic of the whole coupled problem. A dynamic coupling between wake and flexible blades would allow a better understanding of some aeroelastic instabilities such as flutter (Dowell & Hall, 2001; Paidoussis, 2004) or dynamic stall (Carr, 1988), which can also appear for rigid rotors under non-steady flows. This kind of instability is usually experimentally studied (Mullerers & Raffel, 2012). With a proper dynamic description of the coupled rotor problem, it may be possible to obtain a numerical prediction of the instability threshold and, thus, a way to avoid them.

Optimization

One of the objectives of this work was to develop a simple, computationally low-cost model to perform extensive parametric studies. The next step is to use the model together with an optimization procedure. For a rigid configuration, one could imagine modifying the blade geometry in order to optimize, for example, the performance of the rotor under particular flow conditions. For a deformable rotor configuration, same optimization procedure could also be performed by adding elastic properties of the material. Blades can be designed to take advantage of the bending-twisting coupling, for example, for load mitigation in wind turbines (Lobitz & Veers, 2003; Bottasso *et al.*, 2013). Passive strategies just depending on blade geometry and material properties could a priori be addressed in future with the present method.

Application for new rotor configurations

The numerical methodology developed in this work could be adapted to describe other situations related with rotor wakes. For example, it could be interesting to consider the case of two co-rotative vortices emitted from the blade which may occur when the blade exhibits a flap or some additional devices. For this case, a helical braid is expected to be created downstream that can be treated numerically in the same way that solutions obtained in the present work.

Appendices

Appendix A

Numerical methodology

In this appendix, the details of calculation of the different steps of the model are presented.

I) Far-wake solutions

– Parameters: R^* , h^* , α , ε

1. Calculation of the non-dimensional axial period $L^* = L/R_{\text{ext}}$:

$$L^* = \frac{h^*}{N|1/\alpha - \kappa|} \quad (\text{A.1})$$

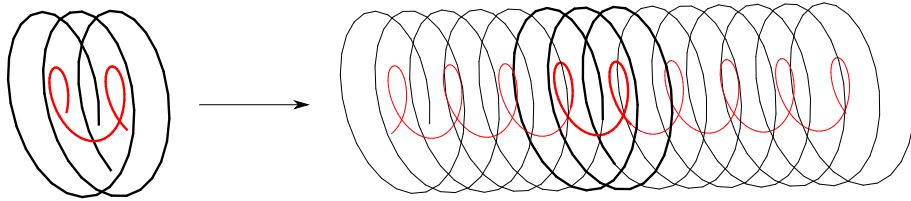
2. Discretization of the non-dimensional axial coordinate in n equispaced elements: $z_k = kL^*/n$ for $k = \{0, \dots, n\}$. The value of n is typically chosen to have a minimum of n_t elements per turn of helix: $n = \text{ceil}(n_t L^*/h^*)$ if $\alpha > 1$ and $n = \text{ceil}(n_t L^*/\alpha h^*)$ if $\alpha < 1$. $n_t = 25$ is typically chosen.

The position of a point k of the vortex j is defined by its cylindrical coordinates: $\xi_k^j = (r_k^j, \phi_k^j, z_k^j)$.

3. Definition of the initial guess structure as two perfect helices along the discretized axial coordinate:

$$r_k^{\text{ext}} = 1, \quad r_k^{\text{int}} = R^*, \quad \phi_k^{\text{ext}} = 2\pi z_k/h^*, \quad \phi_k^{\text{int}} = 2\pi z_k/\alpha h^*. \quad (\text{A.2})$$

4. Construction of the infinite structure by repeating one-period structures:



Typically, the period is repeated at least 7 times from each side, giving an extended structure of $n_T = 7(n - 1) + 1$ elements.

5. Computation of the induced velocity $\mathbf{U}_k^{\text{ind}}$ at each point k as explained in section 2.3.1. First, the induction of the discretized vortices is obtained by adding the contribution of every segment of all the discretized extended structures, including external and internal vortices. The induction of a single segment between points $\{m, m + 1\}$ of vortex i on the point k of vortex j is computed through the discretized Biot-Savat formula:

$$\mathbf{U}_{i,m}^{\text{seg}}(\boldsymbol{\xi}_k^j) = \frac{\Gamma_i}{4\pi} \frac{((1 - |\mathbf{r}_{i,m}^{j,k}|^2)|\mathbf{r}_{i,m}^{j,k}| + (1 - |\mathbf{r}_{i,m+1}^{j,k}|^2)|\mathbf{r}_{i,m+1}^{j,k}|)(\mathbf{r}_{i,m}^{j,k} \times \mathbf{r}_{i,m+1}^{j,k})\mathbf{r}_{i,m}^{j,k} \cdot \mathbf{r}_{i,m+1}^{j,k}}{((\mathbf{r}_{i,m}^{j,k} \cdot \mathbf{r}_{i,m+1}^{j,k})^2 - |\mathbf{r}_{i,m}^{j,k}|^2|\mathbf{r}_{i,m+1}^{j,k}|^2)|\mathbf{r}_{i,m}^{j,k}||\mathbf{r}_{i,m+1}^{j,k}|}, \quad (\text{A.3})$$

where $\mathbf{r}_{i,m}^{j,k}$ is the vector from point m of vortex i to point k of vortex j .

Then, the contribution of the curved section of vortex between the two adjacent points $k - 1$ and $k + 1$ is computed:

$$\mathbf{U}_{j,k}^{\text{loc}} = \frac{\Gamma_j}{4\pi\rho_j^k} \ln\left(\frac{\Delta\phi_j^k\rho_j^k}{\delta a}\right) \mathbf{b}_j^k. \quad (\text{A.4})$$

Finally, the total induced velocity on point k of vortex j is obtained by:

$$\mathbf{U}^{\text{ind}}(\boldsymbol{\xi}_k^j) = \mathbf{U}_{j,k}^{\text{loc}} + \sum_{m=1}^{n_T} \mathbf{U}_{\text{ext},m}^{\text{seg}}(\boldsymbol{\xi}_k^j) + \sum_{m=1}^{n_T} \mathbf{U}_{\text{int},m}^{\text{seg}}(\boldsymbol{\xi}_k^j) \quad (\text{A.5})$$

6. Induced velocities distributions are used to compute moving frame velocities W_F and Ω_F by solving

$$\frac{2\pi}{\alpha N|1/\alpha - \kappa|} = \int_0^{L^*} \frac{\tilde{\Omega}^{\text{int}} - \tilde{\Omega}_F}{\tilde{V}_z^{\text{int}} - \tilde{W}_F} dz, \quad (\text{A.6a})$$

$$\frac{2\pi h^*}{N|1/\alpha - \kappa|} = \int_0^{L^*} \frac{\tilde{\Omega}^{\text{ext}} - \tilde{\Omega}_F}{\tilde{V}_z^{\text{ext}} - \tilde{W}_F} dz, \quad (\text{A.6b})$$

where \tilde{V}_z^j and $\tilde{\Omega}^j$ are the induced axial velocity and rotation normalized by NT/R_{ext} and NT/R_{ext}^2 respectively; the same normalization is used for \tilde{W}_F and $\tilde{\Omega}_F$. These two equations are solved using a Newton-Raphson method. To integrate, a trapezoidal rule is employed. Initial guess values for the numerical resolution are obtained by:

$$\tilde{\Omega}_F^0 = \frac{1}{h^*(1 - \alpha)} \int_0^{L^*} \left[2\pi(\tilde{V}_z^{\text{int}} - \tilde{V}_z^{\text{ext}}) + h^*(\tilde{\Omega}^{\text{ext}} - \alpha\tilde{\Omega}^{\text{int}}) \right] dz, \quad (\text{A.7a})$$

$$\tilde{W}_F^0 = \int_0^{L^*} \left[\tilde{V}_z^{\text{ext}} + \frac{h^*}{2\pi}(\tilde{\Omega}_F^0 - \tilde{\Omega}^{\text{ext}}) \right] dz. \quad (\text{A.7b})$$

7. Radial and azimuthal coordinates of the deformed helical structure are calculated from equations

$$\frac{dr}{dz} = \frac{\tilde{V}_r}{\tilde{V}_z - \tilde{W}_F}, \quad \frac{d\phi}{dz} = \frac{\tilde{\Omega} - \tilde{\Omega}_F}{\tilde{V}_z - \tilde{W}_F}. \quad (\text{A.8})$$

Which are discretized by a finite difference scheme:

$$\begin{bmatrix} D_z & 0 & 0 & 0 \\ 0 & D_z & 0 & 0 \\ 0 & 0 & D_z & 0 \\ 0 & 0 & 0 & D_z \end{bmatrix} \begin{bmatrix} \mathbf{r}^{\text{ext}} \\ \mathbf{r}^{\text{int}} \\ \boldsymbol{\phi}^{\text{ext}} \\ \boldsymbol{\phi}^{\text{int}} \end{bmatrix} = \begin{bmatrix} \tilde{\mathbf{V}}_r^{\text{ext}} / (\tilde{\mathbf{V}}_z^{\text{ext}} - \tilde{W}_F) \\ \tilde{\mathbf{V}}_r^{\text{int}} / (\tilde{\mathbf{V}}_z^{\text{int}} - \tilde{W}_F) \\ (\tilde{\boldsymbol{\Omega}}^{\text{ext}} - \tilde{\boldsymbol{\Omega}}) / (\tilde{\mathbf{V}}_z^{\text{ext}} - \tilde{W}_F) \\ (\tilde{\boldsymbol{\Omega}}^{\text{int}} - \tilde{\boldsymbol{\Omega}}) / (\tilde{\mathbf{V}}_z^{\text{int}} - \tilde{W}_F) \end{bmatrix}, \quad (\text{A.9})$$

where \mathbf{r} and $\boldsymbol{\phi}$ are column vectors of $n + 1$ elements with the radial and azimuthal position of the vortices at each discrete axial position z_k . $\tilde{\mathbf{V}}_r$, $\tilde{\mathbf{V}}_z$ and $\tilde{\boldsymbol{\Omega}}$ are column vectors with non-dimensionalized induced velocities and rotation. D_z ($n + 1$ square matrix) is the first derivative discretization matrix with respect to z :

$$(D_z \mathbf{r}^{\text{ext}})_k = \frac{r_k^{\text{ext}} - r_{k-1}^{\text{ext}}}{\Delta z}, \quad (\text{A.10})$$

where $\Delta z = L^*/n$. Dirichlet conditions are applied on the first element of the position vectors:

$$r_0^{\text{ext}} = 1, \quad r_0^{\text{int}} = R^*, \quad \phi_0^{\text{ext}} = 0, \quad \phi_0^{\text{int}} = 0. \quad (\text{A.11})$$

As induced and frame velocities depend on the geometry of the vortices, the system is coupled. It is solved with Matlab software. Particularly, function `fsolve` is used.

When several blades are considered ($N > 1$), the resolution process does not change. The $2\pi/N$ azimuthal periodicity is imposed. It is just necessary to include the induction effect of the discretized segments of the other vortices by applying Biot-Savart formula (A.3).

II) Near-wake solutions

– Parameters: R_b^* , λ , η , ε

1. Choose of the number of turns of the computation domain n_{NW} , the number of turns of the far-wake domain n_{FW} and the number of discretization elements per turn n_t . So the total number of elements per vortex in the computation domain will be $n = n_{NW} \times n_t$. The far-wake structure is not included in the computation domain.
2. Discretization of the azimuthal coordinate in n equispaced elements: $\phi_k = 2\pi k/n_t$ for $k = \{0, \dots, n\}$. Typically a value of $n_t = 25$ is chosen. The minimum number of computation turns n_{NW} depends on the rotor regime: more complex regimes as VRS will need a higher number of turns to stabilize to a regular structure away from the rotor. We typically choose $n_{FW} = n_{NW} = 15$, except for high tip-speed-ratio wind turbine regimes, where the number of turns is augmented to 30.
3. Definition of the initial guess structure as two perfect helical vortices advected by the external flow:

$$r_k^{\text{tip}} = 1, \quad r_k^{\text{hub}} = R_b^*, \quad z_k^{\text{tip}} = z_k^{\text{hub}} = \phi_k/\lambda \quad (\text{A.12})$$

4. Computation of the induced velocity as explained before in section A.I.5, including the contribution of the discretized segments and the local curved vortex section.

To complete the computation of the induced velocity \mathbf{U}^{ind} , the contribution of the far-wake has to be added. For that, a far-wake structure is calculated as in section A.I., taking as geometric parameters:

$$\begin{aligned} R^* &= r_n^{\text{hub}}/r_n^{\text{tip}}, & h^* &= (z_n^{\text{tip}} - z_{n-n_t}^{\text{tip}})/r_n^{\text{tip}}, \\ \alpha &= (z_n^{\text{hub}} - z_{n-n_t}^{\text{hub}})/(z_n^{\text{tip}} - z_{n-n_t}^{\text{tip}}), & \varepsilon^* &= \varepsilon R^{\text{tip}}/r_n^{\text{tip}}. \end{aligned} \quad (\text{A.13})$$

Then, the induced velocity of the far-wake structure is computed on the point k using discretized Biot-Savart formula (A.3) and including the effect of every segment of internal and external vortices of the far-wake structure:

$$\mathbf{U}_{\text{FW}}^{\text{ind}}(\boldsymbol{\xi}_k^j) = \sum_{m=1}^{n_{\text{FW}}} \mathbf{U}_{\text{extFW},m}^{\text{seg}}(\boldsymbol{\xi}_k^j) + \sum_{m=1}^{n_{\text{FW}}} \mathbf{U}_{\text{intFW},m}^{\text{seg}}(\boldsymbol{\xi}_k^j) \quad (\text{A.14})$$

A simpler way to estimate the effect of the far-wake is to consider the far-wake structure as perfect helices of constant pitch and radius instead of computing the deformed structures. The difference on the induced flow contribution $\mathbf{U}_{\text{FW}}^{\text{ind}}$ is small and it does not have an important effect on the near-wake geometry, on the contrary, computation time is noticeably reduced.

5. The coordinates of the position of the vortices are computed as in section A.I through the following discretized system:

$$\begin{bmatrix} D_\phi & 0 & 0 & 0 \\ 0 & D_\phi & 0 & 0 \\ 0 & 0 & D_\phi & 0 \\ 0 & 0 & 0 & D_\phi \end{bmatrix} \begin{bmatrix} \mathbf{r}^{\text{tip}} \\ \mathbf{r}^{\text{hub}} \\ \mathbf{z}^{\text{tip}} \\ \mathbf{z}^{\text{hub}} \end{bmatrix} = \begin{bmatrix} \eta \tilde{\mathbf{V}}_r^{\text{tip}} / (\eta \tilde{\Omega}^{\text{tip}} - 1) \\ \eta \tilde{\mathbf{V}}_r^{\text{hub}} / (\eta \tilde{\Omega}^{\text{hub}} - 1) \\ (\eta \tilde{\mathbf{V}}_z^{\text{tip}} + 1/\lambda) / (\eta \tilde{\Omega}^{\text{tip}} - 1) \\ (\eta \tilde{\mathbf{V}}_z^{\text{hub}} + 1/\lambda) / (\eta \tilde{\Omega}^{\text{hub}} - 1) \end{bmatrix}. \quad (\text{A.15})$$

Discretization matrix D_ϕ has the same structure as D_z in section A.I with a discretization step $\Delta\phi = n_t/2\pi$. The boundary conditions at the rotor are

$$r_0^{\text{ext}} = 1, \quad r_0^{\text{int}} = R_b^*, \quad z_0^{\text{ext}} = 0, \quad z_0^{\text{int}} = 0. \quad (\text{A.16})$$

For standard Joukowski model, the same process is followed. Parameters R_b^* and α disappear and system (A.15) is reduced to \mathbf{r}^{tip} and \mathbf{z}^{tip} variables. The induction of the straight hub vortex is computed with Biot-Savart formula (2.3). As occurs for generalized far-wake solutions, when several blades are considered ($N > 1$), the same process is followed, just the induction effects of the other vortices have to be considered to compute induced velocities.

III) Rigid blades

– Parameters: $c(r)$, $\beta(r)$, $C_L(\alpha, r)$; λ , ε

1. Guess initial values of Γ , R_{tip} and R_{hub} . Normally, a good guess for tip vortex is $R_{\text{tip}} = 1$. For Γ and R_{hub} , it depends on the blade geometry.

2. Compute the wake geometry as in section A.II taking

$$R_b^* = R_{\text{hub}}/R_{\text{tip}}, \quad \eta = \Gamma/\Omega R R_{\text{tip}}^2, \quad \varepsilon^* = \varepsilon R/R_{\text{tip}}. \quad (\text{A.17})$$

3. With the wake structure obtained in previous point, compute the induced velocity on the blades:

$$\bar{\mathbf{V}}^{\text{ind}}(r) = \frac{1}{2\pi} \int_0^{2\pi} \mathbf{U}_R^{\text{ind}}(r, \theta) d\theta, \quad (\text{A.18})$$

where $\mathbf{U}_R^{\text{ind}}(r, \theta)$ is the induced velocity on the rotor plane, computed from the contribution of all the segments of the discretized wake with Biot-Savart formula A.3. Velocities are normalized by $N\Gamma/R$. Then, local velocity $U(r)$ and angle of attack $\alpha(r)$ are computed

$$U(r) = \sqrt{(1/\lambda + \eta \bar{V}_z^{\text{ind}}(r))^2 + r^2(\eta \bar{\Omega}^{\text{ind}}(r) - 1)^2}, \quad (\text{A.19})$$

$$\alpha(r) = \beta(r) - \phi(r) = \beta(r) - \arctan\left(\frac{1/\lambda + \eta \bar{V}_z^{\text{ind}}(r)}{r(\eta \bar{\Omega}^{\text{ind}}(r) - 1)}\right). \quad (\text{A.20})$$

With this distribution of α , we obtain lift coefficient distribution $C_L(r)$ by interpolating the airfoil data $C_L(\alpha)$.

4. Compute circulation profile $\bar{\Gamma}(r)$ with tip correction F :

$$\bar{\Gamma}(r) = \frac{1}{2} c(r) U(r) C_L(\alpha; r) F, \quad (\text{A.21})$$

$$F = \frac{2}{\pi} \arccos\left[\exp\left(-\frac{N(1-r)}{2r \sin \phi}\right)\right]. \quad (\text{A.22})$$

5. From $\bar{\Gamma}(r)$ distribution, compute R_{tip} , R_{hub} and Γ :

$$\Gamma = \max(\bar{\Gamma}(r)), \quad (\text{A.23})$$

$$R_{\text{hub}} = \frac{\int_0^{r(\Gamma)} r \frac{d\bar{\Gamma}}{dr} dr}{\int_0^{r(\Gamma)} \frac{d\bar{\Gamma}}{dr} dr}, \quad R_{\text{tip}} = \frac{\int_{r(\Gamma)}^R r \frac{d\bar{\Gamma}}{dr} dr}{\int_{r(\Gamma)}^R \frac{d\bar{\Gamma}}{dr} dr}, \quad (\text{A.24})$$

6. Iterate from points 2 to 5 until the relative variation of Γ , R_{tip} and R_{hub} is lower than 10^{-4} :

$$\frac{|\Gamma^{q+1} - \Gamma^q|}{|\Gamma^q|} < 10^{-4}, \quad (\text{A.25})$$

where q is the iteration number.

IV) Deformed blades

- Parameters: $c(r)$, $c'(r)$, $c''(r)$, $\beta(r)$, A^* , I^* , J^* , $C_L(\alpha, r)$, $C_D(\alpha, r)$; λ , ε ; ρ_b^* , E , ν
- 1. Discretize the blade in the local span coordinate s in n_b elements: $s_k = k/n_b$ for $k = \{0, \dots, n_b\}$. Initially, the blade is assumed undeformed, so bending and twisting angles are $\theta_k = 0$ and $\gamma_k = 0$.

The deformed blade position is described by $\xi_b(s) \equiv \{r_b(s), \phi_b(s), z_b(s)\}$.

2. Compute the wake structure and its induction on the rotor assuming rigid blades. Follow the algorithm of section A.III.
3. Compute circulation distribution $\bar{\Gamma}(s)$ and calculate the vortex strength $\eta = \Gamma/\Omega_R R_b^2$ and the position of the vortices on the blade s_{tip} and s_{hub} . This is computed with (A.21-24) replacing r by blade span coordinate s .
4. Compute force terms associated with bending and twisting:

$$F_\theta = \frac{1}{2}c^*U^{*2}(C_L(\alpha) \cos \alpha + C_D(\alpha) \sin \alpha) - \rho_b^*A^*c^{*2} \left[\int_0^s \cos \theta ds \right] \sin \theta - \frac{\rho_b^*A^*c^{*2}}{\text{Fr}^2} \cos \theta \sin(\beta + \gamma), \quad (\text{A.26})$$

$$F_\gamma = \frac{1}{2}c^{*2}U^{*2} [(C_L(\alpha) \cos \alpha + C_D(\alpha) \sin \alpha)\delta_{\text{cm}}^{\text{ac}} + C_{\text{m,ac}}(\alpha)], \quad (\text{A.27})$$

where $\delta_{\text{cm}}^{\text{ac}}$ is calculated as the distance, normalized by c , between the center of mass of the airfoil and the aerodynamic center (at a distance of $c/4$ from the leading edge). $C_{\text{m,ac}}(\alpha)$ is the pitching moment coefficient, to be extracted from an airfoil database as Abbott & Von Doenhoff (1960). For symmetric profiles, $C_{\text{m,ac}}(\alpha) = 0$.

5. Obtain bending $\theta(s)$ and twist $\gamma(s)$ angles by solving the beam model equations (5.14) and (5.15) discretized with a finite difference scheme:

$$c_k^{*4} \left[\frac{\theta_{k+2} - 3\theta_{k+1} + 3\theta_k - \theta_{k-1}}{\Delta s^3} \right] + 8c_k^{*'}c_k^{*3} \left[\frac{\theta_{k+1} - 2\theta_k + \theta_{k-1}}{\Delta s^2} \right] + 4(3c_k^{*'}c_k^{*2} + c_k^{*''}c_k^{*3}) \left[\frac{\theta_{k+1} - \theta_k}{\Delta s} \right] = \frac{\text{Fr}^2}{\rho_b^*EI^*} F_\theta(s_k), \quad (\text{A.28})$$

$$c_k^{*4} \left[\frac{\gamma_{k+1} - 2\gamma_k + \gamma_{k-1}}{\Delta s^2} \right] + 4c_k^{*3}c_k^{*'} \left[\frac{\gamma_{k+1} - \gamma_{k-1}}{2\Delta s} \right] = \frac{2(1+\nu)\text{Fr}^2}{\rho_b^*EJ^*} F_\gamma(s_k). \quad (\text{A.29})$$

Note that F_θ and F_γ are computed from θ and γ distributions from the previous iteration, so the system is linear and completely uncoupled. Just the boundary conditions have to be included:

$$\theta_0 = 0, \quad \frac{\theta_{n_b+1} - \theta_{n_b}}{\Delta s} = 0, \quad \frac{\theta_{n_b+2} - \theta_{n_b+1} + \theta_{n_b}}{\Delta s^2} = 0, \quad (\text{A.30})$$

$$\gamma_0 = 0, \quad \frac{\gamma_{n_b+1} - \gamma_{n_b-1}}{\Delta s} = 0,$$

6. Compute a new wake geometry using as boundary conditions the emission points of the vortices in the deformed blade:

$$r_0^{\text{ext}} = r_b(s_{\text{tip}}), \quad r_0^{\text{int}} = r_b(s_{\text{hub}}), \quad z_0^{\text{ext}} = z_b(s_{\text{tip}}), \quad z_0^{\text{int}} = z_b(s_{\text{hub}}), \quad (\text{A.31})$$

where $r_b(s)$ and $z_b(s)$ are computed from $\theta(s)$ and $\gamma(s)$ as

$$r_b(s) = \int_0^s \cos(\theta(\tilde{s})) d\tilde{s}, \quad z_b(s) = \int_0^s \cos(\beta(\tilde{s}) - \gamma(\tilde{s})) \sin(\theta(\tilde{s})) d\tilde{s} \quad (\text{A.32})$$

The vortices are assumed to shed from the same azimuthal position. This simplifies the model and, as the induced velocity on the blades is azimuthally averaged, it does not imply a big difference on the solution.

7. Compute the induced velocity on the blades along the span coordinate s

$$\bar{\mathbf{V}}^{\text{ind}}(s) = \frac{1}{2\pi} \int_0^{2\pi} \mathbf{U}^{\text{ind}}(r_b(s), z_b(s); \phi) d\phi, \quad (\text{A.33})$$

where velocities are normalized by $N\Gamma/R_b$. Then, local velocity $U(s)$ and angle of attack $\alpha(s)$ are computed:

$$U(s) = \sqrt{(1/\lambda + \eta \bar{V}_z^{\text{ind}}(s))^2 + r_b^2(s)(\eta \bar{\Omega}^{\text{ind}}(s) - 1)^2}, \quad (\text{A.34})$$

$$\alpha(s) = \beta(s) - \phi(s) - \gamma(s) = \beta(r) - \arctan\left(\frac{1/\lambda + \eta \bar{V}_z^{\text{ind}}(s)}{r_b(s)(\eta \bar{\Omega}^{\text{ind}}(s) - 1)}\right) - \gamma(s). \quad (\text{A.35})$$

With this distribution of α , we obtain lift and drag coefficients distribution $C_L(s)$ and $C_D(s)$ by interpolating the airfoil data $C_L(\alpha)$ and $C_D(\alpha)$.

8. Compute a new circulation distribution $\bar{\Gamma}(s)$ and calculate vortex strength Γ and the new position of the vortices on the blade s_{tip} and s_{hub} .
9. Iterate from point 4 to 8 until convergence of the blade deformation

$$\frac{\|\gamma^{q+1} - \gamma^q\|}{\|\gamma^q\|}, \quad \frac{\|\theta^{q+1} - \theta^q\|}{\|\theta^q\|} < 10^{-4}. \quad (\text{A.36})$$

Bibliography

- ABBOTT, I. & VON DOENHOFF, A. 1960 *Theory of wing sections*. Dover Publications.
- BAUCHAU, O. & CRAIG, J. 2009 *Structural Analysis. Solid Mechanics and Its Applications*. Springer.
- BAZILEVS, Y., HSU, M.-C., AKKERMAN, I., WRIGHT, S., TAKIZAWA, K., HENICKE, B., SPIELMAN, T. & TEZDUYAR, T. E. 2011 3D simulation of wind turbine rotors at full scale. Part I: Geometry modeling and aerodynamics. *Int. J. Numer. Meth. Fluids* **65**, 207–235.
- BENHAM, P. & CRAWFORD, R. 1976 *Mechanics of Engineering Materials*. Longman.
- BETCHOV, R. 1965 On the curvature and torsion of an isolated vortex filament. *J. Fluid Mech.* **22**, 471–479.
- BETZ, A. 1920 *Das maximum der theoretisch möglichen ausnützung des windes durch windmotoren*. Zeitschrift das gesamte Turbinewessen.
- BETZ, A. 1926 *Windenergie und ihre Ausnützung durch Windmühlen*. Göttingen: Vandenhoeck und Ruprecht.
- BHAGWAT, M. J. & LEISHMAN, J. G. 2000 Stability analysis of helicopter rotor wakes in axial flight. *J. Amer. Helic. Soc.* **45**, 165–178.
- BLANCO-RODRÍGUEZ, F. J. & LE DIZÈS, S. 2016 Elliptic instability of a curved Batchelor vortex. *J. Fluid Mech.* **804**, 224–247.
- BLANCO-RODRÍGUEZ, F. J. & LE DIZÈS, S. 2017 Curvature instability of a curved Batchelor vortex. *J. Fluid Mech.* **814**, 397–415.
- BLANCO-RODRÍGUEZ, F. J., LE DIZÈS, S., SELÇUK, C., DELBENDE, I. & ROSSI, M. 2015 Internal structure of vortex rings and helical vortices. *J. Fluid Mech.* **785**, 219–247.
- BLISS, D. B. 1993 New vortex dynamics methods for rotor free wake analysis. technical report ARO-25747. *Tech. Rep.*. Durham, USA.
- BOERSMA, J. & WOOD, D. H. 1999 On the self-induced motion of a helical vortex. *J. Fluid Mech.* **384**, 263–280.

- BOLNOT, H., LE DIZÈS, S. & LEWEKE, T. 2014 Spatio-temporal development of the pairing instability in an infinite array of vortex rings. *Fluid Dyn. Research* **46**, 061405.
- DE BOTHEZAT, L. 1919 The general theory of blade screws. tr 29. *Tech. Rep.*. NACA.
- BOTTASSO, C. L., CAMPAGNOLO, F., CROCE, A. & TIBALDI, C. 2013 Optimization-based study of bend-twist coupled rotor blades for passive and integrated passive/active load alleviation. *Wind Energy* **16(8)**, 1149–1166.
- BRAMWELL, A. R. S. 1976 *Helicopter Dynamics*. Edward Arnold, London.
- BRYNJELL-RAHKOLA, M. & HENNINGSON, D. S. 2017 A note on the numerical realization of helical vortices: application to vortex instability. *Tech. Rep.*. Department of Mechanics, Royal Institute of Technology, KTH.
- CARADONNA, F. X. & TUNG, C. 1981 Experimental and analytical studies of a model helicopter rotor in hover (TM 81232). *Tech. Rep.*. NASA.
- CARR, L. W. 1988 Progress in analysis and prediction of dynamic stall. *J. Aircraft* **25**, 6–17.
- CARRERA, E., GIUNTA, G. & PETROLO, M. 1926 *Beam structure: classical and advanced theories*. Wiley & Sons.
- CARRION, M., WOODGATE, M., STEIJL, R. & BARAKOS, G. 2015 Understanding wind-turbine wake breakdown using computational fluid dynamics. *AIAA Journal* **53(3)**.
- CHRITZOS, C. C., HEYSON, H. H. & BOSWINKLE, R. W. 1955 *Aerodynamic characteristics of NACA 0012 airfoil section at angles of attack from 0° to 180°*. National Advisory Committee for Aeronautics.
- CROW, S. C. 1970 Stability theory for a pair of trailing vortices. *AIAA J.* **8** (12), 2172–2179.
- DA RIOS, L. S. 1916 Vortici ad elica. *Il Nuovo Cimento* **11**, 419–431.
- DIAS, M. A. & AUDOLY, B. 2014 A non-linear rod model for folded elastic strips. *Journal of the Mechanics and Physics of Solids* **62**, 57–80.
- DIAS, M. A. & AUDOLY, B. 2015 Wunderlich, meet Kirchhoff: A general and unified description of elastic ribbons and thin rods. *J. Elast* **119**, 49–66.
- DOWELL, E. H. & HALL, K. C. 2001 Modeling of fluid-structure interaction. *Annual Review of Fluid Mechanics* **33** (1), 445–490.
- DREES, J. M. & HENDAL, W. P. 1951 The field of flow through a helicopter rotor obtained from wind tunnel smoke tests. *J. Aircraft Eng.* **23**, 107–111.
- DRZEWIECKI, S. 1920 *Théorie Générale de l'Hélice*. Paris.

- DURÁN VENEGAS, E. & LE DIZÈS, S. 2018 Structure and stability of rotor generated vortices. In *European Fluid Mechanics Conference 12*.
- DURÁN VENEGAS, E. & LE DIZÈS, S. 2019 Generalized helical vortex pairs. *J. Fluid Mech.* **865**, 523 – 545.
- DURÁN VENEGAS, E., LE DIZÈS, S. & ELOY, C. 2019 A strongly-coupled model for flexible rotors. *J. Fluids Struct.* .
- ELOY, C., SOUILLIEZ, C. & SCHOUVEILER, L. 2007 Flutter of a rectangular plate. *J. Fluids Struct.* **23**, 904–919.
- FROUDE, R. 1889 On the part played in propulsion by difference of fluid pressure. *Trans. Inst. Naval Arch.* **30**, 390–405.
- FROUDE, W. 1878 On the elementary relation between pitch, slip and propulsive efficiency. *Trans. Inst. Naval Arch.* **19**, 22–33.
- FUKUMOTO, Y. & HATTORI, Y. 2005 Curvature instability of a vortex ring. *J. Fluid Mech.* **526**, 77–115.
- FUKUMOTO, Y. & MIYAZAKI, T. 1991 Three-dimensional distortions of a vortex filament with axial velocity. *J. Fluid Mech.* **222**, 369–416.
- FUKUMOTO, Y. & OKULOV, V. L. 2005 The velocity induced by a helical vortex tube. *Phys. Fluids* **17**, 107101.
- FUKUMOTO, Y., OKULOV, V. L. & WOOD, D. 2015 The contribution of Kawada to the analytical solution for the velocity induced by a helical vortex filament. *Appl. Mech. Rev* **67** (6), 467–486.
- GERE, J. & TIMOSHENKO, S. 1998 *Mechanics of Materials*. International Thomson editors.
- GESSOW, A. & GUSTAFSON, F. B. 1948 Effect of rotor-blade twist and plan-form taper on helicopter hovering performance. tn 1542. *Tech. Rep.*. NACA.
- GLAUERT, H. 1922 An aerodynamic theory of the airscrew. *ARC R & M* **786**.
- GLAUERT, H. 1926 The effect of compressibility on the lift of an aerofoil. *Cambridge University Press, London* .
- GLAUERT, H. 1935 *Airplane propellers. Division L.*. Springer.
- GOLDSTEIN, M. A. 1929 On the vortex theory of screw propellers. *Proc. R. Soc. Lond.* A **123**, 440–465.
- GRAY, R. B. 1956 An aerodynamic analysis of a single-bladed rotor in hovering and low speed forward flight as determined from smoke studies of the vorticity distribution in the wake. Technical Report 356. *Tech. Rep.*. Princeton University, USA.

- GUPTA, B. P. & LOEWY, R. G. 1974 Theoretical analysis of the aerodynamic stability of multiple, interdigitated helical vortices. *AIAA J.* **12**, 1381–1387.
- GUPTA, S. & LEISHMAN, J. G. 2005*a* Accuracy of the induced velocity from helical vortices using straight-line segmentation. *AIAA J.* **43**, 29–40.
- GUPTA, S. & LEISHMAN, J. G. 2005*b* Comparison of momentum and vortex methods for the aerodynamic analysis of wind turbine. *AIAA Paper* p. 594.
- GUSTAFSON, F. B. & GESSOW, A. 1946 Effect of rotor tip speed on helicopter rotor performance and maximum forward speed. naca arr no. 16a16. *Tech. Rep.*. NACA.
- HAN, S., BENAROYA, H. & WEI, T. 1999 Dynamics of transversely vibrating beams using four engineering theories. *Journal of Sound and Vibration* **225**, 935–988.
- HAND, H., SIMMS, D., FINGERSH, L., JAGER, D., COTRELL, J., SCHRECK, S. & LARWOOD, S. 2001 Unsteady Aerodynamics Experiment Phase VI: Wind tunnel test configurations and available data campaigns. *Tech. Rep.*. NREL/TP-500- 29955.
- HANSEN, M. O. L. 2015 *Aerodynamics of wind turbines*, 3rd edn. Routledge.
- HANSEN, M. O. L., SORENSEN, J. N., VOUTSINAS, S., SORENSEN, N. & MADSEN, H. A. 2006 State of the art in wind turbine aerodynamics and aeroelasticity. *Progr. Aerosp. Sci.* **42**, 285–330.
- HARDIN, J. C. 1982 The velocity field induced by a helical vortex filament. *Phys. Fluids* **25**, 1949–52.
- HATTORI, Y. & FUKUMOTO, Y. 2009 Short-wavelength stability analysis of a helical vortex tube. *Phys. Fluids* **21**, 014104.
- HATTORI, Y. & FUKUMOTO, Y. 2014 Modal stability analysis of a helical vortex tube with axial flow. *J. Fluid Mech.* **738**, 222–249.
- HUERRE, P. & MONKEWITZ, P. A. 1985 Absolute and convective instabilities in free shear layers. *J. Fluid Mech.* **159**, 151–168.
- HUERRE, P. & MONKEWITZ, P. A. 1990 Local and global instabilities in spatially developing flows. *Annu. Rev. Fluid Mech.* **22**, 473–537.
- IVANELL, S., MIKKELSEN, R., SORENSEN, J. & HENNINGSON, D. 2010 Stability analysis of the tip vortices of a wind turbine. *Wind Energ.* **13**, 705–715.
- JACOBS, E. N., WARD, K. E. & PINKERTON, R. M. 1935 The characteristics of 78 related airfoils sections from tests in the variable-density wind tunnel. *Tech. Rep.*. NACA.
- JOHNSON, W. 1980 *Helicopter Theory*. Princeton University Press.
- JOUKOWSKI, N. 1929 *Théorie tourbillonnaire de l'hélice propulsive*. Gauthier-Villars.

- KATZ, J. & PLOTKIN, A. 1991 *Low-Speed Aerodynamics: from wing theory to panel methods*. Mc Graw-Hill.
- KAWADA, S. 1936 Induced velocity by helical vortices. *J. Aero. Sci.* **3** (3), 86–87.
- KELVIN, L. 1880 Vibrations of a columnar vortex. *Phil. Mag.* **10**, 155–168.
- KERSWELL, R. R. 2002 Elliptical instability. *Annu. Rev. Fluid Mech.* **34**, 83–113.
- KIDA, S. 1981 A vortex filament moving without change of form. *J. Fluid Mech.* **112**, 397–409.
- KIDA, S. 1982 Stability of a steady vortex filament. *J. Phys. Soc. Japan* **51**, 1655–1662.
- KLEIN, R., MAJDA, A. J. & DAMODARAN, K. 1995 Simplified equations for the interaction of nearly parallel vortex filaments. *J. Fluid Mech.* **288**, 201–248.
- KNIGHT, M. & HEFNER, R. 1937 Static thrust of the lifting airscrew. *Tech. Rep.*. NACA TN 626.
- KUETHE, A. & CHOW, C. 1976 *Foundations of Aerodynamics*. Wiley.
- KUIBIN, P. A. & OKULOV, V. L. 1998 Self-induced motion and asymptotic expansion of the velocity field in the vicinity of a helical vortex filament. *Phys. Fluids* **10**, 607–614.
- KWIECINSKI, J. A. & VAN GORDER, R. A. 2018 Dynamics of nearly parallel interacting vortex filaments. *J. Fluid Mech.* **835**, 575–623.
- LEISHMAN, J. G. 2006 *Principles of Helicopter Aerodynamics*. Cambridge University Press.
- LEISHMAN, J. G., BHAGWAT, M. J. & ANANTHAN, S. 2004 The vortex ring state as a spatially and temporally developing wake instability. *J. Am. Helicopter Soc.* **49**, 160–175.
- LEISHMAN, J. G., BHAGWAT, M. J. & BAGAI, A. 2002 Free-vortex filament methods for the analysis of helicopter rotor wakes. *J. Aircraft* **39**, 759–775.
- LEVY, H. & FORSDYKE, A. G. 1927 The stability of an infinite system of circular vortices. *Proc. R. Soc. Lond. A* **114**, 594–604.
- LEVY, H. & FORSDYKE, A. G. 1928 The steady motion and stability of a helical vortex. *Proc. R. Soc. Lond. A* **120**, 670–690.
- LEWEKE, T., LE DIZÈS, S. & WILLIAMSON, C. H. K. 2016 Dynamics and instabilities of vortex pairs. *Annu. Rev. Fluid Mech.* **48**, 507–541.
- LEWEKE, T., QUARANTA, H. U., BOLNOT, H., BLANCO-RODRÍGUEZ, F. J. & LE DIZÈS, S. 2014 Long- and short-wave instabilities in helical vortices. *J. Phys.: Conf. Ser.* **524**, 012154.

- LOBITZ, D. & VEERS, P. S. 2003 Load mitigation with bending/twist coupled blades on rotors using modern control strategies. *Wind Energy* **6.2**, 105–117.
- LOCK, C., BATEMAN, H. & TOWNEND, H. 1925 An extension of the vortex theory of airscrews with applications to airscrews of small pitch and including experimental results. *Aeronautical Research Committee. Reports and Memoranda* **1014**.
- LUCAS, D. & DRITSCHEL, D. G. 2009 A family of helically symmetric vortex equilibria. *J. Fluid Mech.* **634**, 245–268.
- LV, P., MOHD-ZAWAWI, F., BENARD, E., PROTHIN, S., MOSCHETTA, J. M. & MORLIER, J. 2013 An application of adaptive blades on convertible mavs. *International Journal of Micro Air Vehicles* **5 (4)**, 229 – 243.
- MAHERI, A. & ISIKVEREN, A. T. 2010 Performance prediction of wind turbines utilizing passive smart blades: approaches and evaluation. *Wind Energy* **13(2–3)**, 255–265.
- MULLERNERS, K. & RAFFEL, M. 2012 The onset of dynamic stall revisited. *Exp. Fluids* **52**, 779–793.
- MUNK, M. 1924 Elements of the wing section theory and of the wing theory. rept no 191. *Tech. Rep.*. NACA.
- OKULOV, V. L. 2004 On the stability of multiple helical vortices. *J. Fluid Mech.* **521**, 319–342.
- OKULOV, V. L. & SORENSEN, J. N. 2007 Stability of helical tip vortices in a rotor far wake. *J. Fluid Mech.* **576**, 1–25.
- OKULOV, V. N. 2016 An acentric rotation of two helical vortices of the same circulations. *Regular and Chaotic Dyn.* **21**, 267–273.
- PAIDOUSSIS, M. P. 2004 *Fluid-Structure Interactions: Slender Structures And Axial Flow, Volume 2*. Academic Press.
- PAYNE, P. R. 1959 *Helicopter Dynamics and Aerodynamics*. Pitman & Sons, London.
- PHILLIPS, W. F. & SNYDER, D. O. 2000 Modern adaptation of Prandtl’s classic lifting-line theory. *Journal of Aircraft* **37(4)**, 662–670.
- PRANDTL, L. 1921 Applications of modern hydrodynamics to aeronautics. *Tech. Rep.*. NACA 116.
- PRANDTL, L. & BETZ, A. 1927 Vier abhandlungen zur hydrodynamik und aerodynamik. *Gottingen Nachr.* pp. 88–92.
- PROUTY, R. W. 1986 *Helicopter Performance, Stability and Control*. Prindle, Weber & Schmidt, PWS Engineering, Boston.
- QUARANTA, H. U., BOLNOT, H. & LEWEKE, T. 2015 Long-wave instability of a helical vortex. *J. Fluid Mech.* **780**, 687–716.

- QUARANTA, H. U., BRYNJELL-RAHKOLA, M., LEWEKE, T. & D.S., H. 2018 Local and global pairing instabilities of two interlaced helical vortices. *J. Fluid Mech.* **863**, 927 – 955.
- QUARANTA, U. 2017 Instabilities in a swirling rotor wake. PhD thesis, Aix Marseille Université.
- RANKINE, W. J. M. 1865 On the mechanical principles of the action of propellers. *Trans. Inst. Naval Arch.* **6**, 13–39.
- REISSNER, H. 1937 On the vortex theory of the screw propeller. *J. Aeronaut. Sciences* **5** (1), 1–6.
- REISSNER, H. 1940 A generalized vortex theory of the screw propeller and its application. TN 750. *Tech. Rep.*. NACA.
- RICCA, R. L. 1994 The effect of torsion on the motion of a helical vortex filament. *J. Fluid Mech.* **273**, 241–259.
- SAFFMAN, P. G. 1992 *Vortex dynamics*. Cambridge University Press.
- SARMAST, R., DADFAR, R., MIKKELSEN, R. F., SCHLATTER, P., IVANELL, S., SORENSEN, J. & HENNINGSON, D. 2014 Mutual inductance instability of the tip vortices behind a wind turbine. *J. Fluid Mech.* **755**, 705–731.
- SCHEPERS, J. G., BOORSMA, K., CHO, T., GOMEZ-IRADI, S., SCHAFFARCZYK, P., JEROMIN, A. & SØRENSEN, N. N. 2012 Analysis of mexico wind tunnel measurements: Final report of IEA task 29, Mexnext (phase 1). *Tech. Rep.*. Research Centre of the Netherlands (ECN).
- SCHEPERS, J. G. & SNEL, H. 2007 Mexico, model experiments in controlled conditions. ECN-E-07-042. *Tech. Rep.*. Research Centre of the Netherlands (ECN).
- SELÇUK, C., DELBENDE, I. & ROSSI, M. 2017 Helical vortices: Quasi-equilibrium states and their time evolution. *Phys. Rev. Fluids* **2**, 084701.
- SELÇUK, C., DELBENDE, I. & ROSSI, M. 2018 Helical vortices: linear stability analysis and nonlinear dynamics. *Fluid Dyn. Res.* **50**, 011411.
- SHELLEY, M. J. & ZHANG, J. 2011 Flapping and bending bodies interacting with fluid flows. *Annu. Rev. Fluid Mech.* **43**, 449–465.
- SHEN, W. Z., MIKKELSEN, R., SØRENSEN, J. N. & BAK, C. 2005 Tip loss corrections for wind turbine computations. *Wind Energy* **8** (4), 457–475.
- SICARD, U. 2014 Development of an extremely flexible, variable-diameter rotor for a micro-helicopter. PhD thesis, The University of Texas at Austin.
- SICKLINGER, S., KÜRKCHÜBASCHKE, A., BELSKY, V., WÜCHNER, R. & BLETZINGER, K.-U. 2015 Fluid-structure interaction with controls for wind turbine simulation using a novel co-simulation approach. *Journal of Wind Engineering and Industrial Aerodynamics* **144**, 135–145.

- SNEL, H., SCHEPERS, J. & MONTGOMERIE, B. 2007 The mexico project (model experiments in controlled conditions): The database and first results of data processing and interpretation. *Journal of Physics: Conference Series* **75**.
- SORENSEN, J. & SHEN, W. 2002 Numerical modeling of wind turbine wakes. *J. Fluids Eng.* **124**, 393–399.
- SØRENSEN, J. N. 2016 *General momentum theory for horizontal axis wind turbines*, Springer series: Research topics in wind energy, vol. 4. Springer.
- STACK, J., CARADONNA, F. & SAVAS, O. 2005 Flow visualizations and extended thrust time histories of rotor vortex wakes in descent. *J. Am. Helicopter Soc* **50**, 279–288.
- THEODORSEN, T. 1948 *Theory of Propellers*. McGraw-Hill.
- THOMSON, J. 1883 *A treatise on the Motion of Vortex Rings*. Mac-Millan, London.
- TIMOSHENKO, S. P. 1922 On the transverse vibration of bars of uniform cross-section. *Philosophical Magazine* p. 125.
- VELASCO FUENTES, O. 2018 Motion of a helical vortex. *J. Fluid Mech.* **836**, R1.
- VERMEER, L. J., SØRENSEN, J. N. & CRESPO, A. 2003 Wind turbine wake aerodynamics. *Prog. Aero. Scie.* **39**, 467–510.
- VOLOVOI, V. V., HODGES, D. H., CESNIK, C. E. & POPSCU, B. 2001 Assessment of beam modeling methods for rotor blade applications. *Mathematical and computer modelling* **33(10–11)**, 1099–1112.
- WALTHER, J. H., GUÉNOT, M., MACHEFAUX, E., RASMUSSEN, J. T., CHATELAIN, P., OKULOV, V. L., SØRENSEN, J. N., BERGDORF, M. & KOUMOUTSAKOS, P. 2007 A numerical study of the stability of helical vortices using vortex methods. *J. Phys.: Conf. Ser.* **75**, 012034.
- WASHIZU, K., AZUMA, A., KOO, J. & OKA, T. 1966 Experiments on a model helicopter rotor operating in the vortex ring state. *Journal of Aircraft* **3(3)**, 225–230.
- WIDNALL, S. E. 1972 The stability of a helical vortex filament. *J. Fluid Mech.* **54**, 641–663.